Optical properties of InP/AlGaInP quantum dot laser heterostrucutures

Julie Lutti

PhD thesis

2005

Cardiff University – School of Physics and Astronomy

ProQuest LLC
789 East Eisenhower Parkway
P.O. Box 1346
Ann Arbor, MI 48106-1346

Abstract

Optical characterisation of InP/AlGaInP quantum dot laser structures, involving laser threshold and wavelength, optical modal gain and absorption spectra, and radiative efficiency are presented. The samples were grown by MOVPE in Sheffield University on (100) 10°off and (211)B GaAs substrates, and consist of 5 layers of self-assembled InP dots, with each layer grown on $Al_{0.3}Ga_{0.7}InP$ and placed in a GaInP quantum well. A record low threshold current density of 290A/cm^2 at a wavelength of 740nm for a 1.6 mm-long device with uncoated facets is obtained from one of the sample grown on (100) 10°off substrate at 690°C. This sample has an internal optical mode loss of 4 ± 1 cm^{-1} and an internal quantum spontaneous emission efficiency of 30% for current densities corresponding to the threshold. The ground state modal gain is shown to saturate at 17cm^{-1} at room temperature, which is about ¼ of the full population inversion limit, and the saturation level increases with decreasing temperature. A sample grown at a lower temperature of 650°C has higher optical mode loss (7.5 ± 1 cm^{-1}) and quantum efficiency under 15%. A sample grown on (211)B substrate exhibits optical transitions at higher photon energies, consistent with smaller dot sizes.

The thesis also presents an analysis of the segmented contact technique used to measure gain and absorption spectra, determining criteria for the excitation and detection geometries required to ensure accurate measurement. It is shown that the collection angle and device nearfield should be limited so that rays that intercept the stripe edges are not collected. If this is not satisfied, the measurement underestimates the modal gain. An exponential variation of the measured ASE upon stripe length cannot be taken as evidence for a correct collection geometry.

Acknowledgments

I would like to express my gratitude to both my supervisors, Peter Smowton and Peter Blood, for their guidance and support during my PhD. To Peter Blood I am thankful for his willingness to share his knowledge, his many helpful comments and advice, and his encouragements. I am grateful to Peter Smowton for his insightful and constructive suggestions and his enthusiasm.

I would also like to thank Andrey Krysa for his willingness to answer at length to my questions about growth, and Gareth Lewis for contributing his knowledge and skills to this work.

Table of contents

Glossary

The various symbols used throughout the thesis are listed below with the physical quantities that they represent.

Variables:

α : modal absorption

A : vector potential

A_0 : vector potential amplitude

$\alpha+\alpha_i$: net modal absorption

α_i : intrinsic modal loss

β : fraction of spontaneous emission coupled to the waveguide

C : coupling coefficient

ΔE_F : quasi Fermi-level energy separation

E_{Fc}, E_{Fv} : quasi-Fermi levels for the conduction / valence bands

E_Γ : direct bandgap

$\hat{e}$: unit polarisation vector

ϕ : angle of propagation perpendicularly to the plane of the waveguide

Φ : internal collection half-angle perpendicularly to the waveguide plane

Φ' : external collection half-angle perpendicularly to the waveguide plane

ϕ : photon flux

F_c, F_v : envelope function for a state in the conduction / valence band

f_c, f_v : occupation probability of an electron state in the conduction / valence band

G : modal gain: $G = -\alpha$

$G-\alpha_i$: net modal gain

HH : heavy hole

$\hbar\omega$: photon energy

$I(\hbar\omega)$: Amplified Spontaneous Emission spectrum

J : current density

k : electron wavevector

$\kappa(\hat{e})$: relative transition strength for transitions between a conduction and valence state for different light polarisation $\hat{e}$.

k_0 : photon wavevector in vacuum

$L\ (E)$: homogeneous linewidth

L_c : laser cavity length

L_{eff} : effective mode width

LH : light hole

m^* : effective mass

M : momentum matrix element

M_T : transition matrix element

m_0 : free electron mass

m_e : effective mass for the conduction band

$m_{hh,lh}$: effective masses in the heavy hole / light hole bands

N : dot density

n : refractive index

n_{eff} : effective index (phase index)

n_g : group index

P_f : inversion factor

θ : angle of propagation with the axis of the waveguide, in the plane of the waveguide

Θ : internal collection half-angle in the plane of the waveguide

Θ' : external collection half-angle in the plane of the waveguide

ρ : density of states

R : facet reflectivity

ρ_{red} : reduced density of states

R_{sp} : spontaneous emission rate spectrum, per unit area of the active region.

SO : spin-orbit split-off hole

w : stripe width

$W_{c\rightarrow v}$, $W_{v\rightarrow c}$: induced radiative transition from the conduction to the valence band, and inversely

ψ : electron wavefunction

Constants:

Speed of light in vacuum:
$c = 299\ 792\ 458$ m s^{-1}

Reduced Planck constant:
$\hbar = 6.582\ 119\ 15 \times 10^{-16}$ eV.s

Boltzmann constant
$k = 8.617\ 343 \times 10^{-5}$ eV.K^{-1}

Dielectric constant:
$\varepsilon_0 = 8.854\ 187\ 817 \times 10^{-12}$ F.m^{-1}

Elementary charge:
$e = 1.602\ 176\ 53 \times 10^{-19}$ C

Electron mass:
$m_0 = 9.109\ 3826 \times 10^{-31}$ kg

I. Introduction

I.1. Presentation

This PhD project has been carried out in the Optoelectronics Research Group in Cardiff University as part of a collaborative project with Sheffield University focusing on the development of InP/AlGaInP quantum dot laser structures.

Interest for laser applications in these structures is motivated by the general potential benefits of quantum dot lasers over quantum well lasers, which have been demonstrated in InAs/InGaAs system, and by the possibility of extending the upper wavelength limit of conventional GaInP quantum well lasers from 690 nm to the region of 750 nm. Compared to InAs/InGaAs quantum dot lasers, InP/AlGaInP quantum dot laser devices have received less attention and have so far not reached the same good performances.

The general aim of this PhD project has been to investigate the performances of InP/AlGaInP quantum dot laser diodes grown by Sheffield University. Optical characterisation of the samples includes measurement of laser threshold and wavelength, modal gain and absorption spectra, and radiative efficiency. The main characterisation technique is the multisection or segmented contact technique, which has been developed in the Optoelectronics Research Group in Cardiff University since 1999. The experimental techniques and procedures are outlined in chapter II. Further developments of the technique made in the course of this work are detailed in chapter III. Chapter IV describes the InP/AlGaInP quantum dot laser heterostructures that were grown for the project and gives threshold current data of lasers fabricated from some of the structures. Chapter V presents the results of passive modal optical absorption spectra, comparing properties of different samples at room temperature. Chapter VI focuses on measurements of gain spectra under electrical injection, radiative efficiency and describes the phenomenon of gain saturation. The thesis ends with a summary of the outcomes of the work.

This introductory chapter gives the basic principle of laser diodes (I.2), a brief description of electronic states in III-V semiconductors and the relevant properties of the AlGaInP material system (I.3), an outline of quantum dot growth and quantum dot lasers (I.4), and a description of gain and emission process in a semiconductor medium (I.5).

I.2. Laser devices

I.2.1 Edge-emitting laser diode

The optically active medium of semiconductor laser diodes is typically provided by a direct bandgap semiconductor, the active optical transition being between the electronic conduction and valence energy bands. The emission wavelength or photon energy of the laser is primarily a function of the semiconductor bandgap.

If the active medium is pumped so that there are more electrons in the upper than lower states involved in transitions at some energy, light at that photon energy is amplified by the medium by the process of stimulated emission. In a laser the active medium is placed within a resonant cavity of length L_c, and light is amplified when travelling back and forth along the cavity. Lasing action is obtained when the amplification of light along the cavity compensates for the optical cavity losses.

A typical design of semiconductor diode laser device is represented in Figure I-1. It is an edge-emitting device processed with oxide-isolated stripe contact like lasers fabricated for this work. The active medium is placed between a p-doped and an n-doped region, which enables pumping of the active medium by electrical current. When a forward voltage is applied to the diode, the electrons in the conduction band of the n-doped material flow to the active region (generally undoped) where they decay radiatively to the valence band, and flow out of the device through the p-doped material. Light is amplified along x and optical feedback is provided by partial reflection at the cleaved facets at both ends, with the cavity length indicated by L_c on the figure. The stripe contact on the top surface of the device allows for the current flow to be confined to a small region of the device.

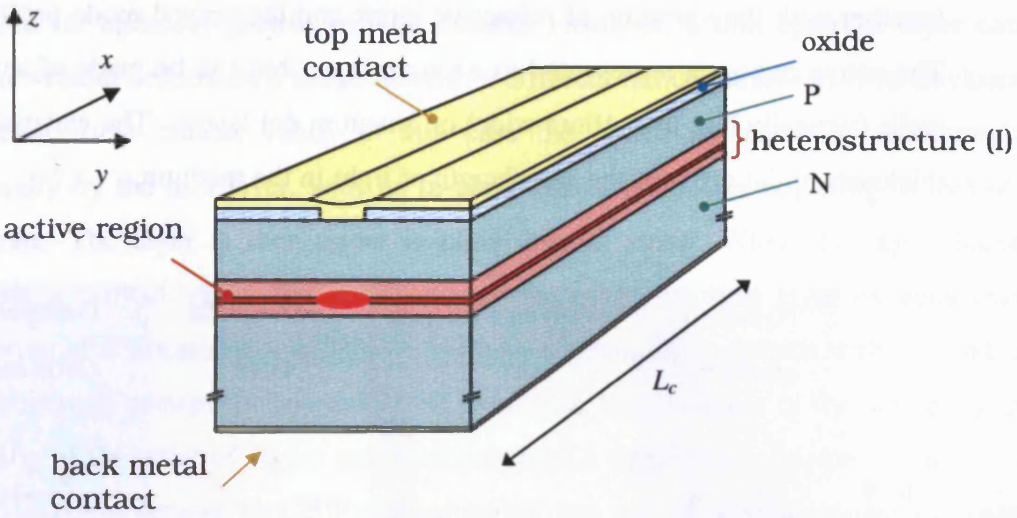

Figure I-1 Edge emitting laser chip with oxide stripe geometry – not to scale

Light amplification is quantified by the modal optical gain which is defined as the fractional increase of light intensity in a given optical mode per unit distance travelled. Laser action occurs when the modal gain G provided by the active region compensates the internal optical losses α_i, and the losses due to transmission at the device facets.

At laser threshold, the gain satisfies the round-trip amplification condition, given by:

$$G - \alpha_i = \frac{1}{L_c}\ln\left(R^{-1}\right) \tag{I.1}$$

where L_c is the cavity length, indicated on Figure I-1, and R is the intensity reflection coefficient, which is assumed to be the same at both facets.

I.2.2 Separate confinement heterostructure

The first semiconductor lasers consisted of heavily doped p-n homostructures (i.e. made of the same semiconductor), which were very inefficient and required a lot of current to reach threshold because the carrier recombination region was not well defined. With the development of heterostructures, i.e. the technology to grow epitaxial layers with different material composition, threshold currents were reduced by embedding the active region in a semiconductor with higher bandgap and lower refractive index, which confines both carriers and light to the active region.

In a separate confinement heterostructure, carriers and light are confined separately.

Figure I-2 represents the energy band diagram of such a structure under forward bias, together with the variation of refractive index and the optical mode profile underneath. The active region is represented as a single layer, but can be made of several quantum wells (typically less than 10nm wide) or quantum dot layers. The waveguide core has a thickness of the order of the wavelength of light in the medium.

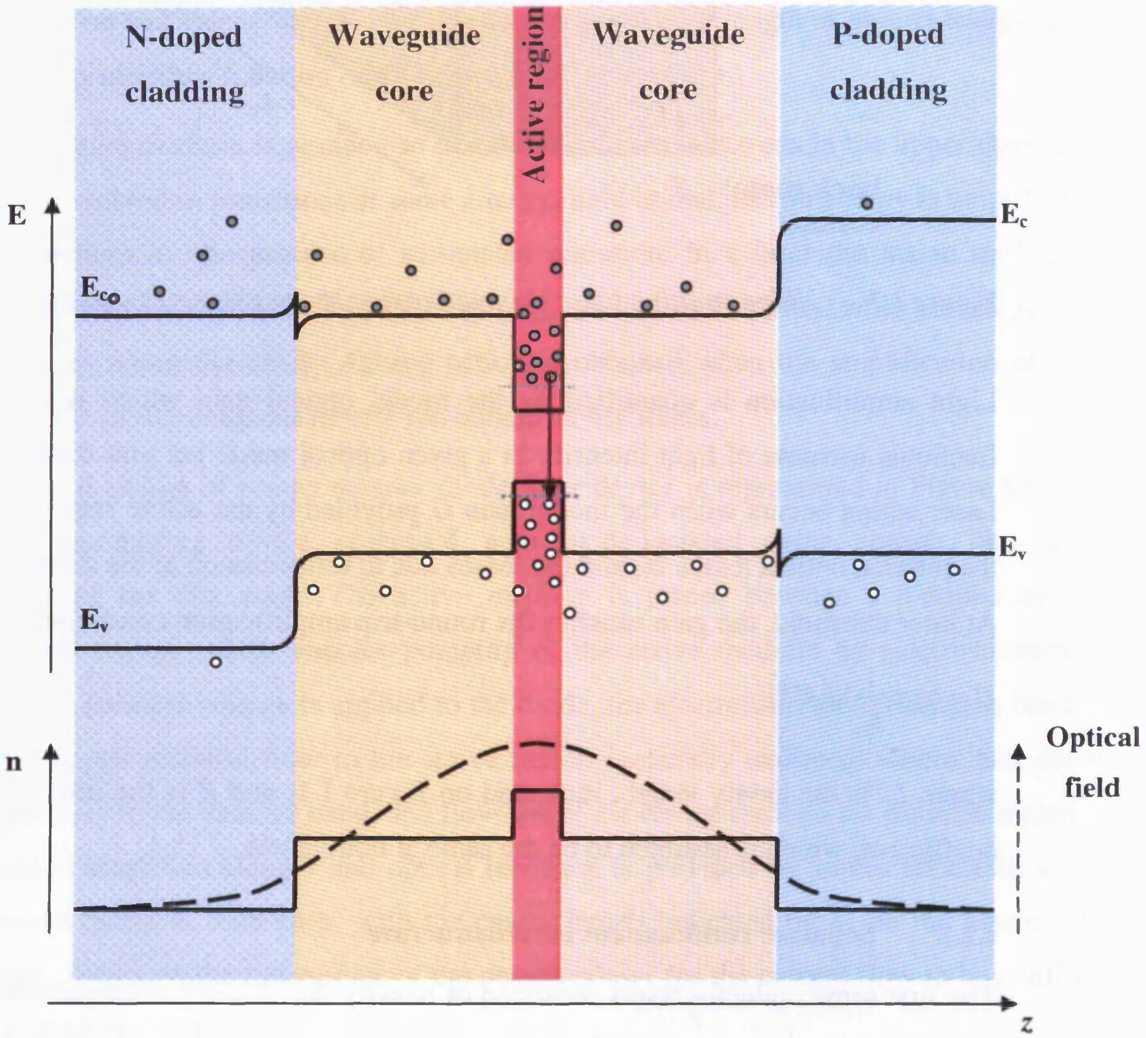

Figure I-2 Band edge diagram of a forward biased double heterostructure and refractive index profile - not to scale

In semiconductor heterostructures, lattice matching between the different bulk layers is required for epitaxial growth without defects. However, a thin epitaxial layer can be grown without defects on a substrate with a different lattice parameter if its thickness is less than some critical value. In this case the lattice mismatch is accommodated elastically by the thin layer, with its in-plane lattice parameter adjusting to that of the substrate. The layer is then under in-plane biaxial strain. When the layer thickness exceeds a critical value, the strain energy stored in the thin layer exceeds that of formation of dislocations and dislocations appear, resulting in defects with non-radiative recombination centres. In quantum well structures, the thickness of the active region is typically of the order of 10 nm and materials with a small lattice mismatch can be used, which gives a greater flexibility by allowing the use of a wider range of material compositions. For a GaInP quantum well, the critical thickness is about 20 nm for a lattice mismatch of 1% with the substrate ([I.1]).

I.3. Electronic states in III-V semiconductors

I.3.1 Generalities

This section briefly describes the valence and conduction band states of a direct bandgap III-V semiconductor, in bulk material and in quantum confined structures. It also describes how strain affects the band structure.

I.3.1.1) Conduction and valence bands

In a bulk crystal the electrons are subject to a periodic potential created by the lattice. From Bloch's theorem, the eigenstates have the form:

$$\psi_k(r) = u_k(r)e^{-jk.r} \tag{I.2}$$

where k is the particle wavevector and $u_k(r)$ is a Bloch function, which has the potential periodicity. The energy of the eigenstates can be represented in an *E(k)* diagram which gives the band structure of the crystal. The conduction and valence bands near the band edge are illustrated in Figure I-3. The three valence bands are the heavy hole (HH), light hole (LH) and spin-orbit split-off hole (SO) bands.

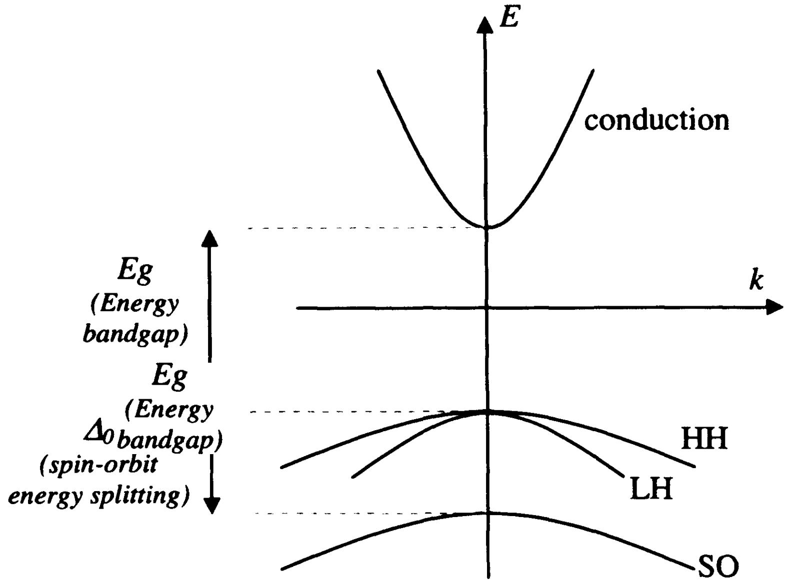

Figure I-3 Valence and conduction band structure in a III-V semiconductor

For small values of k, i.e. near the band edge, the bands are often assumed to be parabolic, and the effective mass of the band, defined as (I.3), determines its curvature.

$$m^* = \frac{\hbar^2}{\partial^2 E / \partial k^2} \tag{I.3}$$

The Bloch functions are not a strong function of k and are approximated by the band edge ($k = 0$) functions. The conduction band Bloch function is denoted by $u_c(r)$, and $u_v(r)$ denotes the valence Bloch functions.

In order to determine how the valence and conduction bands align in a heterojunction, it is necessary to know the position of the bands in the different materials making up the junction on an absolute energy scale. The position of the bands for common III-V binaries was calculated by Van der Walle using model solid theory ([I.21]).

The energy position of the conduction, heavy hole, light hole and split-off hole band edges are denoted respectively by E_C, E_{HH}, E_{LH} and E_{SO}.

If $E_{v,av}$ denotes the average valence-band energy $E_{v,av} = \frac{1}{3}(E_{HH} + E_{LH} + E_{SO})$, the position of each band is characterised by the knowledge of $E_{v,av}$, the bandgap E_g and spin-orbit splitting Δ_0:

$$\begin{cases} E_c = E_{v,av} + \frac{\Delta_0}{3} + E_g & \text{(I.4)} \\ E_{vHH} = E_{vLH} = E_v = E_{v,av} + \frac{\Delta_0}{3} & \text{(I.5)} \\ E_{vSO} = E_{v,av} - 2\frac{\Delta_0}{3} & \text{(I.6)} \end{cases}$$

These expressions are modified in the presence of strain, whose effect is described in section I.3.1.5).

I.3.1.2) Envelope function approximation

If a local potential confines the carriers spatially in the crystal, like in quantum well or quantum dot structures, the periodicity is broken.

In the envelope function approximation, the states are expanded on the Bloch functions of different bands, assumed to be identical in each material:

$$\psi(r) = \sum_l f_l(r) u_l(r) \tag{I.7}$$

where $u_l(r)$ is the band edge Bloch function of band l and $f_l(r)$ is an envelope function. This is generally a good approximation if the Bloch functions are similar in the different materials or if the considered states are strongly confined in one material.

With the additional assumption that there is no band mixing, the states can be written as:

$$\psi(r) = u(r) F(r) \tag{I.8}$$

where $u(r)$ is the Bloch function of the considered band, which takes into account the periodic atomic scale potential, and $F(r)$ is the normalised slowly varying envelope function. $F(r)$ is obtained by solving Schrödinger's equation using the macroscopic potential that follows the band edge in the structure, and the appropriate effective mass (I.3).

The form of the normalised envelope function for bulk, quantum well and quantum dot material is given below:

Bulk

$F(r)=\frac{e^{-jk.r}}{\sqrt{V}}$, where V is the bulk crystal volume. This is equivalent to Bloch's theorem (I.2).

Quantum well

$F(r)=F(z)\frac{e^{-jk.r_{//}}}{\sqrt{A}}$, where A is the area of the quantum well, assumed to be in the (*xy*) plane, and $F(z)$ is the solution of the Schrödinger's equation for a one-dimensional well, defined by the conduction or valence band profile in the *z*-direction. For each solution $F(z)$, the ensemble of the wavefunctions with different in-plane *k*-vectors forms a subband of the quantum well. The band edge energy of each subband can be calculated as described in the next section.

Quantum dot

$F(r)$ is the normalised solution of Schrödinger's equation for the three-dimensional potential defined by the conduction or valence band profile.

I.3.1.3) Energy states in quantum well

The subband edge energies of a square symmetric quantum well in the (*xy*) plane are found by solving Schrödinger's eigenvalue equation for a one-dimensional potential well along *z* with the appropriate effective masses along *z* in the well and barrier region, denoted respectively by m_w and m_b. The quantum well is schematised in Figure I-4. V_0 denotes the potential energy height of the quantum well.

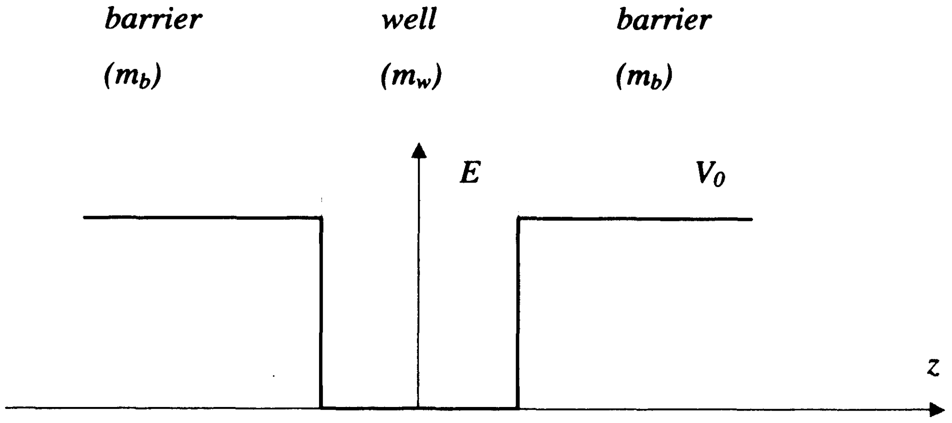

Figure I-4 Diagram of a one-dimensional potential well

From references [I.19] and [I.20], the energy levels E_n of the quantum well at each subband (n) edge are found by finding the solutions n_{QW} of the following equations:

$$\tan\left(\frac{\pi}{2}n_{QW}\right)=\sqrt{\frac{m_w}{m_b}}\frac{1}{n_{QW}}\sqrt{n_{\max}^2-n_{QW}^2} \qquad \text{(I.9)}$$

$$\tan\left[\frac{\pi}{2}(n_{QW}-1)\right]=\sqrt{\frac{m_w}{m_b}}\frac{1}{n_{QW}}\sqrt{n_{\max}^2-n_{QW}^2} \qquad \text{(I.10)}$$

$$\text{with } n_{\max}=\sqrt{\frac{V_0}{E_1^\infty}} \text{ and } n_{QW}=\sqrt{\frac{E_n}{E_1^\infty}} \qquad \text{(I.11)}$$

Equations (I.9) and (I.10) give the confinement energies E_n (I.11) for respectively the even and odd confined eigenstates.

Calculations of the subband edge energies of a square symmetric quantum well are used to interpret experimental data in chapter IV.

I.3.1.4) Density of states

The following expressions include spin degeneracy.

Bulk

In bulk material, the number of states per unit volume and per unit energy interval in one band with associated effective mass m^* is:

$$\rho_{3D}(E)=\frac{1}{2\pi^2}\left(\frac{2m^*}{\hbar^2}\right)^{3/2}\sqrt{E} \qquad [E]^{-1}.[L]^{-3} \qquad \text{(I.12)}$$

Quantum well

In each subband of a quantum well, the number of states per unit energy interval and unit area is:

$$\rho_{2D}(E)=\frac{m^*}{\pi\hbar^2} \text{ for } E>E_0 \qquad [E]^{-1}.[L]^{-2} \qquad \text{(I.13)}$$

where E_0 is the band edge energy associated with the considered subband and m^* is the effective mass in the plane of the quantum well.

Quantum dot

Although the states of a quantum dot are not spread over a continuum of energy, it is always possible to define a density of states per unit energy interval by using delta functions. For one quantum dot, the number of states per unit energy interval associated with, say, the ground state of the conduction band, is:

$\rho_{0D}(E) = 2.\delta(E - E_0)$ $[E]^{-1}$ (I.14)

where E_0 is the conduction ground state energy.

For an ensemble of identical quantum dots distributed in a plane with density N per unit area, the number of dot states per unit area and unit energy interval is:

$\rho_{0D}(E) = 2.N.\delta(E - E_0)$ $[E]^{-1}.[L]^{-2}$ (I.15)

I.3.1.5) Effect of biaxial strain on band structure

I.3.1.5.1 Biaxial strain

The strain is defined as the variation of the lattice constant of a material relative to its native value, in a particular crystal direction.

It was mentioned before that when a thin layer of material with native lattice constant a is grown on a substrate with a different lattice constant a_0, the thin layer adopts the lattice parameter of the substrate in the growth plane, so that the layer is subject to biaxial strain parallel to the plane of the layer ($\varepsilon_{//}$) and uniaxial strain perpendicularly to it ($\varepsilon_{\perp}$). Then the in-plane strain is given by::

$$\varepsilon_{//} = \frac{a_{//}}{a} - 1 = \frac{a_0}{a} - 1 \quad \text{(I.16)}$$

and in the case of growth in the (100) direction:

$$\varepsilon_{\perp} = \frac{a_{\perp}}{a} - 1 = -2.\frac{C_{12}}{C_{11}}.\varepsilon_{//} \quad \text{(I.17)}$$

where C_{11} and C_{12} are elastic constants of the material.

I.3.1.5.2 Effect of biaxial strain on band edge energies

Strain changes the position of the band edge energies E_C, E_{HH}, E_{LH} and E_{SO}. The expressions given here are for the case of in-plane biaxial strain and are taken from the summary of model solid theory by Krijn ([I.22]). The positions of the four band edges under biaxial strain in the (100) plane are given by:

$$\left\{\begin{array}{ll}
E_C = E_{C0} + \Delta E_C^{hy} & \text{(I.18)} \\
E_{HH} = E_{v,av_0} + \Delta E_{v,av}^{hy} + \dfrac{\Delta_0}{3} - \dfrac{\delta E^{sh}}{2} & \text{(I.19)} \\
E_{LH} = E_{v,av_0} + \dfrac{\Delta_0}{3} + \Delta E_{v,av}^{hy} + \dfrac{1}{2}\left(-\Delta_0 + \dfrac{\delta E^{sh}}{2}\right) + \dfrac{1}{2}\sqrt{\Delta_0{}^2 + 2\Delta_0\left(\dfrac{\delta E^{sh}}{2}\right) + 9\left(\dfrac{\delta E^{sh}}{2}\right)^2} & \text{(I.20)} \\
E_{SO} = E_{v,av_0} - \dfrac{2\Delta_0}{3} + \Delta E_{v,av}^{hy} + \dfrac{1}{2}\left(\Delta_0 + \dfrac{\delta E^{sh}}{2}\right) - \dfrac{1}{2}\sqrt{\Delta_0{}^2 + 2\Delta_0\left(\dfrac{\delta E^{sh}}{2}\right) + 9\left(\dfrac{\delta E^{sh}}{2}\right)^2} & \text{(I.21)}
\end{array}\right.$$

where E_{C0}, E_{v,av_0} and Δ_0 are respectively the conduction band edge, the average valence band edge, and spin-orbit split-off energies in the absence of strain, and where

$$\left\{\begin{array}{ll}
\Delta E_C^{hy} = a_c\left(2\varepsilon_{//} + \varepsilon_{\perp}\right) & \text{(I.22)} \\
\Delta E_{v,av}^{hy} = a_v\left(2\varepsilon_{//} + \varepsilon_{\perp}\right) & \text{(I.23)} \\
\dfrac{\delta E^{sh}}{2} = b\left(\varepsilon_{\perp} - \varepsilon_{//}\right) & \text{(I.24)}
\end{array}\right.$$

The material parameters a_c and a_c are the hydrostatic deformation potentials for the conduction and valence bands respectively, and b is the tetragonal shear deformation potential.

I.3.1.5.3 Effect of biaxial strain on effective masses

Biaxial strain affects the effective masses of the valence bands.

The perpendicular effective masses (normal to the plane of the biaxial strain) are not affected. In the limit of high strain, the parallel (in-plane) masses are given by (Appendix 8 of [I.19]):

$$m_{HH,//} = \frac{1}{4}.\left(3m_{LH} + m_{HH}\right) \tag{I.25}$$

$$m_{LH,//} = \frac{1}{4}.\left(3m_{HH} + m_{LH}\right) \tag{I.26}$$

I.3.2 InP/GaInP/AlInP material system for laser heterostructures

I.3.2.1) Introduction

The structures fabricated and measured for this PhD project are based on a separate confinement heterostructure (SCH) in the AlGaInP system, grown on a GaAs substrate.

The quaternary alloy $(Al_xGa_{1-x})_yIn_{1-y}P$ is lattice matched to GaAs for $y = 0.516$. Its bandgap increases with increasing Aluminium composition x, while its refractive index decreases. In typical SCH structures in this material system, the active region consists of one or several $Ga_yIn_{1-y}P$ quantum wells, and increasing aluminium composition is used for the waveguide core (or barrier) and the cladding.

In the structures studied in this PhD work, the active region consists of InP quantum dots deposited in GaInP wells lattice-matched to GaAs. The core and the cladding are made of $(Al_xGa_{1-x})_{0.51}In_{0.49}P$ with aluminium content of respectively $x = 0.3$ and $x = 1$.
In this section, the material properties that are referred to later in the thesis are described.
Properties of the AlGaInP material system are reviewed in references [I.1] and [I.2]. For an extensive review of band parameters in III-V compounds, one can refer to [I.3].

I.3.2.2) Lattice parameter

The lattice parameter of the InP binary compound at room temperature (300K) is:

$$a = 5.869 \quad (\overset{\circ}{A}) \tag{I.27}$$

By linear interpolation of the lattice constant of the binaries InP (5.869 Å) and GaP (5.451 Å), the lattice constant of $Ga_yIn_{1-y}P$ is:

$$a = 5.869 - 0.418.y \quad (\overset{\circ}{A}) \tag{I.28}$$

$Ga_yIn_{1-y}P$ is lattice matched to the GaAs substrate ($a = 5.653\overset{\circ}{A}$) for $y = 0.516$, and so is $(Al_xGa_{1-x})_{0.516}In_{0.484}P$ is lattice-matched to GaAs for any value of x.
In the rest of the thesis, GaInP and (Al_xGa_{1-x})InP written without the "y" subscript designate the lattice-matched compositions.

I.3.2.3) Ordering

The ternary alloy GaInP can grow in a disordered phase, where the Gallium and Indium atoms occupy the group III sublattice randomly, or in a ordered phase, where the group III sub lattice consists of alternating (111) planes of one atomic species. Atomic ordering of the group III planes reduces the bandgap energy, such that random and ordered GaInP have respective bandgap energies of 1.91 eV and 1.84 eV at room temperature. The degree of ordering depends on the growth conditions as well as the substrate orientation ([I.6]). GaInP grown on (100) GaAs surface tends to exhibit strong ordering, which is reduced when the growth surface is inclined towards (111) or (110). Heterostructures grown for the project were grown on such substrates, the growth plane being either (100) oriented 10° towards (111), or (211)B, in order to ensure the growth of fully disordered alloy.

Growth temperature is a critical parameter for growth of good quality quaternary AlGaInP alloys, with a temperature around 700°C being optimum for MOVPE growth.

I.3.2.4) Bandgaps

InP:

From ([I.3], [I.4]), the temperature dependence of the direct bandgap of InP follows:

$$E_\Gamma(T) = E_\Gamma(0) - \frac{\alpha T^2}{T+\beta} \qquad (I.29)$$

with $E_\Gamma(0) = 1.4236$ eV, $\alpha = 0.363$ meV/K and $\beta = 162$ K.

It gives at 295K:

$$E_\Gamma = 1.354 \quad (eV) \qquad (I.30)$$

GaInP lattice-matched to GaAs

Reference ([I.7]) reports measurement of the direct bandgap of fully disordered lattice-matched GaInP at 295 K at a value of:

$$E_\Gamma = 1.91\,(eV) \qquad (I.31)$$

And the temperature dependence of the bandgap determined in ([I.1]) is:

$$E_\Gamma(T) = E_\Gamma(0) - S.\langle\hbar\omega\rangle\left[\coth\left(\frac{\langle\hbar\omega\rangle}{2kT}\right) - 1\right] \qquad (I.32)$$

with $E_\Gamma(0) = 1.992$ eV , S = 2.478 and $\langle\hbar\omega\rangle = 0.0220$ eV.

$Ga_yIn_{1-y}P$

By interpolation of the direct bandgap energies of the binaries GaP (2.74 eV) and InP (1.35 eV), and that of GaInP lattice matched GaAs (1.91 eV), the direct bandgap of bandgap of $Ga_yIn_{1-y}P$ is:

$$E_\Gamma = 1.35 + 0.76.y + 0.63.y^2 \quad (eV) \tag{I.33}$$

$Al_xGa_{1-x}InP$ lattice-matched to GaAs

The direct bandgap of lattice-matched $Al_xGa_{1-x}InP$ quaternary at 295K is given in ([I.5]) as:

$$E_\Gamma = 1.91 + 0.61.x \; (eV) \tag{I.34}$$

For an aluminium fraction x of 0.3, reference ([I.1]) reports the following temperature dependence of the bandgap:

$$E_\Gamma(T) = E_\Gamma(0) - S.\langle\hbar\omega\rangle\left[\coth\left(\frac{\langle\hbar\omega\rangle}{2kT}\right) - 1\right] \tag{I.35}$$

with $E_\Gamma(0) = 2.175$ eV , S = 2.471 and $\langle\hbar\omega\rangle = 0.0242$ eV.

I.3.2.5) Heterojunction band lineups

In this work the position of the bands on an absolute scale are obtained from reference ([I.1]) for the AlInP/GaInP material system, which follows the interpolation scheme described by Krijn ([I.22]).

Table I-1 regroups the value of the average valence band energy $E_{v,av}$ (average of heavy, light, and split-off holes) and the spin-orbit splitting Δ_0 for the alloys of interest (unstrained). In the table, a is the symbol for the lattice parameter (I.28). The position of each band for unstrained material can then be obtained from equations (I.4) to (I.6).

	$Ga_yIn_{1-y}P$	$(Al_xGa_{1-x})_{0.516}In_{0.484}P$
average valence band energy $E_{v,av}$ (eV)	$(-41.32 + 1.4y - 0.4y^2)/a$ with a lattice parameter in Å	$-7.2 - 0.25x$
Spin-orbit splitting Δ_0 (eV)	$0.11 - 0.03y$	$0.108 + 0.0284x$

Table I-1 Average valence band energy and spin-orbit splitting for unstrained alloys

The additional material parameters needed to describe the variation of band positions with biaxial strain in $Ga_yIn_{1-y}P$ are given in Table I-2.

	symbol	value
hydrostatic deformation potential for conduction band (in eV)	a_c	$-5.04 + 2.1\,y$
hydrostatic deformation potential for valence band (in eV)	a_v	$1.27 + 0.43\,y$
tetragonal shear deformation potential (in eV)	b	$-1.6 + 0.1\,y$
elastic constant C_{11} (in 10^{12} dyn.cm^{-2})	C_{11}	$1.02 + 0.39\,y$
elastic constant C_{12}(in 10^{12} dyn.cm^{-2})	C_{12}	$0.58 + 0.04\,y$

Table I-2 Strain-related material parameters for $Ga_yIn_{1-y}P$

The band positions for the alloys of interest have been calculated and plotted in Figure I-5.

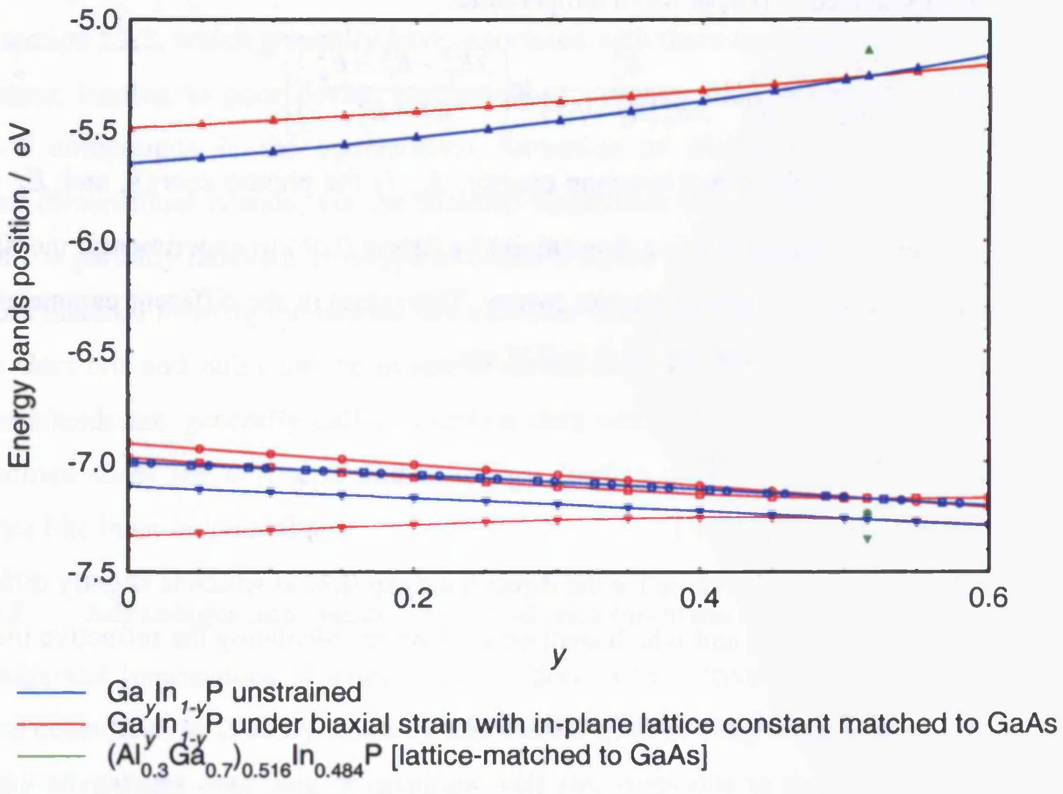

Figure I-5 Band edge energy positions for the conduction (▲), HH (●), LH (■) and SO (▼) bands.

I.3.2.6) Effective masses

Following reference ([I.1]) which summarises values of effective masses obtained from ([I.22]), the effective masses for the conduction band m_e, and the heavy and light hole bands (respectively m_{hh} and m_{lh}) of unstrained material in the [100] direction are given in Table I-3.

	$Ga_yIn_{1-y}P$	$(Al_xGa_{1-x})_{0.516}In_{0.484}P$
m_e	$0.064 + 0.086.y$	$0.1079 + 0.036.x$
m_{hh}	$0.48 - 0.07.y$	$0.4443 + 0.015.x$
m_{lh}	$0.14 + 0.02.y$	$0.1502 + 0.031.x$

Table I-3 Effective masses in units of free electron mass

•

I.3.2.7) Refractive indices

The refractive index *(n)* of AlGaInP compounds lattice-matched to GaAs has been characterised in [I.8] at room temperature:

$$n^2 - 1 = \frac{E_d}{E_0}\left[1 + \frac{E_p^2}{E_0^2} + \frac{E_p^4}{2E_0^2\left(E_0^2 - E_\Gamma^2\right)}.\ln\left(\frac{2E_0^2 - E_\Gamma^2 - E_p^2}{E_\Gamma^2 - E_p^2}\right)\right] \qquad (I.36)$$

where E_Γ is the direct bandgap energy, E_p is the photon energy, and E_0 and E_d are fitting parameters that are determined by fitting (I.36) to experimental measurements of the optical index versus photon energy. The values of the different parameters for lattice matched $Al_xGa_{1-x}InP$ reported in [I.8] are:

$$E_\Gamma = 1.89 + 0.67.x \ (eV) \qquad (I.37\ a)$$

$$E_0 = 4.17 + 0.49.x \ (eV) \qquad (I.37\ b)$$

$$E_d = 35.79 - 1.16.x \ (eV) \qquad (I.37\ c)$$

The authors used a value for the direct bandgap (I.37 a) which is slightly different to that of equation (I.34), and which shall be used when calculating the refractive index.

I.3.2.8) Momentum matrix element

The interband momentum matrix element $|M|$, defined later in section I.5.1.2), determines the optical interaction strength between conduction and valence states.

The recommended values for $|M|$ in [I.3] are given below.

For the binary compound InP:

$$\frac{2|M|^2}{m_0} = 20.7 \quad \text{eV} \tag{I.38}$$

For GaInP lattice-matched to GaAs, by linear interpolation between the binaries:

$$\frac{2|M|^2}{m_0} = 26 \quad \text{eV} \tag{I.39}$$

I.4. Quantum dot lasers

I.4.1 Self-assembled quantum dots

It was mentioned in section I.2.2 that it is possible to grow a thin epitaxial layer of material on a substrate with a slightly different native lattice parameter. If the layer is thin enough, the lattice mismatch is accommodated so that the in-plane lattice parameter adjusts to that of the substrate. After a critical thickness has been deposited, the formation of a two-dimensional layer is not favourable energetically and the strain relieves. One mechanism to relieve strain is the formation of dislocations as mentioned in section I.2.2, which generally have associated with them non-radiative recombination centres, leading to poor device performances. Another mechanism of strain relief in III-V compounds is the spontaneous formation of dislocation-free or "coherent" three-dimensional islands, via the Stranski-Krastanow (SK) mode ([I.9]), in which the strain is partially relieved. This type of island is called self-assembled.

If the material forming the islands has a smaller bandgap than the surrounding material, the electrons and holes can be quantum mechanically confined in all three directions. The islands are generally called quantum dots when they are small enough that the confined states are well separated in energy, leading to a so-called discrete density of states like in an individual atom.

I.4.2 Advantages and issues associated with quantum dot (QD) lasers

Theoretical implications of using quantum dots as the active material in a diode laser were considered in 1982 by Arakawa and Sakaki ([I.10]). They were predicted to present many advantages over bulk or quantum well structures due to their discrete density of states, and some of these advantages are briefly introduced below.

In quantum well and bulk lasers, the states are spread over a continuum of energy states, giving rise to a broad spectrum of spontaneous emission. For laser application, only the transition participating to the lasing wavelength is useful, and most of the radiative recombination is parasitic. In an ideal quantum dot structure where all the dots are identical and where all the injected carriers are captured into the dots and recombine via the ground state, this parasitic recombination would be suppressed, leading to a strong reduction of the laser threshold.

However, it is well-known that an ensemble of self-assembled quantum dots presents size and composition fluctuations, which give rise to a broadened transition energy spectrum (inhomogeneous broadening). Additionally, the ground state energy is at finite energy from upper-lying states like excited states or the two-dimensional wetting layer continuum, where carriers can thermally escape and recombine. It results in an increase of the threshold current as well as increased temperature dependence compared to the ideal case of isolated dot states. To minimise threshold current and temperature dependence, the quantum dot ground states should be distant in energy from the excited states, and more importantly from any continuum of states, and exhibit small inhomogeneous broadening. It should however be mentioned that quantum dot lasers with a large amount of inhomogeneous broadening can be used at an advantage for ultra-short pulse generation due to the possibility of having a large gain bandwidth.

Another important advantage of the use of quantum dots for laser applications are that they give access to a wider range of material composition than quantum well structures to reach particular emission wavelengths, in particular by allowing the use of materials with greater lattice mismatch.

Quantum dot lasers have been explored extensively in the InAs/GaAs system because they extend available GaAs-based devices to the technologically important 1.3 μm wavelength range. They have several advantages over the existing InP-based technology: GaAs substrates are cheaper, they offer the possibility of fabricating VCSELs, and QD devices could have better temperature stability that removes the need for the costly cooling system of telecom lasers. Very low threshold current 1.3 μm QD lasers have already been demonstrated to operate at room temperature under CW operation, with a threshold current density of 40 A/cm^2 reported reference [I.12] for a device with uncoated facets, and 20 A/cm^2 reported in [I.11] for a device with high-reflectivity coated facets.

I.4.3 InP / (Al)GaInP quantum dot lasers

The InP/(Al)GaInP quantum dot system has also aroused some interest, although literature on the subject is much less abundant than in the InAs/GaAs system. Interest for laser application in this material system is motivated on one hand by the general potential benefits of quantum dot lasers brought by zero-dimensionality, and on the other hand, by the possibility of extending the upper wavelength limit of conventional compressively strained GaInP quantum wells from 690 nm to the region of 750 nm, above which good performance AlGaAs laser diodes are available.

The InP lattice parameter is bigger than GaAs by 3.7% and it can form dots in the SK mode when deposited on GaAs-lattice-matched (Al)GaInP. The earliest reported results on growth and characterisation of quantum dots in the InP/(Al)GaInP system were produced about a decade ago by different research groups ([I.13], [I.14], [I.15]). Room temperature optically-pumped laser action was achieved in 1996 from MBE-grown samples, at a lasing wavelength of 704 nm ([I.16]), and laser action under electrical injection at room temperature has been reported more recently for samples grown by both MOVPE and MBE in the wavelength range between 645 nm and 750 nm ([I.17], [I.18]). All results reported in the literature have threshold current densities in excess of 1 kA/cm^2.

I.5. Optical gain and emission in III-V semiconductors

The theory outlined in this section, that supports the work later in the thesis, has been mostly distilled from reference [I.19], with addition of the quantum dot case.

I.5.1 Radiative transition rate

I.5.1.1) Induced radiative transition rate for a two-level system

The semi-classical Hamiltonian of an electron in a static potential V in the presence of an external electromagnetic field is given by:

$$H = \frac{(\quad + e \quad)^2}{2m_0} + V(r) \tag{I.40}$$

where A is the (classical) vector potential and P the electron momentum.

In the weak field limit and if dephasing processes occur in a timescale much shorter than the transition process, one can derive from (I.40) an electronic transition probability per unit second induced by an electromagnetic field due to absorption/stimulated emission of photons. For a two-level electronic system, the transition probability per unit second from an occupied state ψ_1 to an empty state ψ_2 of energy difference $|\hbar\omega_2 - \hbar\omega_1| = E_{12}$, induced by a harmonic field of frequency ω, is:

$$W_{1\to2}(\hbar\omega) = \frac{2\pi}{\hbar}|H'_{12}|^2 L\ (E_{12} - \hbar\omega) \tag{I.41}$$

- H'_{12} determines the strength of interaction between the states and is given by:

$$H'_{12} = \frac{e}{2m_0}\langle\psi_1|\quad(r)\quad|\psi_2\rangle \tag{I.42}$$

where $\quad(r,t) = \quad(r)e^{j\omega t}$

- $L\ (E_{12} - \hbar\omega)$ is the lineshape function that takes into account the energy broadening of the transition due to a finite dephasing lifetime of the states. It is normalised to unity. In the limit of unbroadened electron states:

$$L\ (E_{12} - \hbar\omega) = \delta(E_{12} - \hbar\omega) \tag{I.43}$$

Equation (I.41) gives the rate from an occupied state ψ_1 to an empty state ψ_2. If the states have a probability f_1 and f_2 of been occupied, and that the occupation of the two states are **independent**, then the transition rate from state ψ_1 to state ψ_2 ($\psi_1 \rightarrow \psi_2$) is:

$$W_{1\to2}(\hbar\omega) = \frac{2\pi}{\hbar}|H'_{12}|^2 . L\ (E_{12} - \hbar\omega)[f_1(1 - f_2)] \tag{I.44}$$

I.5.1.2) Transition matrix element

This section gives the transition matrix element for optical transitions between a conduction and a valence band state of a direct semiconductor.

In the envelope function approximation, the matrix element $|H'_{12}|$ between states of the conduction and the valence bands is obtained by substituting the wavefunctions in equation (I.42) by $\psi_1 = u_c(r).F_c(r)$ and $\psi_2 = u_v(r).F_v(r)$. The vector potential can generally be considered as uniform or slowly varying over the spatial extent of the envelope functions, and H'_{12} (I.42) can be written as:

$$|H'_{12}|^2 = \left(\frac{e}{2m_0}.A_0\right)^2 .|M_T|^2 \qquad \text{(I.45)}$$

where A_0 is the vector potential amplitude.

and M_T is the transition matrix element, given by:

$$M_T = \langle F_c|F_v\rangle.\langle u_c|\hat{}\cdot\ \ |u_v\rangle$$

(I.46)

where $\langle F_c|F_v\rangle = \int_r F_c^*(r).F_v(r).d^3r$ is the envelope function overlap, which determines selection rules for the transition. In particular, it implies *k*-conservation in a bulk material and in the non-confined directions (*x* and *y*) of a quantum well. The second term in the product of (I.46) is:

$$\langle u_c|\hat{}\cdot\ \ |u_v\rangle = \frac{1}{V_{unit\ cell}}\int_{unit\ cell} u_c(r)^*(\hat{}\ \ \ )u_v(r).d^3r \qquad \text{(I.47)}$$

where ˆ is the unit polarisation vector.

Introducing the momentum matrix element *M* between the conduction Bloch function and one of the "basis valence Bloch function" commonly labelled u_x, u_y and u_z (see for example Appendix 8 of reference [I.19]):

$$M = \langle u_c|\ \ |u_x\rangle \qquad \text{(I.48)}$$

$\langle u_c|\hat{}\cdot\ \ |u_v\rangle$ can be written in terms of *M*:

$$|\langle u_c|\hat{}\cdot\ \ |u_v\rangle|^2 = \kappa(\hat{e}).|M|^2 \qquad \text{(I.49)}$$

The coefficient $\kappa(\hat{e})$ contains the polarisation dependence of the optical transition strength.

By substitution in (I.43), the induced transition probability rate from a state "1" of the conduction band to a state "2" of the valence band can be written:

$$W_{1\to 2}(\hbar\omega)=\frac{2\pi}{\hbar}\left(\frac{e}{2m_0}.A_0\right)^2 .\left|\langle F_c\,|\,F_v\rangle\right|^2\kappa(\hat{e})|M|^2.f_1(1-f_2).L\,(E_{12}-\hbar\omega) \tag{I.50}$$

I.5.1.3) Spontaneous emission rate

Spontaneous emission does not arise from a semi-classical treatment but requires a full quantum treatment of the electron and field. Spontaneous emission is equal to the downwards radiative transition induced by the electromagnetic field corresponding to one photon per optical mode.

The density of optical modes per unit volume (in each polarisation) is given by:

$$\rho_{opt}(\hbar\omega)=\frac{1}{3.\pi^2}.\frac{n_g.n^2}{(\hbar c)^3}(\hbar\omega)^2 \tag{I.51}$$

The vector potential amplitude A_0 associated with the energy of a single photon in a unit volume is:

$$A_0^{\;2}=\frac{2.\hbar}{n.n_g.\varepsilon_0.\omega} \tag{I.52}$$

Therefore by substitution in (I.50), the spontaneous emission rate spectrum in a given polarisation $\hat{e}$ is given by:

$$R_{sp}^{\hat{e}}(\hbar\omega)=\frac{4.n.\hbar\omega}{3.\pi.\hbar^2c^3.\varepsilon_0}.\left(\frac{e}{2m_0}\right)^2 .\left|\langle F_c\,|\,F_v\rangle\right|^2\kappa(\hat{e})|M|^2.f_1(1-f_2).L\,(E_{12}-\hbar\omega) \tag{I.53}$$

I.5.1.4) Value of the polarisation dependent coefficient κ

The value of coefficient κ defined by (I.49) for transitions between a conduction and a valence state, can be found for bulk material by expanding the heavy and light hole Bloch functions on the basis Bloch functions (u_x, u_y, u_z) ([I.19]), which gives for heavy holes:

$$\kappa(\hat{e})=\frac{1}{2}\left[1-\left|\hat{k}.\hat{e}\right|^2\right] \tag{I.54}$$

and for light holes:

$$\kappa(\hat{e})=\frac{1}{2}\left[{}^{1}\!/_{3}+\left|\hat{k}.\hat{e}\right|^2\right] \tag{I.55}$$

where $\hat{k}$ is a unit vector directed along the electron wavevector k.

In a quantum well, the band edge envelope functions are typically constructed from the superposition of two plane waves with quantised k vectors along z, (where z is perpendicular to the plane of the quantum well). Therefore for small in-plane wavevectors, the relative transition strengths are obtained ([I.19]) by substituting $\hat{k} = \hat{z}$ in (I.54) and (I.55), and the results are in Table I-4.

	Electric field polarisation ($\hat{e}$)	
	$\hat{x}$ or $\hat{y}$	$\hat{z}$
HH (heavy holes)	1/2	0
LH (light holes)	1/6	2/3

Table I-4: Relative transition strength $\kappa(\hat{e})$ for a quantum well in the (xy) plane, near the band edge.

I.5.2 Transition rates in quantum wells and quantum dot ensembles

Equation (I.50) gives the transition probability rate for a single electronic pair. To find the total transition rate from the conduction to the valence band, expression (I.50) should be summed over all the possible pairs, i.e. over all the conduction and valence states.

I.5.2.1) In a quantum well:

When summing (I.50) for a quantum well, it is unnecessary to consider pairs of states with different in-plane wavevectors since their envelope function overlap is nil. It is therefore common to introduce a reduced density of states function, which is equal to the number of transition pairs with same in-plane wavevector per unit area of the well and per unit energy.

The reduced density of states for one pair of subbands of a quantum well is:

$$\frac{1}{\rho_{red}(E)} = \frac{1}{\rho_c(E)} + \frac{1}{\rho_v(E)} \qquad \text{(I.56)}$$

In the effective mass approximation, it can be reduced to:

$$\rho_{red}(E) = \frac{m_{red}{}^*}{\pi\hbar^2} \quad \text{with} \quad \frac{1}{m_{red}{}^*} = \frac{1}{m_c{}^*} + \frac{1}{m_v{}^*} \quad \text{for } E > E_{c0} - E_{v0} \qquad \text{(I.57)}$$

where E_{c0} and E_{v0} are respectively the conduction and valence band edge energy for the considered subbands.

The occupancy probabilities f_c and f_v of the conduction and valence states are a function of the states' energies. In one pair of subbands, because of the conservation of the in-plane wavevector, the choice of the transition energy fixes the energies of the two states involved in the transition. Therefore the energy of the conduction and valence states can be written as a function of the transition energy *E*, and will be written as $E_c(E)$ and $E_v(E)$ respectively. The occupancy probabilities of the conduction and valence states associated with transition energy *E* are respectively written as $f_c(E_c(E))$ and $f_v(E_v(E))$.

Summing (I.50), the downward transition rate per unit area and unit energy for a pair of subbands of a quantum well in the (*xy*) plane, in the presence of an external harmonic field of frequency ω is:

$$W_{c\to v}(\hbar\omega)=\frac{2\pi}{\hbar}.A_0{}^2\left(\frac{e}{2m_0}\right)^2.\kappa(\hat{e})|M|^2|\langle F_c(z)|\,F_v(z)\rangle|^2\int_E \rho_{red}(E).f_c[E_c(E)]\{1-f_v[E_v(E)]\}L\,(E-\hbar\omega)dE \tag{I.58}$$

And from (I.53), the spontaneous emission rate spectrum from a single pair of subbands per unit area is:

$$R_{sp}^{\hat{e}}(\hbar\omega)=\frac{4n\hbar\omega}{3\pi\hbar^2c^3.\varepsilon_0}\left(\frac{e}{2m_0}\right)^2.\kappa(\hat{e})|M|^2|\langle F_c(z)|\,F_v(z)\rangle|^2\int_E \rho_{red}(E).f_c[E_c(E)]\{1-f_v[E_v(E)]\}L\,(E-\hbar\omega)dE \tag{I.59}$$

If several pairs of subbands are involved, (I.58) and must be summed over the pairs of subbands, with different envelope functions $F_c(z)$ and $F_v(z)$, and different functions $E_c(E)$ and $E_v(E)$.

I.5.2.2) In a quantum dot ensemble:

In the structures considered in this work, the quantum dots are distributed in the growth plane with a density *N* per unit area, therefore it makes sense to derive a transition rate per unit area as for the quantum well case. The expression of the transition rate given below relates to a particular pair of states; say the dots conduction and valence ground states.

Since the transition occurs between states in the same dots (otherwise the envelope function overlap is zero), and assuming that all the dots are identical with a ground transition energy E_0, the transition rate is just equal to *2.N* times equation (I.50) (the factor two takes into account spin degeneracy):

$$W_{c\rightarrow v}(\hbar\omega)=\frac{2\pi}{\hbar}.A_0^{\ 2}\left(\frac{e}{2m_0}\right)^2.\kappa(\hat{e})|M|^2|\langle F_c(r)|F_v(r)\rangle|^2.2N.f_c[E_c(E_0)]\{1-f_v[E_v(E_0)]\}L\ (E_0-\hbar\omega) \qquad (I.60)$$

where $\langle F_c(r)|F_v(r)\rangle$ is the overlap integral between the considered valence and conduction ground states in the same dot.

A real ensemble of quantum dots is subject to composition and size fluctuations giving rise in effect to a continuous distribution of transition energies (inhomogeneous broadening). $n(E)$ denotes the energy distribution of the ground states transitions, i.e. $n(E)$ is the number of transitions at energy transition E per unit area and unit transition energy associated with the dot ground states. $n(E)$ is generally well described by a Gaussian function. Assuming that for the ground state, all the dots have the same overlap integral, the transition rate per unit area and energy interval can be written:

$$W_{c\rightarrow v}(\hbar\omega)=\frac{2\pi}{\hbar}.A_0^{\ 2}\left(\frac{e}{2m_0}\right)^2.\kappa(\hat{e})|M|^2|\langle F_c(r)|F_v(r)\rangle|^2\int_E n(E).f_c[E_c(E)]\{1-f_v[E_v(E)]\}L\ (E-\hbar\omega)dE \qquad (I.61)$$

where it was also assumed that the occupancy probabilities can be written as a function of transition energy instead of the energy of the individual states. When the dots have identical transition energies we can write $n(E)=2.N.\delta(E-E_0)$ and recover equation (I.60).

The spontaneous emission rate spectrum per unit area from the same states is given by:

$$R_{sp}(\hbar\omega)=\frac{4n\hbar\omega}{3\pi\hbar^2c^3\varepsilon_0}\left(\frac{e}{2m_0}\right)^2.\kappa(\hat{e})|M|^2|\langle F_c(r)|F_v(r)\rangle|^2\int_E n(E).f_c[E_c(E)]\{1-f_v[E_v(E)]\}L\ (E-\hbar\omega)dE \qquad (I.62)$$

I.5.3 Modal gain in a slab waveguide structure

I.5.3.1) Guided modes of slab dielectric symmetric waveguide

I.5.3.1.1 Introduction

A symmetric slab dielectric waveguide is represented on Figure I-6. The index of the core and the cladding are respectively denoted by n_2 and n_1 ($n_2 > n_1$), and the waveguide core width by *2d*. The optical modes of the structure are found by solving Maxwell's propagation equation in each medium together with continuity of the fields and their derivatives at the interfaces.

Guided modes propagate in the (xy) plane and have a field amplitude profile along z. The guided modes are either transverse electric (TE) or transverse magnetic (TM). In the following x is taken as the propagation direction, so that TE and TM modes respectively have their electric and magnetic fields along the y-axis.

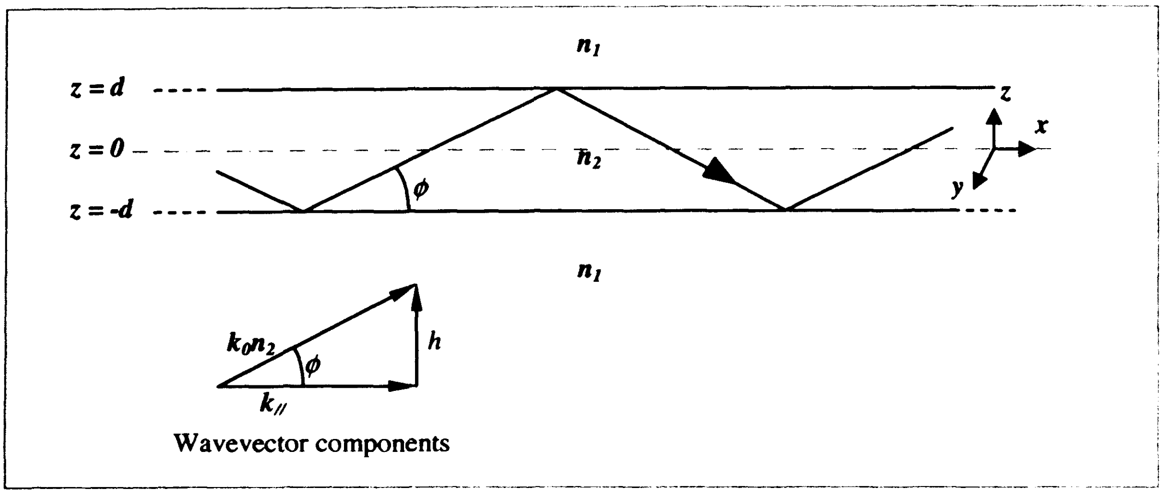

Figure I-6 Slab symmetric dielectric waveguide

I.5.3.1.2 TE_0 mode profile

The propagation equation of the electric field in a dielectric is:

$$\nabla^2 E(r) + k_0{}^2 n^2(r) E(r) = 0 \tag{I.63}$$

where k_0 is the wavenumber in vacuum and n is the index of refraction.

Denoting by $k_{//}$ the component of the wavevector along the x-direction in the waveguide, the guiding condition is:

$$k_{//} > k_0.n_1 \tag{I.64}$$

Angle ϕ is defined as represented in Figure I-6 :

$$\cos\phi = \frac{k_{//}}{n_2.k_0} \tag{I.65}$$

The guiding condition is thus equivalent to:

$$\phi < A\cos(n_1 / n_2) = \phi_c \tag{I.66}$$

ϕ_c is the total internal reflection angle at the $n_2 \rightarrow n_1$ interface.

Therefore, spontaneous emission emitted from the active region situated within the waveguide core is guided if it is emitted with an angle ϕ relative to the waveguide plane smaller than ϕ_c.

Due to the symmetry of the waveguide, the profile of the electric field for guided light is either odd or even along z; the lowest order mode is TE$_0$ even, and even TE modes are given by:

$$\begin{cases} E_y = A.\exp\left[-p.\left(|z|-d\right)-ik_{//}x\right] & for\ |z|\geq d \\ E_y = B.\cos(hz)\exp(-ik_{//}x) & for\ |z|\leq d \end{cases} \qquad (I.67)$$
$$with\ \ A = B\cos(hd)$$

where p and h are positive real parameters to be determined.

The phase index of the guided mode (or effective index) is given by:

$$n_{eff} = \frac{k_{//}}{k_0} \qquad (I.68)$$

Writing that the electric field (I.67) must satisfy the propagation equation and the continuity of the tangential component and derivative at the interface, it can be shown that:

$$\begin{cases} (pd)^2 + (hd)^2 = \left(n_2{}^2 - n_1{}^2\right)k_0{}^2.d^2 \\ pd = hd\tan(hd) \end{cases} \qquad (I.69)$$

and $k_{//}{}^2 = k_0{}^2 n_2{}^2 - h^2 = k_0{}^2 n_1{}^2 + p$ (I.70)

The first equality in (I.70) results in the right-angle triangle in Figure I-6, and from (I.68), the effective index of the guided mode is given by:

$$n_{eff} = n_2\sqrt{1-\frac{h}{k_0 n_2}} \qquad (I.71)$$

The system of equations (I.69) can be solved numerically to find coefficients h and d that determine the effective index from (I.71) and the field profile from (I.67) for even TE modes. The fundamental TE$_0$ mode has a parameter h falling within the range:

$$0 < hd < \frac{\pi}{2} \qquad (I.72)$$

The waveguide is monomode if:

$$0 < \sqrt{n_2^2 - n_1^2}.k_0.d < \frac{\pi}{2} \qquad (I.73)$$

I.5.3.2) Modal gain

The modal optical gain G is defined as the fractional increase in energy W_{EM} in an optical mode per unit length along the direction of propagation. If x denotes the direction of propagation:

$$G = \frac{1}{W_{EM}} . \frac{dW_{EM}}{dx} = \frac{n_g}{c} \frac{1}{W_{EM}} \frac{dW_{EM}}{dt} \tag{I.74}$$

In bulk material, the electromagnetic energy density per unit volume is:

$$W_{EM} = \left[\frac{1}{2} n.n_g \varepsilon_0 \omega^2 A_0{}^2 \right] \tag{I.75}$$

For a monomode slab waveguide device in which the light is confined along z and propagates along x, the energy stored in the guided mode, taking account of the full extent of the mode in the z-direction in an area $dx.dy$ is:

$$W_{EM} = \left[\frac{1}{2} n_{eff} n_g \varepsilon_0 \omega^2 \int A_0{}^2 (z) dz \right] dx.dy \tag{I.76}$$

and the rate of increase of W_{EM} is:

$$\frac{dW_{EM}}{dt} = \hbar\omega . \left[W_{c \to v}(\hbar\omega) - W_{v \to c}(\hbar\omega) \right] dx.dy \tag{I.77}$$

where $W_{c \to v}(\hbar\omega)$ and $W_{c \to v}(\hbar\omega)$ are the induced downward and upward transition rate per unit area in the considered guided mode.

Combining (I.74), (I.76) and (I.77), the modal optical gain is:

$$G(\hbar\omega) = \frac{2\hbar\omega}{n_{eff} c \varepsilon_0 \omega^2 \int A_0{}^2 (z) dz} . \left[W_{c \to v}(\hbar\omega) - W_{v \to c}(\hbar\omega) \right] \tag{I.78}$$

Quantum well case:

The expression of the modal gain spectrum for a quantum well structure in one subband is obtained by substituting (I.58) in (I.78):

$$G(\hbar\omega) = \frac{4\pi\hbar}{c \varepsilon_0 \hbar\omega . n_{eff} . L_{eff}} . \left(\frac{e}{2m_0} \right)^2 . \kappa(\hat{e}) . |M|^2 . |\langle F_c(z) | F_v(z) \rangle|^2 \int_E \rho_{red}(E) . \{ f_c[E_c(E)] - f_v[E_v(E)] \} . L\ (E - \hbar\omega) dE \tag{I.79}$$

where L_{eff} is the effective mode width defined by:

$$L_{eff} = \frac{\int A_0{}^2 (z) dz}{A_0 (z = 0)^2} \tag{I.80}$$

if the active region is at $z = 0$.

If more than one subband is involved in the process, the modal gain is obtained by summing (I.80) over the subbands.

Quantum dot case:

Similarly, for a single layer of dots at $z = 0$, the modal gain associated with the ground state is:

$$G(\hbar\omega) = \frac{4\pi\hbar}{c\varepsilon_0 \hbar\omega . n_{eff} . L_{eff}} \left(\frac{e}{2m_0}\right)^2 . \kappa(\hat{e}) |M|^2 |\langle F_c(r) | F_v(r) \rangle|^2 \int_E n(E) \{ f_c[E_c(E)] - f_v[E_v(E)] \} L\ (E - \hbar\omega) dE \tag{I.81}$$

I.5.4 Polarisation dependence of the transition strength

Coefficient $\kappa(\hat{e})$ characterises the polarisation dependence of the transition strength. For quantum well transitions near the band edges, the value of $\kappa(\hat{e})$ is given by Table I-4. With $\hat{e} = \hat{y}$ for TE modes and $\hat{e} = \hat{z}.\cos\phi + \hat{y}.\sin\phi \approx \hat{z}$ for TM modes for practical cases, the relative transition strengths of TE and TM modes for heavy and light holes transitions is directly given by Table I-4.

I.5.5 Quasi thermal equilibrium

The occupation probabilities f_c and f_v of the conduction and valence states can often be described using Fermi statistics by using a separate Fermi level for the conduction and valence states:

$$f_c(E) = \frac{1}{e^{(E-E_{Fc})/kT} - 1} \tag{I.82}$$

$$f_v(E) = \frac{1}{e^{(E-E_{Fv})/kT} - 1} \tag{I.83}$$

where E_{Fc} and E_{Fv} are the conduction and valence quasi-Fermi levels.

Neglecting the effect of the convolution by the lineshape function in (I.79) or (I.81), the modal gain $G(\hbar\omega)$ is positive when $\{f_c[E_c(\hbar\omega)] - f_v[E_v(\hbar\omega)]\}$ is positive.

Rearranging (I.82) and (I.83):

$$f_c[E_c(\hbar\omega)] - f_v[E_v(\hbar\omega)] = f_c[E_c(\hbar\omega)](1 - f_v[E_v(\hbar\omega)]) * \left[1 - e^{(\hbar\omega - \Delta E_F)/kT}\right] \tag{I.84}$$

with $\Delta E_F = E_{Fc} - E_{Fv}$ (I.85)

Therefore from (I.84), the modal gain $G(\hbar\omega)$ is positive when the quasi-Fermi level separation ΔE_F is greater than the considered photon energy $(\hbar\omega)$. This generally remains approximately true when including the lineshape function.

This chapter summarised the background theory and the material properties that will be referred to when interpreting the experimental results presented in this thesis. The next chapter describes the experimental techniques used to characterise the samples.

References

[I.1] "Visible Emitting (AlGa)InP Laser Diodes"
P.M. Smowton and P. Blood
chapter 9 in "Strained-layer quantum wells and their applications", edited by M.O. Manasreh, Gordon and Breach Science Publishers (1996)
[I.2] "AlGaInP quantum well lasers"
D.P. Bour
chapter 9 in "Quantum well lasers", edited by S.Zory, Academic Press (1993)
[I.3] "Band parameters for III-V compound semiconductors and their alloys"
I. Vurgaftman, J.R. Meyer and L.R. Ram-Mohan
Journal of Applied Physics **89** (11) pp 5815-5873 (2001)
[I.4] "Heterostructure lasers, Part A: fundamental principles"
H.C. Casey Jr and M.B. Panish
Academic Press, 1978
[I.5] "Growth temperature dependent atomic arrangements and their role on band-gap of InGaAlP alloys grown by MOCVD"
C. Nozaki, Y. Ohba, H. Sugawara, S. Yasuami and T. Nakanisi
Journal of crystal growth **93**, 406 (1988)
[I.6] "Substrate-driven ordering microstructure in $Ga_xIn_{1-x}P$ alloys"
P. Bellon JP. Chevalier, E. Augarde, JP Andre and GP Martin
Journal of applied physics **66**, p2388 (1989)
[I.7] "Bandgap of "completely disordered" $Ga_{0.52}In_{0.48}P$"
M.C. DeLong, D.J Mowbray, R.A. Hogg, M.S. Skolnick, J.E. Willims, K. Meehan, S.R. Kurtz, J.M. Olson, R.P. Schneider, M.C. Wu, M. Hopkinson
Applied Physics Letters **66** (23), pp3185-3187 (1995)
[I.8] "Refractive indices measurement of (GaInP)n/(AlInP)n quasi-quaternaries and GaInP/AlInP multiple quantum wells"
Y. Kaneko and K. Kishino
Journal of Applied Physics **76** (3), p1809 (1994)

[I.9] "Dislocation-free Stranski-Krastanow growth of Ge on Si (100)"
D.J. Eaglesham and M. Cerullo
Phys. Rev. Lett. **64**, 1943 (1990)

[I.10] "Multidimensional quantum well laser and temperature dependence of its threshold current"
Y. Arakawa and H. Sakaki
Applied Physics Letters **40**, 939 (1982)

[I.11] "Low-threshold oxide-confined 1.3-µm quantum-dot laser"
Gyoungwon Park; Shchekin, O.B.; Huffaker, D.L.; Deppe, D.G.;
Photonics Technology Letters, IEEE. Vol. **12** (3), March 2000, pp230 – 232

[I.12]: "1.3 µm InAs/GaAs multilayer quantum-dot laser with extremely low room-temperature threshold current density"
Sellers IR, Liu HY, Groom KM, Childs DT, Robbins D, Badcock TJ, Hopkinson M, Mowbray DJ, Skolnick AS
Electronics Letters **40** (22): 1412-1413 OCT 28 2004

[I.13] "Study of the two-dimensional–three-dimensional growth mode transition in metalorganic vapor phase epitaxy of GaInP/InP quantum-sized structures"
N. Carlsson, W. Seifert, A. Petersson, P. Castrillo, M. E. Pistol, and L. Samuelson
Applied Physics Letters – Dec. 12, 1994 - Volume **65** (24), pp. 3093-3095

[I.14] "Red luminescence from strain-induced GaInP quantum dots"
M. Sopanen, M. Taskinen, H. Lipsanen, and J. Ahopelto
Applied Physics Letters - Nov 25, 1996 – Vol. **69**, Issue 22, pp. 3393-3395

[I.15] "Electronic subband structure of InP/InxGa1-xP quantum islands from high-pressure photoluminescence and photoreflectance"
C. Ulrich, S. Ves, A. R. Goñi, A. Kurtenbach, K. Syassen, and K. Eberl
Phys. Rev. B **52** (16), 12212–12217 (1995)

[I.16] "Optical gain and lasing in self-assembled InP/GaInP quantum dots"
A. Moritz, R. Wirth, and A. Hangleiter, A. Kurtenbach and K. Eberl
Applied Physics Letters - July 8, 1996 – Vol. **69** (2), pp. 212-214

[I.17] "Room-temperature lasing via ground state of current-injected vertically aligned InP/GaInP quantum dots"
Y.M. Manz, O.G. Schmidt and K.Eberl
Applied Physics Letters – June 5, 2000 – Vol. **76** (23), pp.3343-3345

[I.18] "Visible spectrum (654nm) room temperature continuous wave InP quantum dot coupled to InGaP quantum well InP-InGaP-In(AlGa)P heterostructure laser"
G. Walter, N. Holonyak Jr, R.D. Heller and R.D. Dupuis
Applied Physics Letters – December 9, 2001 – Vol. **80** (24), pp.4604-4606
[I.19] "Diodes lasers and photonic integrated circuits"
L.A. Coldren and S.W. Corzine
Wiley Interscience (1995)
[I.20] "Wave mechanics applied to semiconductor heterostructures"
G. Bastard
Les éditions de physique (1988)
[I.21] "Band lineups and deformation potentials in the model-solid theory"
C.G. Van der Walle
Physical Review B, **39** (1989) pp 1871-1883
[I.22] "Heterojunction band offsets and effective masses in III-V alloys"
M Krijn
Semiconductor Science Technology, **6** (1991) pp.27-31

II. Experimental techniques

II.1. Device fabrication

The processing of the samples studied for this project was undertaken in the cleanroom facilities of Cardiff University by either GM Lewis, K Barnett or A Sobiesierski. The cleaving and mounting of the device was done by either GM Lewis or myself.

The samples studied in this project are grown on n-type substrates and are processed and mounted n-side down. They were fabricated into both or either laser and multisection devices.

II.1.1 Laser devices

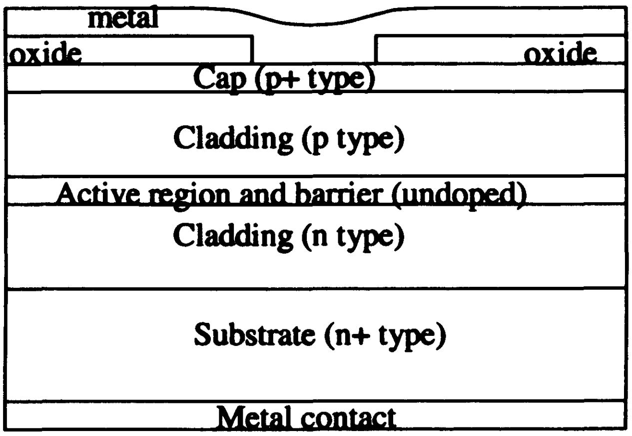

Figure II-1 Oxide stripe laser device seen from the facet

Fabricated laser chips are oxide isolated stripe devices as represented in the first chapter in Figure I-1, with a stripe width of 50 μm. The orientation of the stripe is such as to obtain (100) facets when cleaving perpendicular to the stripe axis. Figure II-1 is a more detailed representation of the structure seen from the laser facet.

The processing involves lithography, oxide deposition and etching, and metallization. The different steps have been described in detail in [II.1]. The samples were then cleaved in chips of cavity lengths ranging from 500 μm to 2 mm and mounted on copper heat sink holders using silver epoxy and gold wires.

II.1.2 Multisection devices

Multisection devices fabricated for the project are also based on oxide isolated stripe geometry with a stripe width of 50 μm. Figure II-2 is a diagram of a multisection chip. It is similar to an oxide stripe laser chip, but the top electrical contact is segmented into sections of 200 or 300 μm that can be electrically pumped separately. The sections are defined by chemically etching the metallic contact and the capping layer, which are highly conductive.

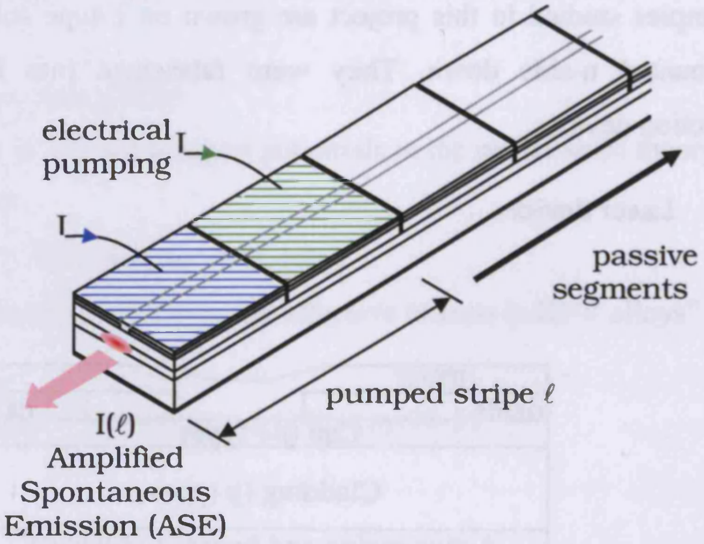

Figure II-2: Diagram of a multisection device

These devices are used to measure the single-pass Amplified Spontaneous Emission (ASE) in order to determine gain and absorption in the sample with the method explained later in section II.3. For this purpose it is essential to prevent the collection of light that travels more than one stripe length, in particular the light that is reflected on the back of the device and comes back to the front facet through which the light is collected. This is achieved by leaving several sections of unpumped material at the back of the device, which partially absorb the light, and by physically damaging the back facet to prevent internal reflection. Furthermore, the samples that have been studied in this project were grown off the (100) direction, and some multisection devices were processed so as to get angled facets in order to reduce the amount of light reflected back in the active region at both the front and the back facet.

II.2. Laser threshold from light-current charateristic

The system used to measure the LI characteristic of laser devices was built by K Griffiths and HD Summers. It is designed to perform automated gated measurements of the current-voltage (IV) and light-current (LI) characteristics of devices under pulsed excitation. For the measurements presented in this work, the diode lasers are driven in pulsed mode at 1 kHz repetition rate with a pulse width of 1 μs which is sufficiently low duty cycle to prevent heating of the sample.

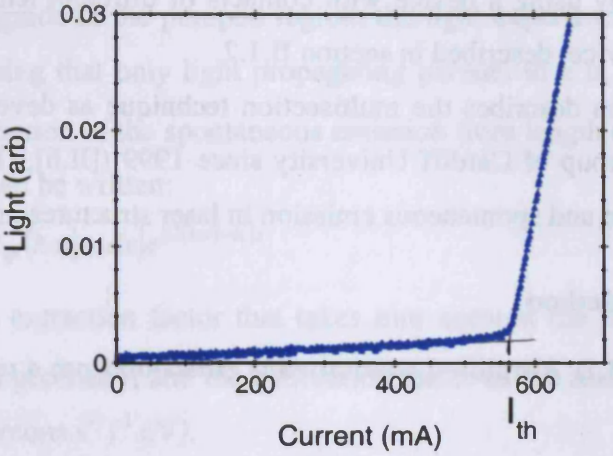

Figure II-3 Example of typical output power versus current curve for a diode laser.

Figure II-3 shows a typical measured L-I characteristic for a diode laser. It presents a clear change of slope, which corresponds to the threshold current, indicated by I_{th} on the figure. Below threshold, the internal radiative recombination is typically dominated by spontaneous emission, which increases with pumping power. When the round-trip amplification condition is met, the spontaneous emission becomes clamped and the increase of light out is due to stimulated emission.

II.3. Gain and emission spectrum measurement by the multisection technique

The multisection technique is a variation of the widely used "variable stripe length technique". It enables the modal gain to be extracted from the single-pass Amplified Spontaneous Emission (ASE) measured as a function of excitation stripe length. The first reported variable stripe length measurements were performed with optical excitation ([II.2], [II.3]) where the excitation beam is focused onto the sample surface so as to form a stripe of known length. Electrical excitation of several stripe lengths can be achieved by using a device with contacts of different lengths ([II.4]), or a segmented contact device, described in section II.1.2.

This section describes the multisection technique as developed by the optoelectronics research group of Cardiff University since 1999 ([II.6], [II.7], [II.5]), used to measure optical gain and spontaneous emission in laser structures under electrical injection.

II.3.1 Method

II.3.1.1) Amplified spontaneous emission from a uniformly pumped stripe

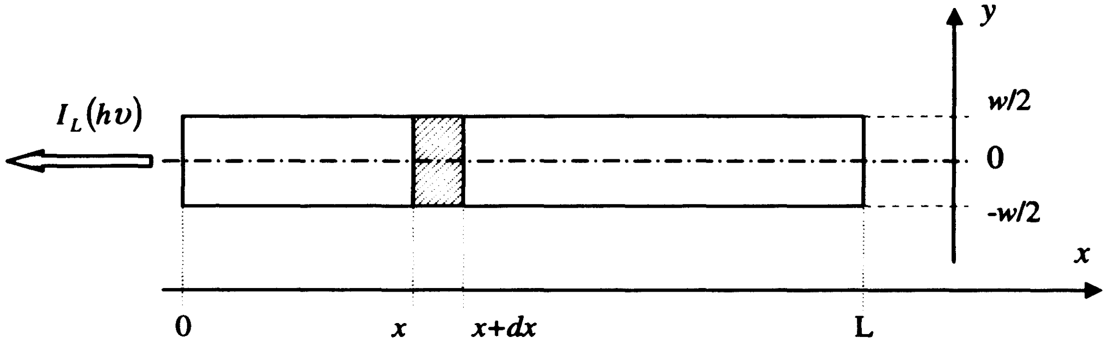

Figure II-4 Schematic diagram of the device stripe in the plane of the structure layers

Although the expression for the Amplified Spontaneous Emission (ASE) intensity is well known, it is derived in this section to make clear what the different quantities involved represent in view of the analysis presented later in chapter III. Only monomode planar waveguide devices are considered. The notations refer to those of Figure II-4. The x and y directions are in the plane of the structure layers, with x along the axis of the stripe and with the device facet at $x = 0$, and y perpendicular to it. The z-axis is perpendicular to the structure layers (i.e. along the growth direction). w denotes the stripe width.

The following gives a derivation of the expression of the ASE intensity spectrum $I_L(h\nu)$ in either the TE or the TM polarisations, collected from the end of a uniform pumped stripe of length *L*, assuming all the collected light is guided and that it travels parallel to the axis *x* of the stripe.

The spontaneous emission from length element [*x*, *x*+*dx*] of the stripe that couples to the waveguide:

$$dN(\hbar\omega) = \beta.R_{sp}(\hbar\omega).w.dx \qquad [\text{photons.s}^{-1}.\text{eV}^{-1}] \qquad (\text{II.1})$$

where β is the fraction of spontaneous emission that is guided. When propagating along *x* in the waveguide in the pumped region, the light experiences a net modal gain $[G(\hbar\omega)-\alpha_i]$. Assuming that only light propagating parallel to *x* in the guided mode is collected, the contribution of the spontaneous emission from length element [*x*, *x*+*dx*] to the measured ASE can be written:

$$dI_L(\hbar\omega) = F(\hbar\omega).\beta.[R_{sp}(\hbar\omega).w.dx].e^{[G(\hbar\omega)-\alpha_i]x} \qquad (\text{II.2})$$

where $F(\hbar\omega)$ is an extraction factor that takes into account the facet reflectivity, the stripe and collection geometry, and the calibration factor of the measurement apparatus in units of [(a.u).(photons.s^{-1})$^{-1}$.eV].

Integrating equation (II.2) along *x* gives:

$$I_L(\hbar\omega) = F(\hbar\omega)\beta.w.R_{sp}(\hbar\omega).\frac{e^{(G(\hbar\omega)-\alpha_i)L}-1}{G(\hbar\omega)-\alpha_i} \qquad (\text{II.3})$$

Substituting $C(\hbar\omega) = F(\hbar\omega).\beta.w$ (II.4)

$$I_L(\hbar\omega) = C(\hbar\omega).R_{sp}(\hbar\omega).\frac{e^{(G(\hbar\omega)-\alpha_i)L}-1}{G(\hbar\omega)-\alpha_i} \qquad (\text{II.5})$$

Similarly, when there is an unpumped section of length *L'* in front of the pumped section *L*, the ASE is multiplied by an exponential absorption factor and the expression for the measured ASE becomes:

$$I'_{L,L'}(\hbar\omega) = C(\hbar\omega).R_{sp}(\hbar\omega).\frac{e^{(G(\hbar\omega)-\alpha_i)L}-1}{G(\hbar\omega)-\alpha_i}e^{[-(\alpha(\hbar\omega)+\alpha_i)L']} \qquad (\text{II.6})$$

where $\alpha(\hbar\omega)+\alpha_i$ is the net modal absorption coefficient in the unpumped material.

Equation (II.5) is only valid for light propagating parallel to the stripe axis. Indeed for light propagating with non-zero angle in the (*xy*) plane, the path length of light emitted from a point at depth x to the end facet can be longer than x, modifying the exponential factor in (II.2). More importantly, the integration of equation (II.2) into (II.3) relies on the assumption that the extraction coefficient $F(\hbar\omega)$ in (II.2) is not a function of x; this is not true for any collection geometries.

How expression (II.5) extends to practical collection geometries is studied in chapter III.

II.3.1.2) Extraction of gain, loss and spontaneous emission

The net modal gain $(G-\alpha_i)$ and the spontaneous emission R_{sp} can be extracted from the ASE measured from the end of the device by fitting the dependence of the ASE over excitation stripe length L to (II.5). Similarly, the net modal absorption $(\alpha+\alpha_i)$ can be obtained by fitting the dependence of the measured ASE over the unpumped length L' to (II.6).

An oxide-stripe device where the top electrical contact is segmented in sections of identical lengths L, as described in II.1.2, is used to vary the excitation stripe length.

For measurements presented in this thesis, only the two first sections of the device are used, as represented in Figure II-5.

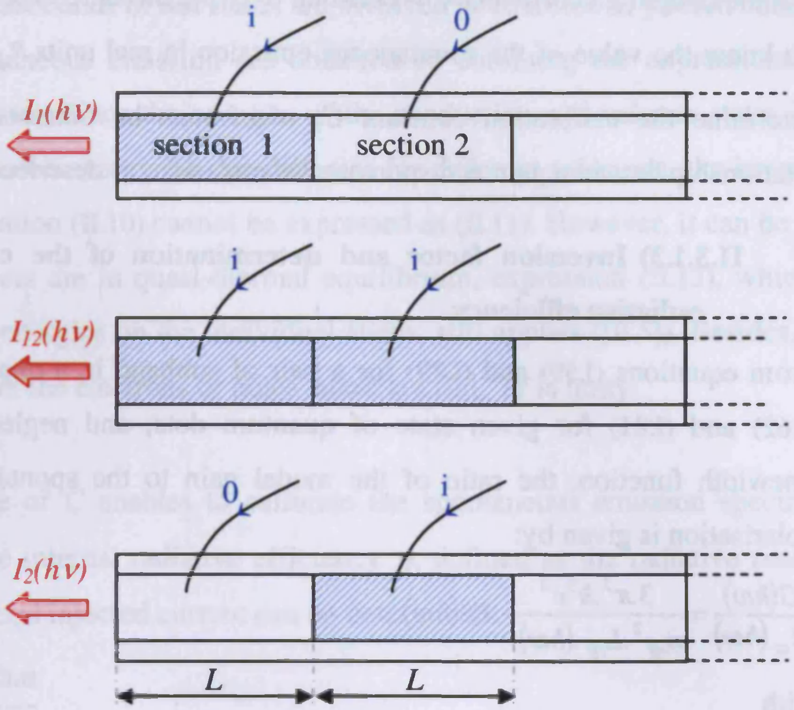

Figure II-5 Schematic diagram of the segmented contact device representing the measured ASE. The portion of the stripe under electrical excitation is hatched.

$I_1(h\nu)$ and $I_2(h\nu)$ denote the measured ASE spectra respectively when section 1 and section 2 are pumped separately, and $I_{12}(h\nu)$ the ASE spectrum when sections 1 and 2 are pumped together, at the same current density. Sections 1 and 2 are assumed to be identical: they have the same length L and produce the same gain and spontaneous emission when pumped with the same current.

From (II.5), the net modal gain of the pumped material is:

$$\boxed{G(\hbar\omega)-\alpha_i=\frac{1}{L}\ln\left(\frac{I_{12}(\hbar\omega)}{I_1(\hbar\omega)}-1\right)} \qquad \text{(II.7)}$$

And from (II.6), the net modal absorption of the unpumped material is given by:

$$\boxed{\alpha(\hbar\omega)+\alpha_i=-\frac{1}{L}\ln\left(\frac{I_2(\hbar\omega)}{I_1(\hbar\omega)}\right)} \qquad \text{(II.8)}$$

The spontaneous emission spectrum in arbitrary units can also be extracted from (II.5):

$$\boxed{I_{sp}(\hbar\omega)=C.R_{sp}(\hbar\omega)=\frac{1}{L}\ln\left(\frac{I_{12}(\hbar\omega)}{I_1(\hbar\omega)}-1\right)\frac{I_1(\hbar\omega)^2}{I_{12}(\hbar\omega)-2I_1(\hbar\omega)}} \qquad \text{(II.9)}$$

where the ASE spectra are assumed to be corrected for the spectral system response so that the coupling coefficient C is constant over the measured spectral range.

To know the value of the spontaneous emission in real units $R_{sp}(\hbar\omega)$, it is necessary to determine the calibration constant C, which can be obtained using a fundamental relationship between gain and spontaneous emission, as described in the next section.

II.3.1.3) Inversion factor and determination of the coupling constant and radiative efficiency

From equations (I.59) and (I.79) for a pair of subband in a quantum well or equations (I.62) and (I.81) for given state of quantum dots, and neglecting the effect of the linewidth function, the ratio of the modal gain to the spontaneous emission in one polarisation is given by:

$$\frac{G(\hbar\omega)}{R_{sp}(\hbar\omega)} = \frac{3\pi^2\hbar^3c^2}{{n_{eff}}^2.L_{eff}.(\hbar\omega)^2}.Pf(\hbar\omega) \tag{II.10}$$

with

$$Pf(\hbar\omega) = \frac{f_c(E_c(\hbar\omega)) - f_v(E_v(\hbar\omega))}{f_c(E_c(\hbar\omega))[1 - f_v(E_v(\hbar\omega))]} \tag{II.11}$$

Equation (II.10) is taken as the definition of the inversion factor Pf.

With $R_{sp}(\hbar\omega) = \frac{1}{C}.I_{sp}(\hbar\omega)$ and rearranging (II.10):

$$\frac{Pf(\hbar\omega)}{C} = \frac{G(\hbar\omega)}{I_{sp}(\hbar\omega)}.\left[\frac{{n_{eff}}^2.L_{eff}.(\hbar\omega)^2}{3\pi^2\hbar^3c^2}\right] \tag{II.12}$$

If the carriers are in quasi thermal equilibrium, from (II.11), and (I.84):

$$\frac{Pf(\hbar\omega)}{C} = \frac{1}{C}\left[1 - \exp\left(\frac{\hbar\omega - \Delta E_F}{kT}\right)\right] \tag{II.13}$$

The inversion factor spectrum is defined by (II.10) and determined experimentally from (II.12), where $G(\hbar\omega)$ and $I_{sp}(\hbar\omega)$ are respectively obtained from (II.7) and (II.9), and C is to be determined. Fitting to (II.13) with ΔE_F and C as fitting parameters gives the value of C, enabling the spontaneous emission spectrum to be calibrated

Even when the carriers are not in thermal equilibrium, it is possible to determine C if a spectral region can be identified where Pf should be unity, which happens if either the electrons or holes states are full from equation (II.11).

When several subbands or dot states are involved in emission at photon energy $\hbar\omega$, the gain and spontaneous emission are obtained by summing the expressions for single subbands or states. Since the energies of the conduction and valence states involved in transition at photon energy $\hbar\omega$ are different for different subbands, the inversion factor defined by equation (II.10) cannot be expressed as (II.11). However, it can be shown that when the carriers are in quasi-thermal equilibrium, expression (II.13), which does not depend on the energies on the individual states, still applies ([II.5]). Besides, it remains true that if either the electrons or holes states are full, Pf is unity.

The knowledge of C enables to calibrate the spontaneous emission spectrum in real units. Thus, the internal radiative efficiency η, defined as the radiative recombination current to the total injected current can be determined:

$$\eta = \frac{e\int R_{sp}(\hbar\omega)d\hbar\omega}{J} \qquad \text{(II.14)}$$

where $R_{sp}(\hbar\omega)$ is summed over all three polarisations and J is the injected current density.

II.3.1.4) Example of gain measurement

Figure II-6 represents an example of a set of ASE spectra (corresponding to $I_1(h\nu), I_2(h\nu)$ and $I_{12}(h\nu)$ with the previous notations) measured from a quantum well multisection device with sections of length 300 μm pumped at a current density of 2.5 kA/cm^{-2}.

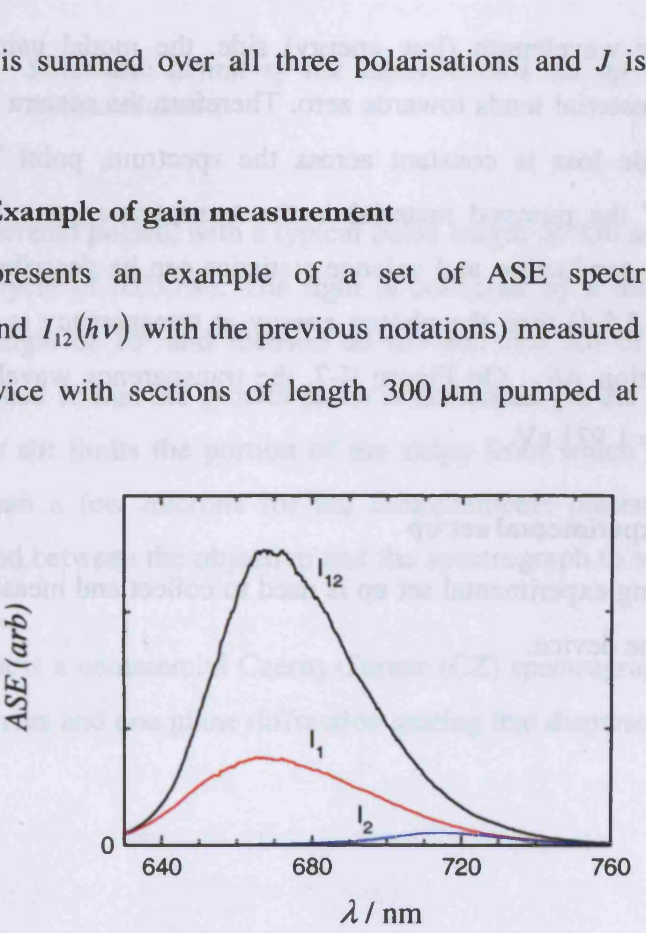

Figure II-6 ASE spectra I_{12}, I_1 and I_2 (respectively in black, red and blue)

Figure II-7 is the corresponding calculated value of net modal gain and net modal absorption obtained by applying equations (II.7) and (II.8).

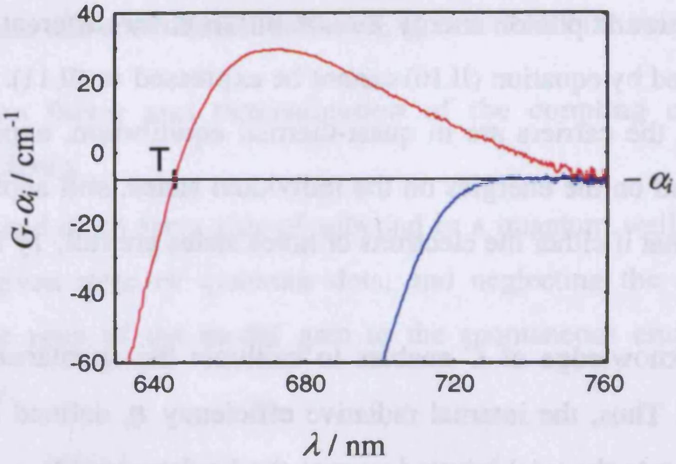

Figure II-7 *Net modal gain spectra of the pumped (red) and unpumped (blue) material*

On the long wavelength (low energy) side, the modal gain G of the pumped and unpumped material tends towards zero. Therefore the spectra tend towards ($-\alpha_i$). If the internal mode loss is constant across the spectrum, point T indicated on the gain spectrum of the pumped material is the transparency point, for which $G = 0$. If in addition the conduction and valence statistics can be described by Fermi distributions (see section I.5.4) then the photon energy at transparency is equal to the quasi-Fermi level separation ΔE_F. On Figure II-7, the transparency wavelength is 645.6nm, which gives $\Delta E_F = 1.921$ eV.

II.3.2 Experimental set up

The following experimental set up is used to collect and measure the ASE spectra from the end of the device.

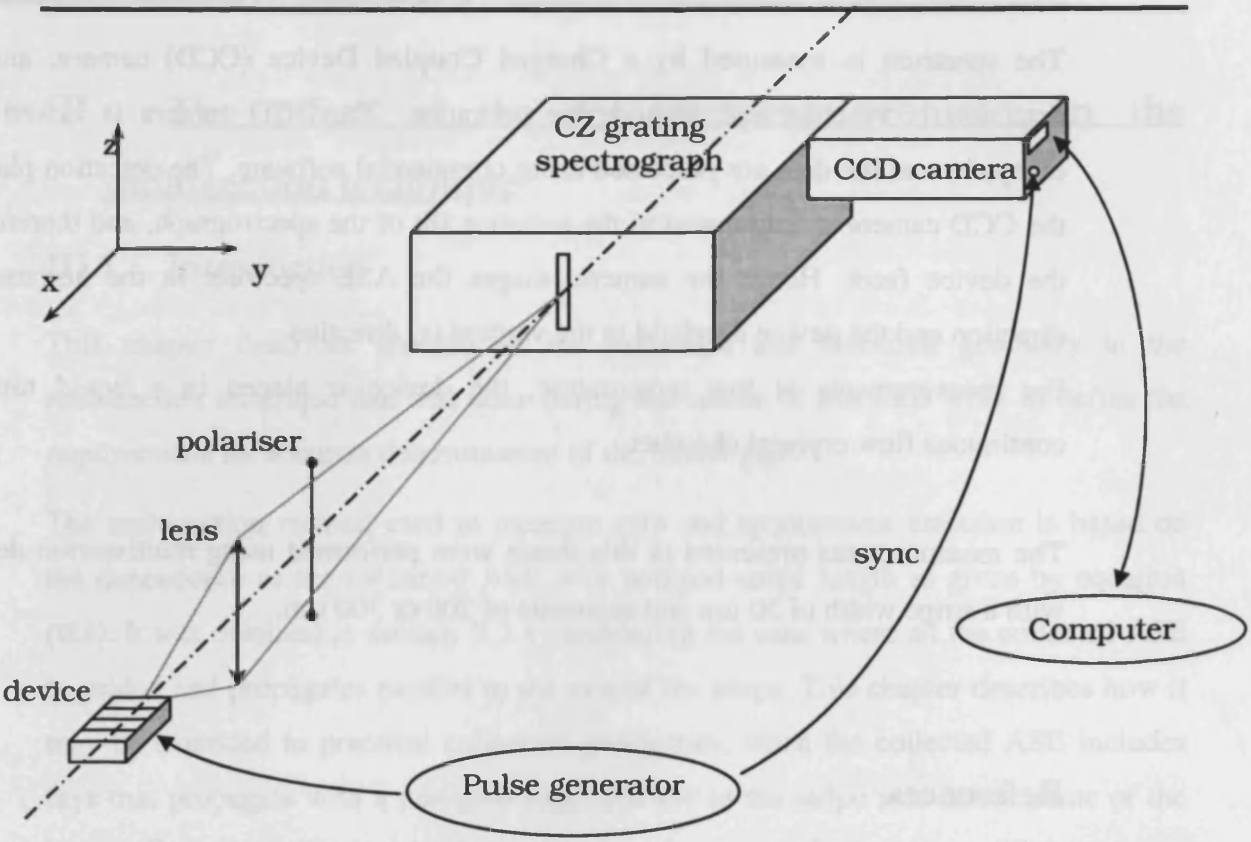

Figure II-8 *Schematic layout of the experimental set up used to perform gain measurements*

The device is operated pulsed, with a typical pulse length of 350 ns and a repetition rate of 1kHz (duty cycle of 0.035%). The light is collected by a microscope lens with a collection half-angle of 10º and focused on the entrance slit of a spectrometer. The device is positioned so that the growth plane is horizontal (in the (*xy*) plane), therefore the spectrometer slit limits the portion of the stripe from which the ASE is detected, typically less than a few microns for the measurements presented in this work. A polariser is placed between the objective and the spectrograph to select either the TE or TM polarisation.

The spectrograph is a commercial Czerny-Turner (CZ) spectrograph, which consists of two concave mirrors and one plane diffraction grating that disperses the light in the (*xy*) plane.

The spectrum is measured by a Charged Coupled Device (CCD) camera, and the detection is synchronised with device operation. The CCD camera is linked to a computer and the data are processed using commercial software. The detection plane of the CCD camera is conjugated to the entrance slit of the spectrograph, and therefore to the device facet. Hence the camera images the ASE spectrum in the horizontal y direction and the device nearfield in the vertical (z) direction.

For measurements at low temperature, the device is placed in a liquid nitrogen continuous flow cryostat chamber.

The measurements presented in this thesis were performed using multisection devices with a stripe width of 50 μm and segments of 200 or 300 μm.

References

[II.1]: H.D. Summers, "Strained laser $(Al_yGa_{1-y})_xIn_{1-x}P$ quantum well lasers, PhD thesis 1993

[II.2]: C.V. Shank, A. Dienes and W.T. Silvat, "single-pass gain of exciplex 4-mu and rhodamine 6G dye laser amplifiers", Applied Physics Letters **17**, 307-309, 1970.

[II.3]: K.L. Shaklee and R.F. Leheny, " Direct determination of optical gain in semiconductor crystals", Applied Physics Letters **18**, 475-477, 1971.

[II.4]: A. Oster, G. Erbert and H. Wenzel, "Gain spectra measurement by a variable stripe length method with current injection", Electronic Letters, **33**, 864-866, 1997.

[II.5] Blood P, Lewis GM, Smowton PM, Summers H, Thomson J, Lutti J, "Characterization of semiconductor laser gain media by the segmented contact method", IEEE Journal of Selected Topics in Quantum Electronics **9** (5), 1275-1282, 2003

[II.6] J.D. Thomson, H.D. Summers, P.J. Hulyer, P.M. Smowton, P. Blood, "Determination of single pass optical gain and internal loss using a multisection device", Applied Physics Letters, **75**, 2527-2529, 1999.

[II.7] G.M. Lewis, P.M. Smowton, J.D. Thomson, H.D. Summers and P. Blood, "Measurement of the true spontaneous emission spectra from the facet of diode lasers structures", Applied Physics Letters, **80**, 1-3, 2002

III. The effect of the measurement geometry in the multisection technique

III.1. Introduction

This chapter describes analysis of the excitation and detection geometry in the multisection technique that was done during the course of this PhD work to define the requirements for accurate determination of the modal gain.

The multisection method used to measure gain and spontaneous emission is based on the dependence of the measured ASE over pumped stripe length as given by equation (II.5). It was obtained in section II.3.1 considering the case where all the collected ASE is guided and propagates parallel to the axis of the stripe. This chapter describes how it may be extended to practical collection geometries, when the collected ASE includes rays that propagate with a non-zero angle relative to the stripe axis in the plane of the layers. The study is limited to planar single-mode waveguide structures with no guiding in the plane of the structure layers (*xy*) and under the assumption that all the collected light is guided.

In this chapter, I first describe qualitatively how the collection geometry should be limited so that the variation of the measured ASE with excitation stripe length follows that of equation (II.5) to a good approximation. I then calculate the measured ASE for a known collection geometry to quantify how it affects the result of a gain measurement. It is found that in order to minimise the measurement error, the nearfield and the collection angle must be limited interdependently, and that the use of inadequate collection geometry leads to an underestimation of the modal gain.

III.1.1 Measurement geometry

The collection geometry of the ASE from the facet of the device is determined by both angular and spatial limitation of the nearfield.

For illustration, a simple set up is represented on Figure III-1. $\mathcal{L}$ is a spherical lens collecting the light from the end of the device. Its numerical aperture and distance to the device determines the collection angle. The lens focuses the device facet onto a plane (P), where an aperture limits the portion of the device facet where the light is measured from (nearfield limitation). With the experimental set up of Figure II-8, (P) corresponds to the plane of the spectrometer entrance slit.

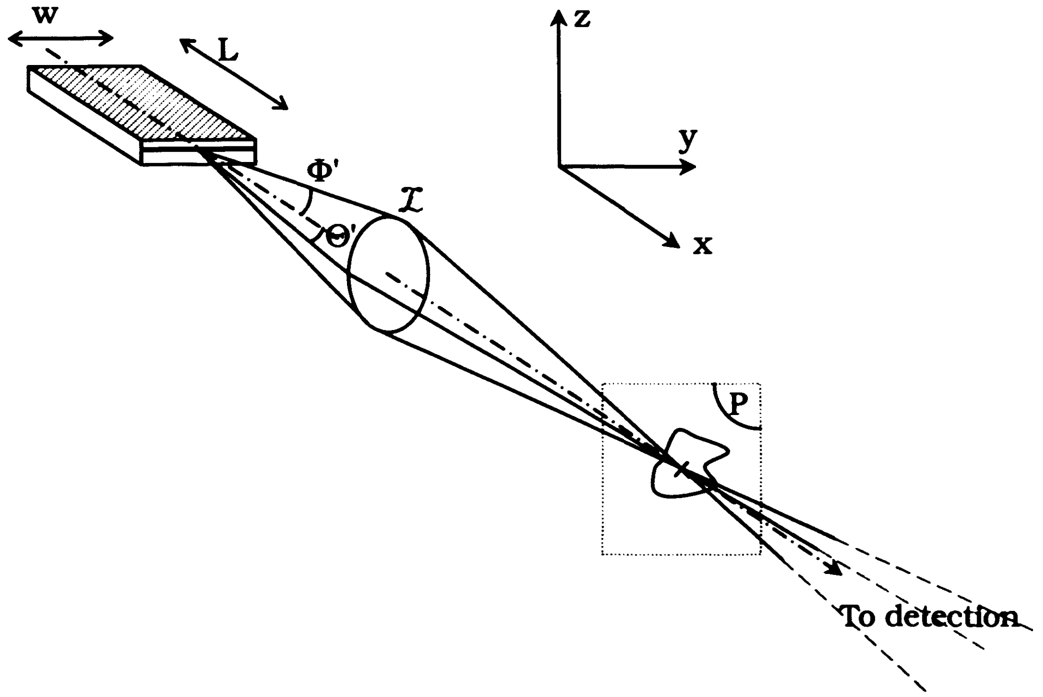

Figure III-1 Diagram of the collection geometry

More generally the collection half-angle in the horizontal (Θ') and vertical plane (Φ') can be different.

Collection geometry in the horizontal plane:

In the horizontal plane, the light is not guided and a geometrical optics approach is relevant. The collected ASE is a sum of rays spread in the (xy) plane, with different propagation angles θ and different exit points on the facet. The light is not diffracted in the (xy) plane at the device facet so that the propagation angle θ inside the device corresponds to a propagation angle θ' in air with $\sin\theta' = n.\sin\theta$ where n is the refractive index in the device. If Θ' denotes the collection half-angle in the (xy) plane, then it corresponds to an internal collection half-angle Θ with $\sin\Theta' = n.\sin\Theta$.

Collection geometry in the vertical direction:

Only planar monomode waveguide structures are considered and it is assumed that all the collected ASE is guided. Unguided light is emitted with an angle relative to the waveguide plane ϕ larger than the total reflection angle of the waveguide ϕ_c (I.66). Neglecting diffraction at the device/air interface for unguided light, it is emitted out of the device with an angle larger than ϕ_c' with $\sin\phi_c' = n.\sin\phi_c$. If the internal collection half-angle Φ in the vertical direction is less than ϕ_c, it is a good approximation that all the collected ASE is guided (and the nearfield of the device need not be limited along the z-direction). Therefore, as long as the collection half-angle is not bigger than ϕ_c, the collection geometry in the vertical direction does not cause the variation of the ASE over stripe length to deviate from (II.5).

If the waveguide is multimode, with say, two possible propagation angles, then the collected ASE cannot be written as (II.5) but is a summation of two terms with two different modal gains. In that case the measurement can only be performed if one can filter the different guided modes. Note that strictly speaking, there are usually two modes propagating in a monomode waveguide, corresponding to the TE and TM polarisations. However, these two modes can easily be separated with a polariser.

Assuming that all the collected ASE is guided, the calculation of the ASE in the device is a two-dimensional problem in the plane of the layers (*xy*). In the following I describe the effect of the collection geometry in the (*xy*) plane.

III.1.2 Qualitative description

The measurement of the gain using the multisection method is based on the dependence of the ASE upon excitation stripe length. It is necessary that, for a pumped stripe of length *L*, all the collected ASE has the same amplification path length *L* along which it experiences a net modal gain ($G - \alpha_i$).

III.1.2.1) Necessary limitation of the nearfield

Light that emerges from the device outside the pumped stripe width has been propagating through the unpumped material alongside the pumped stripe. In order to prevent its collection, it is necessary to limit the collected nearfield spatially to at most the pumped stripe, which can be done by using a suitable aperture in a plane conjugated to the device facet (P) as sketched on Figure III-1.

III.1.2.2) Necessary limitation of the collection angle

Following the statement made in III.1.2.1), the collection of the ASE is assumed to be limited to a portion of the stripe width. Then to prevent the collection of rays of which the path intercepts the edges of the stripe and do not have the whole amplification path length, the collection half-angle Θ in the plane of the layer (*xy*) must be limited as illustrated on Figure III-2 to at most Θ_{max}.

On the figure, L_{max} is the maximum excitation stripe length used for the experiment, *w* is the stripe width, and the light is collected from a central portion $\varepsilon.w$ of the stripe width ($\varepsilon < 1$).

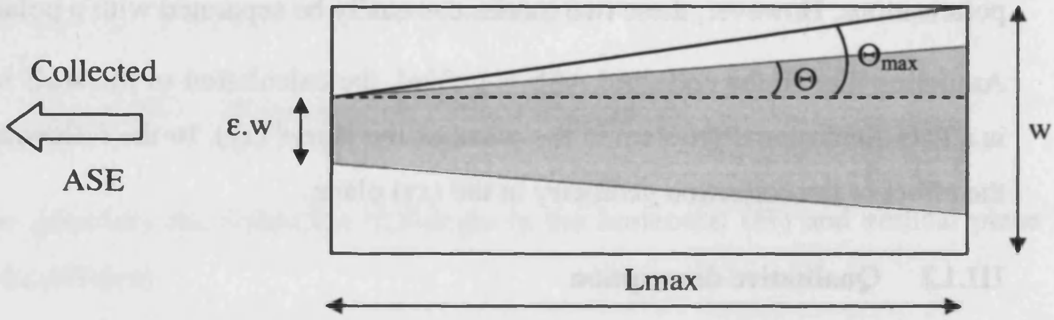

Figure III-2 Schematic representation of the stripe and a suitable collection geometry.

The collected rays are contained in the shaded region. The nearfield is limited to a portion ε.w of the stripe and the collection angle Θ is limited accordingly to a maximum of Θ_{max} so that rays of which the path intercepts the edges of the stripe are not collected.

Angle Θ_{max} represented on Figure III-2 is given by:

$$\Theta_{\max} = a\tan\left(\frac{(1-\varepsilon)w/2}{L_{\max}}\right) \tag{III.1}$$

Considering a plane (P) emitting light with uniform brightness, the amount of light that couples from plane (P) to point M within an angle Θ does not depend on the position of the plane as far as the collection cone does not meet the boundaries of the plane. Therefore if the collection geometry is as sketched on Figure III-2 with $\Theta < \Theta_{\max}$, the ASE is collected with uniform efficiency along the stripe, implying that the extraction coefficient $F(\hbar\omega)$ in equation (II.2) is not a function of x. Moreover if the collection angle is small, the path length of all the collected rays can be approximated to L. In those conditions the length dependence of the collected ASE follows that of equation (II.5) in good approximation.

III.2. Calculation of the measured ASE

All calculations of the ASE found in the literature are based on a point-source approach, meaning that for a given collection geometry, the measured ASE is evaluated numerically by summing the contribution of each point source of the stripe. Here, integration along the ASE path is included literally and the ASE is calculated by summing numerically over the facet of the device. It has the advantage of suppressing one integration variable and necessitating fewer approximations. It also enables nearfield limitations to be included explicitly.

Here only cases where the nearfield is limited to at most the pumped stripe width are considered, because it was already said that it is a necessary precaution for this experiment (III.1.2.1). The calculation can easily be extended if needed by introducing one more parameter which is the absorption coefficient of the unpumped material alongside the stripe.

III.2.1 Differential expression for the ASE inside the stripe.

In this section, I derive a differential expression for the ASE inside the stripe at the device facet ($x = 0^+$). All the collected ASE is assumed to be guided; therefore it is a two-dimensional problem.

The differential quantity $d^2\phi(\theta,y)$ indicated on Figure III-3 denotes the photon flux at the device facet inside the device ($x = 0^+$) across a length element *dy* of the facet, located by its *y*-coordinate from the centre of the stripe, and due to ASE propagating at an angle θ with the axis of the stripe, within dθ. It originates from spontaneous emission from the hatched area in Figure III-3.

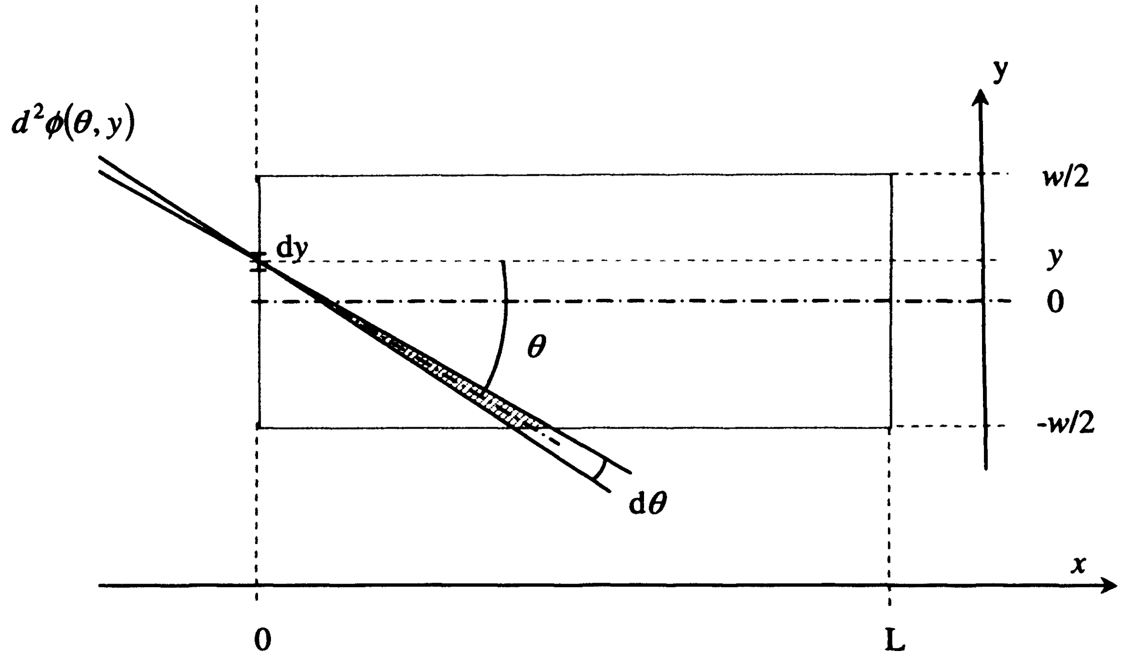

Figure III-3 Diagram representing the stripe in the (x-y) plane.

The light $d^2\phi(\theta,y)$ collected from a differential element dy of the facet within an angle $d\theta$ originates from the hatched area

As mentioned before, only collection geometries where the ASE is collected within the pumped stripe width are considered. Therefore the derivation of $d^2\phi(\theta,y)$ is restricted to $-{}^{w}\!/_{2} < y < {}^{w}\!/_{2}$. The expression obtained can easily be extended to $|y| > {}^{w}\!/_{2}$ by introducing the absorption coefficient in the unpumped region if needed.

The expression of $d^2\phi(\theta,y)$ is derived with the help of Figure III-4.

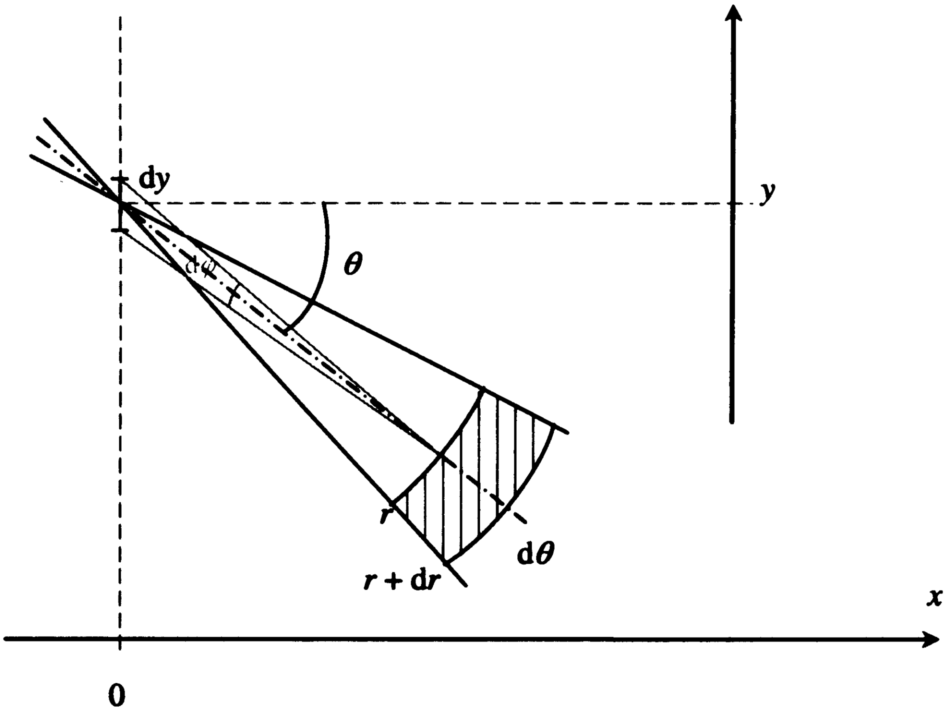

Figure III-4 *Representation of the ASE collection in the (x-y) plane. The hatched area represents the contribution to $d^2\phi(\theta,y)$ of an element of the stripe at distance between r and r+dr of the collection point*

The spontaneous emission emitted by the hatched area of Figure III-4 in all directions is $R_{sp}(h\nu).dr.rd\theta$. A fraction β of the spontaneous emission couples to the waveguide. A fraction $\frac{d\varphi}{2\pi}$ of it then couples to the length element of width dy. The differential angle $d\theta$ appears as a large quantity on Figure III-4 to make it readable.

Therefore the contribution of the spontaneous emission from the hatched area of Figure III-4 to $d^2\phi(\theta,y)$ at the facet is:

$$d^3\phi(\theta,y)=\beta.\frac{d\varphi}{2\pi}.Rsp.dr.rd\theta.e^{(G-\alpha_i)r} \tag{III.2}$$

Substituting $d\varphi=\left(\frac{dy}{r}\right)\cos\theta$:

$$d^3\phi(\theta,y)=\beta.\frac{dy}{2\pi}.\cos\theta.R_{sp}.dr.d\theta.e^{(G-\alpha_i)r} \tag{III.3}$$

Integrating over r gives:

$$d^2\phi(\theta,y)=\beta\frac{\cos\theta}{2\pi}.R_{sp}.\frac{e^{(G-\alpha_i)\ell(\theta,y)}-1}{G-\alpha_i}.dy.d\theta \tag{III.4}$$

where $\ell(\theta,y)$ is the path length of the ASE in the stripe.

Considering Figure III-5, $\ell(\theta,y)$ is given by:

$$\begin{cases} \ell(\theta,y)=\dfrac{w/2+y}{\sin\theta} & \text{if } \theta<\theta_1 \\ \ell(\theta,y)=\dfrac{L}{\cos\theta} & \text{if } \theta_1<\theta<\theta_2 \\ \ell(\theta,y)=\dfrac{w/2-y}{\sin\theta} & \text{if } \theta>\theta_2 \end{cases} \quad \text{with} \quad \tan\theta_1=\frac{w/2+y}{L}, \quad \tan\theta_2=\frac{w/2-y}{L} \tag{III.5}$$

where θ is signed in the trigonometric orientation.

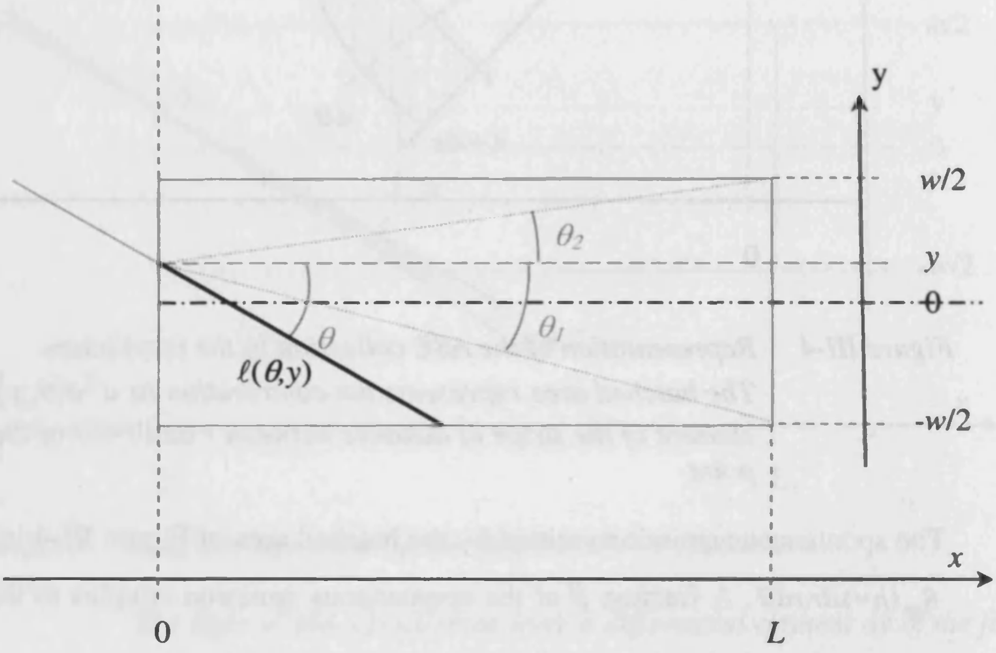

Figure III-5 Diagram representing the stripe in the (x-y) plane.

Equation (III.4) with (III.5) gives a differential expression of the ASE at the facet inside the sample, for light propagating towards the facet. It can easily be modified to account for ASE flux at any position x in the stripe and include light propagating away from the facet. Integration over all angles θ and across the stripe width gives the total ASE flux at any position x in the stripe. For the purpose of the present study, the expression of the ASE is used to calculate the collected ASE, and (III.4) is summed over θ and y depending on the collection geometry.

III.2.2 Differential expression for the measured ASE

Equation (III.4) gives a differential expression for the ASE at the device facet inside the device, at a given propagation angle θ and at a position y on the device facet. It contributes to the measured ASE with an additional dependence on θ and y:

$$d^2I(\theta,y)(h\nu)=F(\hbar\omega,\theta,y)d^2\phi(\theta,y) \tag{III.6}$$

The extraction coefficient F takes into account the collection geometry, (as well as the reflection at the facet and the sensitivity of the detection apparatus).

One can refer to Figure III-1 for a representation of the measurement geometry.

Dependence of F over y:

In practical applications, the limited nearfield is small compared to the working distance of the collecting optics and/or its diameter. In this case the collection angle Θ is constant over the device nearfield (i.e. Θ is not dependent on y). Thus the dependence of F upon y is only determined by the limitation of the nearfield in plane (P). For example if the nearfield is limited by a vertical slit in plane (P) that limits the nearfield to a central portion α of the stripe, then

$$H(y)=\begin{cases}1 & \text{for } |y|\le\alpha\,{}^{w}\!/_{2}\\ 0 & \text{for } |y|\ge\alpha\,{}^{w}\!/_{2}\end{cases} \tag{III.7}$$

Dependence of F over θ:

The dependence of F over θ is primarily dependent on the collection aperture of the lens in the (xy) plane (Θ'), but is also affected by the vertical collection angle (Φ') due the diffraction at the device facet in the z-direction.

For the calculation it is assumed that the intensity of the collected ASE is constant along z over the spatial extent of the collecting optics due to diffraction. In this case the fraction of collected ASE is proportional to the extent of the collecting optics in the z-direction.

If the collection lens is cylindrical with its axis along z, then the dependence of F upon θ is:

$$s(\theta)=\begin{cases}1 & \text{for } \theta\le\Theta\\ 0 & \text{for } \theta\ge\Theta\end{cases} \tag{III.8}$$

If the collection lens is circular, then with the notations of III.1.1, $s(\theta)$ is given by:

$$s(\theta)=\begin{cases}\cos\theta.\sqrt{1-\left(\tan\theta/\tan\Theta\right)^2} & \text{for} \quad \theta\leq\Theta \\ 0 & \text{for} \quad \theta\geq\Theta\end{cases} \tag{III.9}$$

A derivation of (III.9) is given in the appendix III.1 at the end of the chapter.

with $F(h\nu,\theta,y)=F(h\nu).s(\theta).H(y)$ (III.10)

The differential measured ASE is written as:

$$d^2I(\theta,y)(h\nu)=F(\hbar\omega).s(\theta).H(y).d^2\phi(\theta,y) \tag{III.11}$$

Or explicitly:

$$d^2I(\theta,y)(h\nu)=F(\hbar\omega).s(\theta).H(y).\beta\frac{\cos\theta}{2\pi}.\frac{e^{[(G-\alpha_i)(h\nu).\ell(\theta,y)]}-1}{(G-\alpha_i)(h\nu)}.R_{sp}(h\nu).d\theta.dy \tag{III.12}$$

Where $\ell(\theta,y)$ is given by expressions (III.4) and $s(\theta)$ is given by (III.5) for a circular lens with a collection angle smaller than the divergence of the ASE caused by diffraction at the end of the device, and $H(y)$ describes the nearfield limitations in the horizontal plane (i.e. along y) and is for example given by (III.7) if the nearfield is limited to a central portion of the stripe.

III.2.3 Integration

The measured ASE taking into account the full collection geometry is obtained by a numerical integration of (III.12), first over θ and then over y. This is a two-dimensional summation, whereas summing over contributions of points in the stripe would require a three-dimensional summation (x, y and θ).

III.3. Numerical simulation of a gain measurement

In this paragraph, I have applied the previous calculation to simulate the result of gain measurements performed with different measurement geometries.

III.3.1 Using the ASE measured from two stripe lengths

III.3.1.1) Simulation

This section deals with the case where the gain is extracted from the ASE measured from two excitation stripe lengths L and $2L$, as described in section II.3.1.

The measurement error $\Delta(G-\alpha_i)$ is defined as the difference between the measured net modal gain and its nominal value.

Results of measurement simulations for different collection geometries are represented on Figure III-6, which is a plot of the predicted error $\Delta(G-\alpha_i)$ as a function of the internal collection half-angle Θ, for three nominal values of the net modal gain: $(G-\alpha_i)=0\,\text{cm}^{-1}$, $-50\,\text{cm}^{-1}$ and $50\,\text{cm}^{-1}$, chosen to cover the range of gain values commonly measured. The simulated experimental conditions are as follows:

- the stripe dimensions are $w=50\,\mu\text{m}$ and $L=300\,\mu\text{m}$ as for most of the experimental data presented in this thesis,
- the internal collection angle Θ is determined by a circular lens so that the measured ASE is given by (III.7) and (III.5),
- the portion of the collected nearfield is aligned with the centre of the stripe. Its width is different for the three graphs of Figure III-6: it is infinitely narrow *(a),* equal to half of the stripe width *(b)* and to the whole stripe width *(c).*

For all three graphs, the prediction of the measured gain is equal to the nominal gain for $\Theta=0$.

The angles $\Theta_{\max}(2L)$ and $\Theta_{\max}(L)$, defined in section III.1.2.2), are represented on the graphs: $\Theta_{\max}(2L)$ [resp. $\Theta_{\max}(L)$] corresponds to the limit angle above which rays of which the paths intercept the edges of the stripe are collected when a stripe of length $2L$ [resp. L] is pumped. The values of $\Theta_{\max}$ are:

(a) $\Theta_{\max}(2L)=a\tan\left(\frac{w/2}{2L}\right)=2.4°$ $\quad\quad$ $\Theta_{\max}(L)=a\tan\left(\frac{w/2}{L}\right)=4.8°$

(b) $\Theta_{\max}(2L) = a\tan\left(\dfrac{w/4}{2L}\right) = 1.2^\circ$ $\Theta_{\max}(L) = a\tan\left(\dfrac{w/4}{L}\right) = 2.4^\circ$

(c) $\Theta_{\max}(2L) = \Theta_{\max}(L) = 0^\circ$

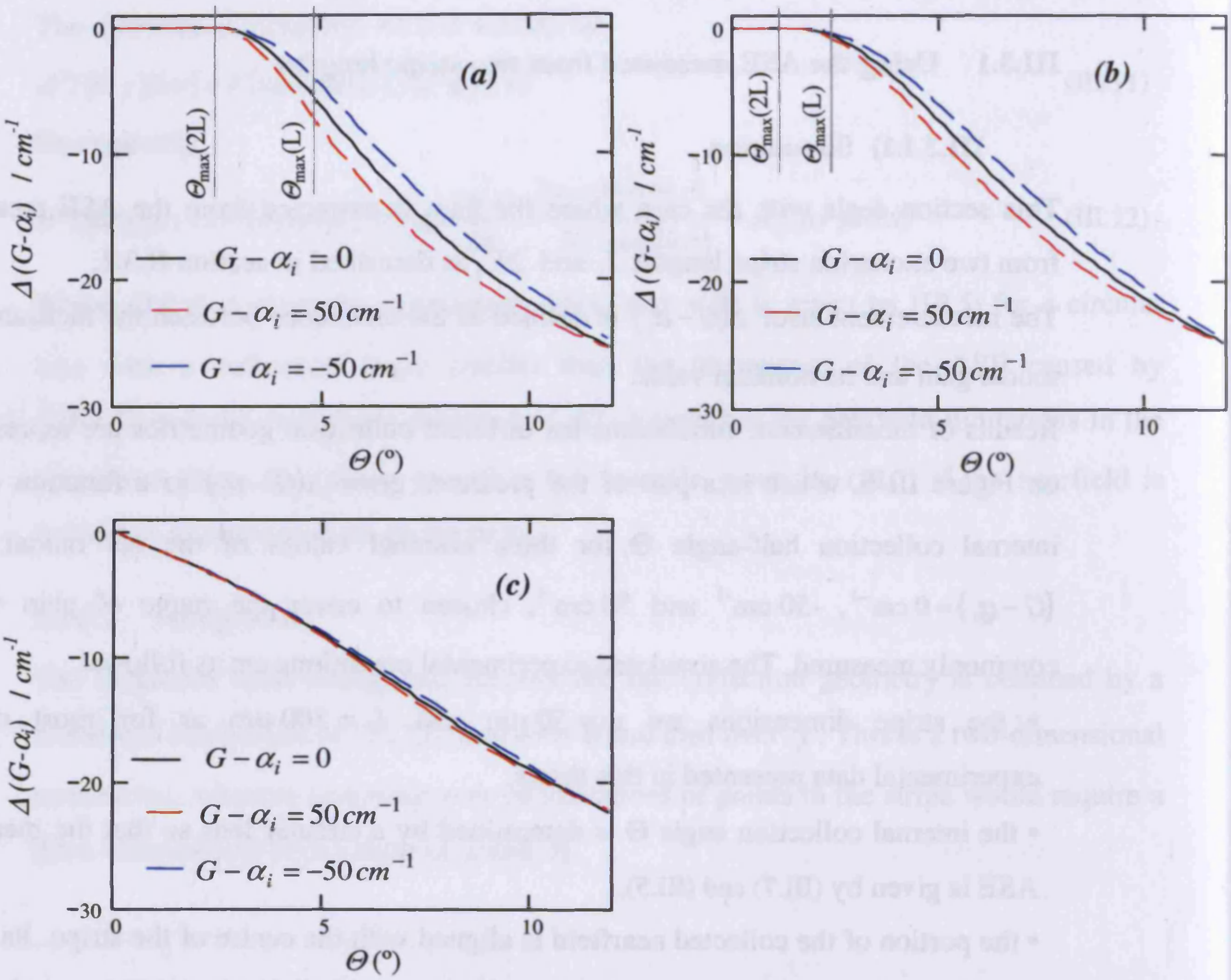

Figure III-6 Predicted measurement error $\Delta(G-\alpha_i)$ as a function of internal collection angle

(a) ASE collected from infinitely narrow portion of the nearfield, at the centre of the stripe

(b) ASE collected from half of the stripe width, at the centre

(c) ASE collected from the whole stripe

(i) For $\Theta < \Theta_{\max}(2L)$, the error in the measured gain is small (less than 0.01cm^{-1}) and cannot be seen at this scale on the graphs. It is due to small variations of path length inside the stripe with propagation angle.

(ii) As Θ is increased with $\Theta_{\max}(2L) < \Theta < \Theta_{\max}(L)$, all of the collected rays have the full path length when length L is pumped, but some have a shorter path length when $2L$ is pumped. Therefore I_{l2} is underevaluated compared to I_l and the gain obtained from (III.7) is underestimated, hence the negative value of $\Delta(G - \alpha_i)$.

(iii) When Θ is increased further, I_{l2} remains constant while I_l increases, therefore the calculated gain continues to decrease.

If the collection angle is too large, the calculated gain spectra are shifted down. Additionally, for a given collection aperture, $|\Delta(G - \alpha_i)|$ increases with $(G - \alpha_i)$, causing a relatively small distortion (compression) of the gain spectra. The predicted distortion is very small when the ASE is collected from the whole stripe width *(c)*.

III.3.1.2) Experimental check

In this section the previous predictions are checked experimentally by comparing the net modal gain measured with two different collection geometries. The device used is a 50 μm oxide stripe multisection device with 300 μm long sections. The net modal gain is determined from equation (III.7) using the ASE measured from the first two sections with the same current density. The measurement was performed using two different collection lenses giving internal collection half-angles Θ of 1.9° and 4.4°. For both measurements, the nearfield is limited to a narrow central part of the stripe (less than 5% of the stripe width). The result of the two measurements is given in Figure III-7. As might be expected after the calculations already described, the measured gain spectrum obtained with $\Theta = 4.4°$ is lower than that measured with $\Theta = 1.9°$.

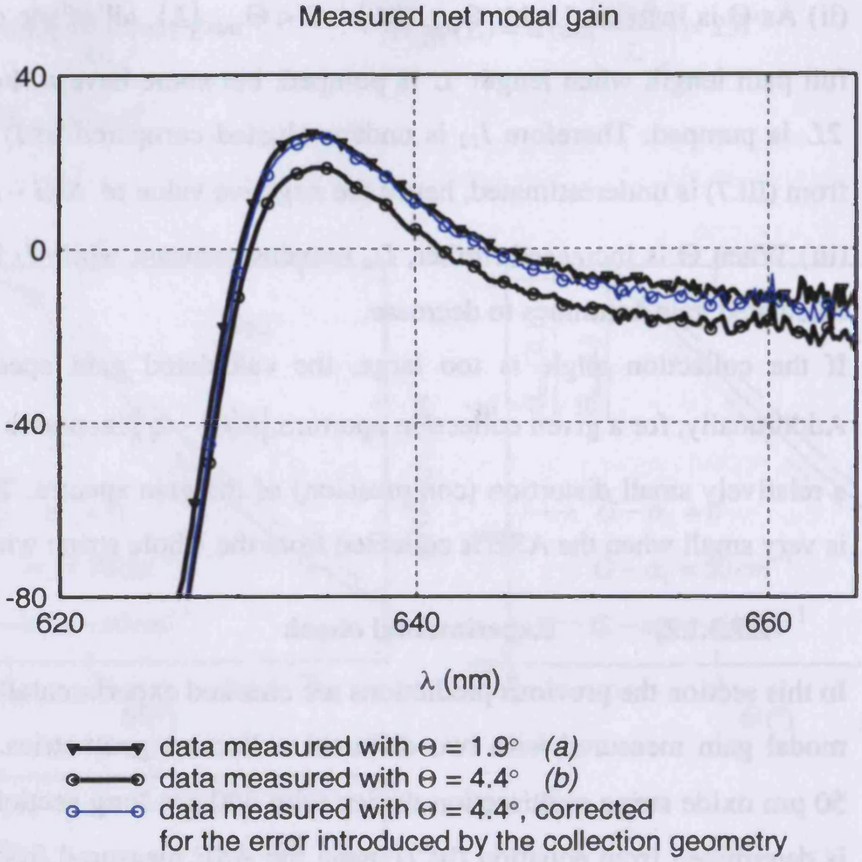

Figure III-7 Net modal gain measured using two different collection angles

The exact value of the predicted error associated with set up *(a)* and *(b)* is calculated as in III.3.1.1). It is negligible with the use of set up *(a)* (less than .01 cm^{-1}), whereas the use of set up *(b)* introduces a visible error. The gain spectrum corrected for that error is also plotted on Figure III-7. It agrees very well with the data measured with *(a)*, validating the analysis and demonstrating the importance of using a suitable collection geometry.

III.3.2 Using the ASE measured from several stripe lengths

In the previous section I studied the case where the gain is extracted from the measurement of the ASE from two stripe lengths and showed both by numerical simulation and experimentally that the use of an inadequate limitation of the collection angle and nearfield leads to an underestimation of the modal gain. One may wonder if some validation of the set up can be obtained by using a larger number of stripe lengths. In this section I simulate the case where the ASE is measured for a large number of pumped stripe lengths and the gain is determined by fitting the dependence of the ASE over length to equation (II.5).

Figure III-8 *(a)* and *(b)* show, on a semi-logarithmic scale, the predicted variations of the ASE intensity with increasing pumped length. Graphs *(a)* and *(b)* correspond to two different nearfield limitations. On each graph, the simulated measurement for different collection angles are represented by symbols, while the dashed line represents the variation expected from equation (II.5). The net modal gain is arbitrarily chosen at $G-\alpha_i = 10cm^{-1}$.

The simulated measurement geometry is as follows:
The stripe width is $w = 50$ µm.
In graph *(a)*, the ASE is collected from an infinitely narrow region at the centre of the stripe, and in graph *(b)*, it is collected from the whole stripe width. The internal collection angle Θ is determined by a circular lens so that the measured ASE is given by (III.7) and (III.5).and the measurements are simulated for $\Theta = 2$, 4 and 10° on both graphs. The symbols represent the result of simulated measurements when the pumped length is varied from 100 µm to 1.5 mm by sections of 100 µm, and the plain lines represent their best fit to equation (II.5).

For both graphs in Figure III-8, the simulated measurements (symbols) diverge from the nominal curves (dashed) rather drastically. However, it is possible to fit the data according to equation (II.5) quite nicely as indicated by the plain lines, which gives underestimated values for the net modal gain. The fitted values of the net modal gain thus obtained are listed in the table below for nominal net modal gain of 10 cm^{-1}.

	(a)	*(b)*
$\Theta = 2°$	7.91 cm^{-1}	6.38 cm^{-1}
$\Theta = 4°$	1.66 cm^{-1}	1.68 cm^{-1}
$\Theta = 10°$	-9.35 cm^{-1}	-7.95 cm^{-1}

Table III-1 *Values of the net modal gain obtained by fitting the data.*
The nominal value of the net modal gain is 10 cm^{-1}.

This result clearly shows that a good fit to equation (II.5) does not indicate correct collection geometry and does not validate the result of the measurement in that respect.

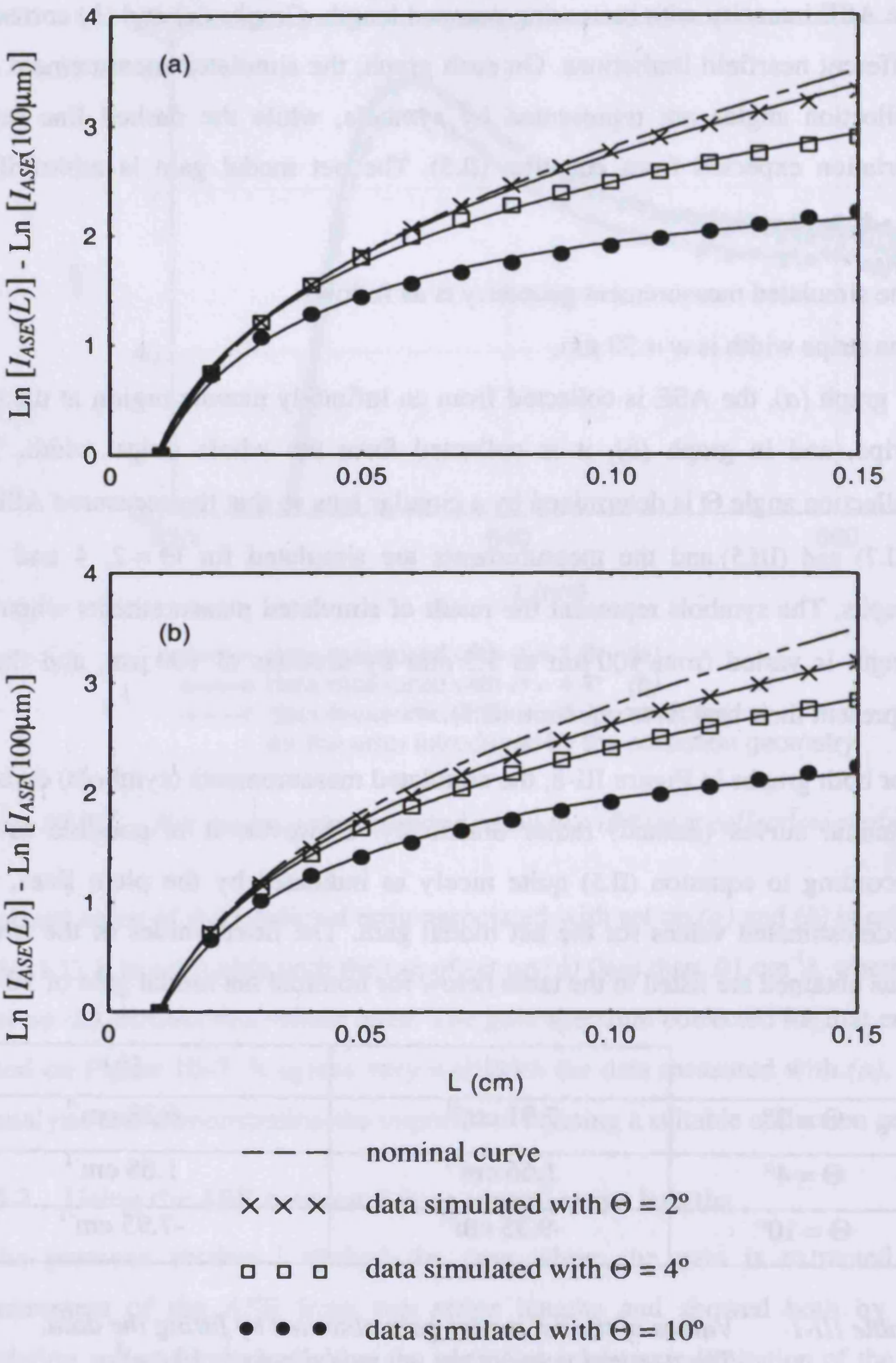

Figure III-8 Variation of the measured ASE intensity with pumped length L when the nearfield is limited to (a) *an infinitely narrow section at the centre of the stripe and to* (b) *the whole stripe width.*

Nominal gain: $G - \alpha_i = 10\,cm^{-1}$

III.4. Conclusions and practical implications

The effects of the collection geometry in determining the gain from the measurement of the Amplified Spontaneous Emission from a broad area device with no in-plane guiding, were described both qualitatively and quantitatively. It was shown that the ASE should be collected from a portion of the stripe width and that the collection angle should be limited accordingly so that the paths of the collected modes do not intercept the stripe edges.

To fulfil this condition, in the limit where the ASE is collected from a central and infinitely narrow portion of the stripe width, the collection angle inside the device in the plane of the waveguide shall be kept smaller than $\Theta_{max} = A\tan(w/2L_{max})$, where w is the pumped stripe width and L_{max} is the maximum pumped length. With w = 50 μm and L_{max} = 600 μm, it gives a maximum collection half-angle of 2.4° in the sample, or, taking into account refraction at the device facet, 8.4 ° in air for a sample with a refractive index of 3.5. If the ASE is collected from the full stripe width, the condition can be fulfilled only if the collection angle in the plane of the layers is zero, meaning that only rays propagating parallel to the stripe are collected.

In either case, if too large a collection angle is used, the measurement underestimates the net modal gain. When the gain is determined from the ASE emitted by two sections of length 300 μm and width 50 μm, the use of a large collection angle primarily causes the gain spectrum to shift down with a relatively small distortion of the shape, leading mainly to an overestimation of the optical scattering losses α_i. Besides, it was shown that when the ASE is measured from many pumped stripe lengths, the dependence of the ASE over stripe length still gives a good fit to equation (II.5), showing that the exponential variation of ASE intensity upon excitation stripe length cannot be taken as evidence of a correct collection geometry.

Several device-specific factors will modify the measurement error predicted by the simulation, such as current spreading and gain guiding. For example gain guiding (or other types of guiding in the lateral direction) would reduce the predicted error caused by using too wide a collection angle. Therefore the simulations made in this chapter cannot safely be used to correct for the error introduced by the collection geometry, despite an excellent agreement between simulation and experiment obtained in section III.3.1.2). Also, a misalignment of the device axis with that of the optical bench would introduce similar errors on the measurement of gain spectra.

The collection geometry used for the measurements presented in chapter IV to VI is that described in section II.3.2. The internal collection angle is about 3° and the ASE is collected from a central portion of the stripe of about 1μm. The multisection devices used in this thesis have a stripe width of 50 μm, the segments length is either 200 or 300 μm, and the gain and loss measurements are determined by using the ASE collected from the two first sections. Using the calculations performed in section III.3.1, the error in determining the gain (and loss) with this collection geometry is less than $1cm^{-1}$ for values up to $50\ cm^{-1}$.

Appendix III.1

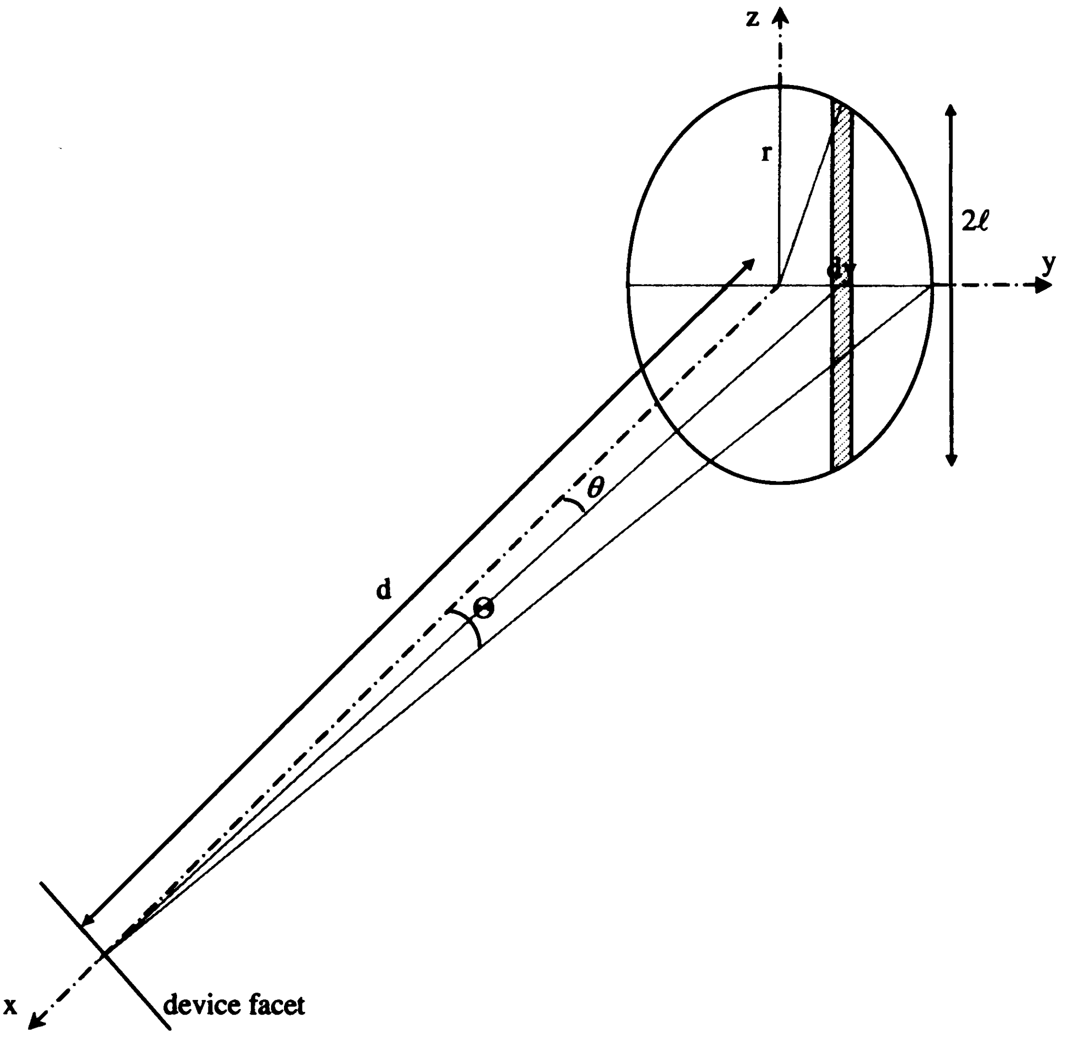

Figure III-9 : Diagram representing the collection of light from the device facet by a circular lens.

θ denotes the propagation angle of the light with the x-axis in the (x-y) plane and Θ' is the collection angle of the lens (i.e. the collection cone half-angle)

The collection efficiency in a small angle $d\theta$ is proportional to the hatched area on the figure, which is equal to $2\ell.dy$.

$\ell^2 = r^2 - y^2$ and $y = \frac{\tan\theta'}{\tan\Theta'}r$

Therefore $\ell = r.\sqrt{1-\left(\frac{\tan\theta'}{\tan\Theta'}\right)^2}$

Besides $dy = d.\cos\theta' d\theta'$

Therefore the collection efficiency of the lens varies with θ' as:

$$s(\theta')=\cos\theta'\sqrt{1-\left(\frac{\tan\theta'}{\tan\Theta'}\right)^2}$$

or expressed as a function of the angles in the sample:

$$s(\theta)=\cos\theta\sqrt{1-\left(\frac{\tan\theta}{\tan\Theta}\right)^2}$$

IV. InP/AlGaInP laser devices: structure and lasers

This chapter describes the layer structure of all the laser samples studied in this thesis, as well as threshold results measured on two of the samples. Optical properties of all samples are studied in more details in chapters V and VI.

IV.1. Laser heterostructures

InP quantum dots laser structures were designed by GM Lewis and PM Smowton in Cardiff University and grown by AB Krysa and JS Roberts in Sheffield University. They are double heterostructure lasers based on the GaInP/AlInP system, with the active region consisting of InP islands. They were grown by low pressure Metal-Organic Vapor Phase Epitaxy (MOVPE) on GaAs substrates with two orientations, the growth plane being either (211)B or (100) misoriented by 10° towards (111).

IV.1.1 Materials

The alloys used are listed in Table IV-1 together with some of their properties, obtained from the formulae given in section I.C. Apart from the InP dot material, the composition of the alloys was adjusted to be lattice-matched to the GaAs substrate.

Material	Use	Lattice parameter (Å)	Energy gap (eV)	Refractive index at 1.65 eV
GaAs	Contact layer	5.653	1.43	
$Al_{0.51}In_{0.49}P$	Cladding	5.653	2.35 (E_X)	3.10
$(Al_{0.3}Ga_{0.7})_{0.51}In_{0.49}P$	Barrier / Waveguide core	5.653	2.09	3.28
$Ga_{0.51}In_{0.49}P$	Quantum well	5.653	1.91	3.38
InP (unstrained)	Quantum dots	5.869	1.35	

Table IV-1 Alloys used to fabricate heterostructures and some of their properties

IV.1.2 Layer structure

The full layer structure is shown in Table IV-2. The active dot material in the devices was grown by depositing two monolayers (6Å) of InP on $Al_{0.3}Ga_{0.7}InP$ lattice-matched to GaAs and covering with GaInP without growth interruption. InP has a lattice parameter that is 3.7% larger than GaAs and nucleates in the Stranski Krastanow mode. Transmission Electron Microscopy (TEM) images made in Sheffield by AB Krysa on test structures showed that formation of quantum dots took place for a critical thickness of 1.6 monolayer (ML) and above. Several layers of dots are stacked in order to generate enough gain for laser operation, which is common for quantum dot laser structures. Indeed, in general, the amount of gain achievable with a single layer of dots is much lower than with a single quantum well, because of the combination of small dot density and large inhomogeneous broadening.

Layer	Nominal thickness (Å)	Material	Doping (cm^{-3})
cap	4000	GaAs	p, Zn, 10^{19}
cap	100	GaInP	p, Zn, 2.10^{18}
cladding	10000	AlInP	p, Zn, 5.10^{17}
barrier	920	$(Al_{0.3}Ga_{0.7})InP$	

×5

barrier	80	$(Al_{0.3}Ga_{0.7})InP$	
well	80	GaInP	
dots	6	InP	

barrier	1000	$(Al_{0.3}Ga_{0.7})InP$	
cladding	10000	AlInP	n, Si, 10^{18}
	100	GaInP	n, Si, 2.10^{18}
buffer	7000	GaAs	n, Si, 10^{19}

Table IV-2 Layer structure

The structures were grown at 690°C, which is the common growth temperature for AlGaInP, with the 5 repeats of the (dots/well/barrier) stack grown either at 650 or 690°C. The nominal rate of deposition of InP varies between 0.8 and 2.5ML/s.

The elements that differ between the structures are listed in Table IV-3.

Sample reference number	Deposition rate of InP (ML/sec)	Growth temperature of the stack (°C)
M1a - M1b	0.8	650
M2a – M2b	1.3	650
M3a - M3b	2.5	650
P3a	2.5	690

Table IV-3 Some growth conditions of the laser heterostructure

Letters "a" and "b" in the sample reference respectively designate a sample grown on (100) 10° off or (211)B substrate.

IV.1.3 Optical confinement

Neglecting the effect of the local index step due to the GaInP wells and InP islands, the optical modes are that of a symmetric slab waveguide (*see* section I.5.3.1)). I used a simple iterative routine to solve (I.69), and calculated the effective index, the mode profile and the effective mode width for TE_0 optical modes.

The overall waveguide core width is 275 nm. The refractive indices of the core and cladding are obtained from equation (I.36), which gives, at a photon energy of 1.65 eV, respective values of 3.28 and 3.09. Solving the TE_0 mode gives an effective index n_{eff} of 3.195 and an effective waveguide width L_{eff} of 282 nm.

The effective waveguide width L_{eff} is plotted on Figure IV-2 as a function of photon energy. The quantity $(n_{eff}.L_{eff}.\hbar\omega)$, which appears at the denominator in the expression of the modal gain (I.79) and (I.81) is also represented; it varies by less than 4% over the 1.55-1.75 eV energy range.

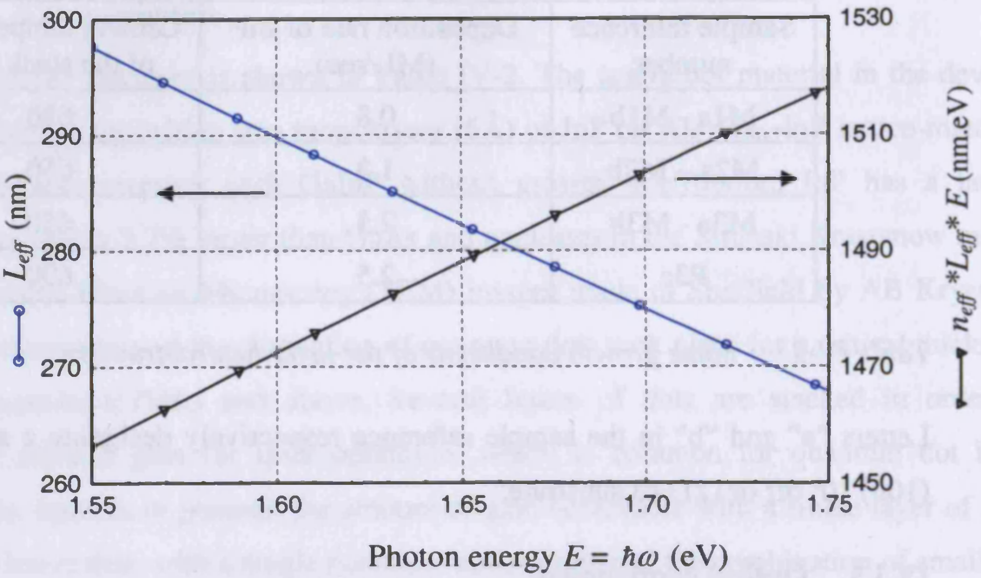

Figure IV-1 Effective waveguide width (L_{eff}) versus photon energy

IV.2. Laser measurements

On the basis of the gain data described in the chapter VI, laser devices were only fabricated from two samples: M1b and P3a. The samples were processed into oxide isolated stripe contact lasers with stripe width of 50 μm as detailed in section II.1.1, and cleaved to obtain cavity lengths ranging from 500 μm to 1.6 mm. The facets were left uncoated.

IV.2.1 Threshold current and lasing wavelength

Room temperature (295K) threshold current was measured as detailed in section II.2. The devices were operated pulsed with a repetition rate of 1kHz and excitation pulse duration of 1μs.

Sample M1b

Despite difficulties in cleaving the (211)B sample, GM Lewis succeeded in fabricating a 750 μm-long laser device with good quality facets by thinning the wafer. The device lased at room temperature (295-300K) at a wavelength of 688 nm (1.802 eV) for a current density of 2.4 kA.cm^{-2}.

The lasing wavelength is on the boundary of the targeted spectral range of [690-750 nm], and can be obtained from conventional compressively strained GaInP quantum well structures. However a longer device would have a longer lasing wavelength. Despite the (211)B wafers being difficult to handle, and probably not appropriate for commercial device production, this result demonstrates that working lasers can be produced.

Sample P3a

From sample P3a, devices with cavity lengths ranging from 500 μm to 1.6 mm were fabricated. Figure IV-2 gives examples of measured light-current characteristics of lasers for a few cavity lengths.

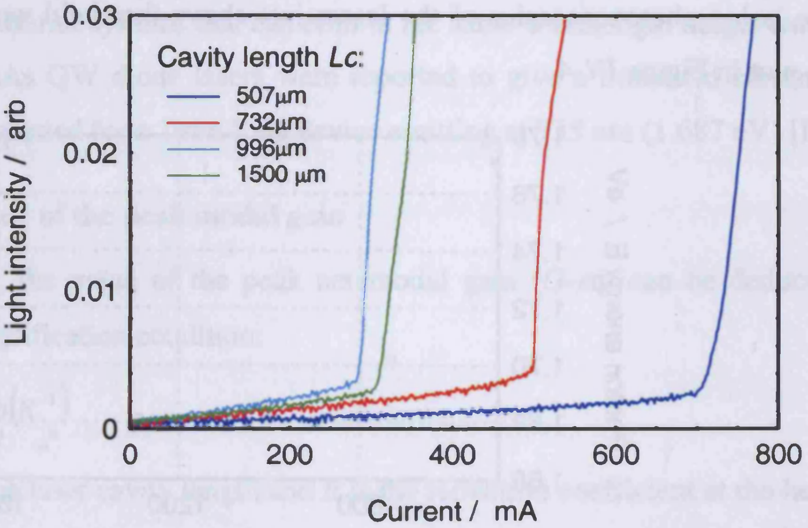

Figure IV-2 LI characteristics of laser devices from sample P3a

Looking at the time evolution of the light output along the excitation pulse, it was observed that lasing action at threshold occurs with a delay of 800 ns, which decreases as the current is increased. The cause of this behaviour is not obvious. However, ridge devices from the same sample, fabricated and measured in the University of New Mexico by Y Li, were not seen to exhibit such behaviour, while giving similar threshold current densities.

Figure IV-3 is a plot of the measured threshold current density J_{th} versus cavity length L_c. The current density was worked out from the injected current using the measured cavity length and an effective stripe width of 60 μm to take into account current spreading at the edges of the stripe as estimated by measurement of the nearfield.

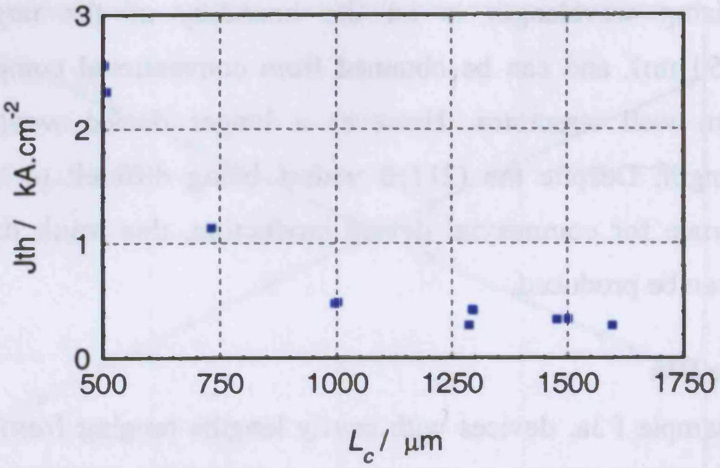

Figure IV-3 Threshold current density (Jth) vs cavity length (L_c) for sample P3a

The lasing photon energies of the lasers just above threshold were also measured and are plot in Figure IV-4

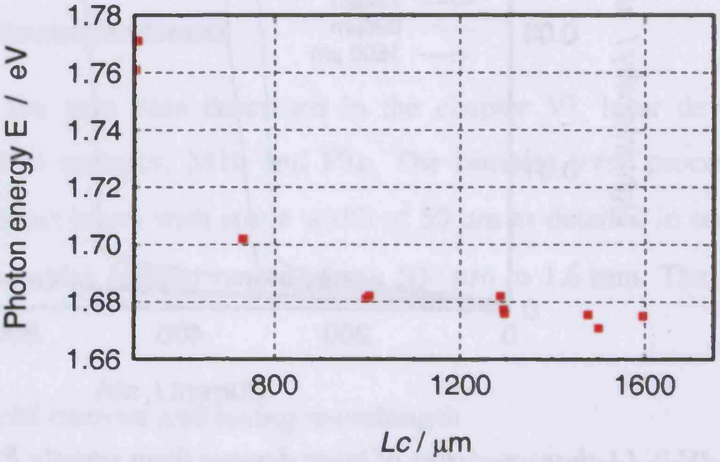

Figure IV-4 Lasing emission energy (E) vs cavity length (Lc) for sample P3a

IV.2.2 Discussion

The threshold current density at room temperature (295 K) is as low as 290 A.cm^{-2} for a 1.6 mm-long device emitting at 1.675 eV (740 nm), which is much below values found in the literature. Indeed, reports of InP dot laser threshold found in the literature for emission above 690 nm are so far as follows. Samples grown by Solid Source Molecular Beam Epitaxy (SSMBE) were reported to give threshold current densities of 2.3 kAcm^{-2} [IV.2] for a 2 mm-long device with emission at 728 nm (1.703 eV) and 2.6 kA.cm^{-2} for 1 mm-long devices [IV.3]. InP quantum dot laser grown by MOVPE emitting 718 nm (1.717 eV) was also reported ([IV.1]), with a threshold current density of 4.9 kA.cm^{-2} for 500 μm-long devices.

The measured threshold current also compares quite well with performances obtained from other material systems that can emit in the same wavelength range: tensile-strained GaAsP/AlGaAs QW diode lasers were reported to give a threshold current density of 300 A/cm^2 reported for a 1mm-long device emitting at 735 nm (1.687 eV) [IV.4].

IV.2.3 Value of the peak modal gain

At threshold, the value of the peak net modal gain (G-α_i) can be deduced from the roundtrip amplification condition:

$$G - \alpha_i = \frac{1}{L_c}\ln\left(R^{-1}\right) \qquad \text{(IV.1)}$$

where L_c is the laser cavity length and R is the reflection coefficient at the laser facets. The reflection coefficient is given by:

$$R = \left(\frac{n-1}{n+1}\right)^2 \qquad \text{(IV.2)}$$

where n is the effective index of the waveguide mode, taken as 3.2 from the calculation made in section IV.1.3., which gives a value for R of 0.275.

From (IV.1) and the measured values of threshold current densities, the peak net modal gain is obtained as a function of current density, which is plotted in Figure IV-5 for samples M1b and P3a.

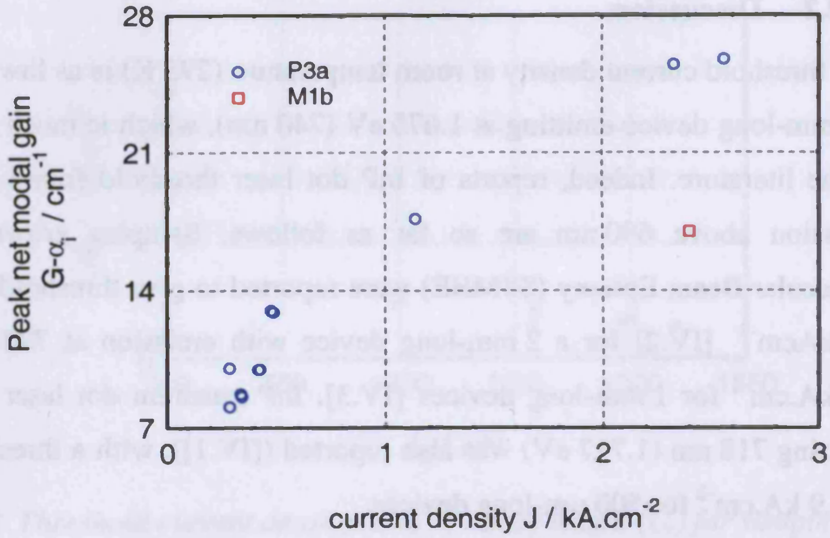

Figure IV-5 Peak net modal gain versus current density from laser threshold measurements from sample P3a and M1b

The next chapters present a study of the absorption and gain properties of the samples that account for the results presented in this chapter.

References

[IV.1] "Lasing from excited states in self-assembled InP/GaInP quantum islands"
J. Porsche, M. Ost, T. Riedl, A. Hangleiter and F. Scholz
Material science and engineering B **74** (2000) pp 263-268

[IV.2] "Room-temperature lasing via ground state of current-injected vertically aligned InP/GaInP quantum dots"
Y.M. Manz, O.G. Schmidt and K.Eberl
Applied Physics Letters – June 5, 2000 – Vol. **76** (23), pp.3343-3345

[IV.3] "Optical and structural anisotropy of InP/GaInP quantum dots for laser applications"
Y.M. Manz, A. Christ, O.G. Schmidt, T. Riedl and A. Hangleiter
Applied Physics Lett. **83** (5) 2003, pp 887-889

[IV.4] "7W CW power from tensile-strained GaAs$_y$P$_{1-y}$/AlGaAs (λ = 735 nm) QW diode lasers"
A. Knauer, G. Erbert, H. Wenzel, A. Bhattacharya, F. Bugge, J. Maege, W. Pittroff and J. Sebatian
Electronics Letters **35** (8) 1999

V. Passive optical absorption

In this chapter, measurements of the passive absorption spectra of samples listed in Table IV-3 are shown and interpreted.

The passive absorption spectrum is a useful quantity to measure in order to understand the performances of the laser structures and to compare the optical properties of different samples. Contrary to gain spectra under excitation, it does not depend on particular pumping conditions so that comparison of the samples is more direct.

First, Atomic Force Microscopy (AFM) measurements performed by JC Lin and AB Krysa on test structures in Sheffield University are described, as they are useful to the interpretation of the absorption spectra presented afterwards.

V.1. AFM

Figure V-1 shows AFM measurements performed on samples made of a single layer of InP dots grown on $Al_{0.3}Ga_{0.7}InP$ without a capping layer, grown on substrates with (211)B and (100) 10° off orientation. The dot layer was formed by deposition of two monolayers (approximately 6 ´) of InP on $Al_{0.3}Ga_{0.7}InP$ at a growth temperature of 650°C, and at a growth rate of 2.5ML/s.

The AFM measurements show that dots have formed on both substrates.

In Figure V-1 *(a)*, measured on the 10° off sample, a clear bimodal distribution of sizes is visible, with large dots appearing to have heights between 15 and 20 nm and a diameter of 40 to 70 nm, and small dots with height of less than 7 nm. Bimodal size distribution was also reported by other groups for InP dots grown on GaInP on (100) substrates ([V.3]) and the same terminology of "type B" for the large dots and "type A" for the small dots is used here. From a count on a surface of 25 μm^2, the type B dots have a density of $2.9 \pm 0.1 \times 10^9 \, cm^{-2}$ and an average height of 16 ± 2 nm with a standard deviation of 1 nm.

The dots in the (211)B sample (Figure V-1 *(b)*) are smaller than the type B dots of the 10°off sample, and seem to be spread over a wide range of heights up to 12 nm.

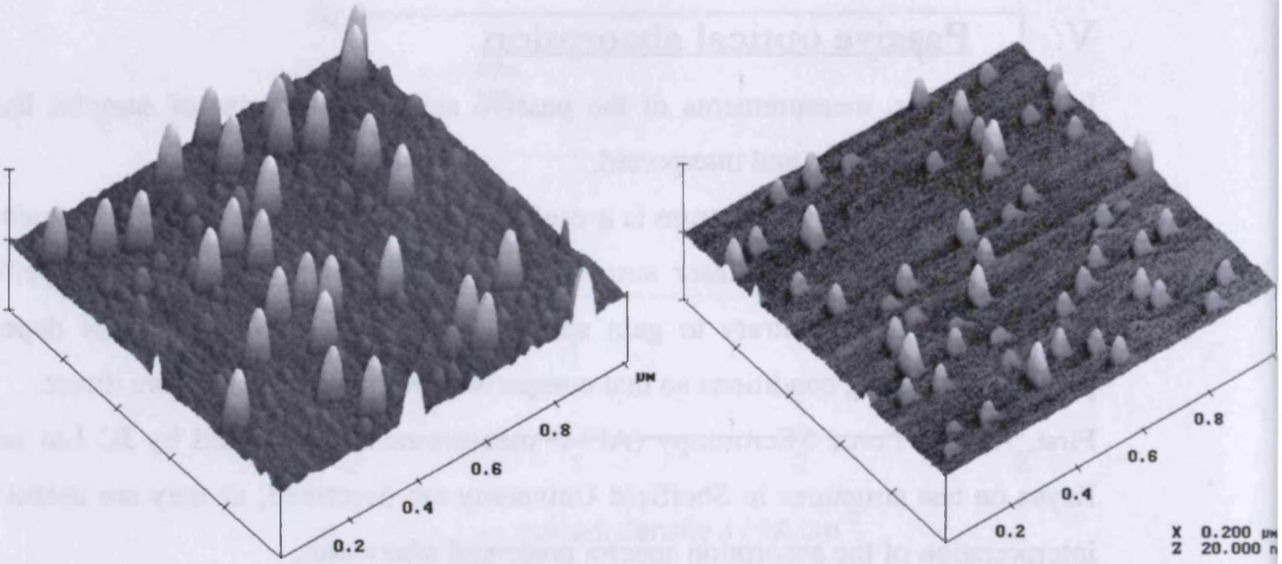

(a) *(b)*

Figure V-1: ***AFM of single layer of dots grown by deposition of two monolayers (2ML) of InP on AlGaInP on 10° off (a) and (211)B substrates (b).***

Samples were also grown for AFM characterisation at a temperature of 690°C with the same InP deposition rate of 2.5 ML/sec, and at a temperature of 650°C with a growth rate of 0.4 ML/sec. Dots are visible on all samples. All the (100) 10°off samples exhibit a clear bimodal distribution of sizes with average heights of the type B dots measured between 14 and 19 nm, while the (211)B samples present smaller dots.

Although the AFM results are useful to show that the dots have formed and do not evaporate, they should be treated with a lot of caution when used to interpret results from heterostructure samples for the following reasons.

In the laser samples, the deposition of the dot material was immediately followed by the deposition of a layer of GaInP. In comparison, the dots in the AFM samples were left uncapped and left to cool down slowly to room temperature. During this cool down period, the species can migrate on the surface, so that changes in not only dot sizes and composition but also density can occur. The growth interruption time was shown to have a large effect on InP dot formation [V.4], with the dots dimensions tending to increase with growth interruption time. Hence, the dots in the laser samples can be expected to be smaller than the AFM suggests.

Besides, the capping of the dots itself can result in changes of dot sizes and composition. Moreover, in the laser samples, the dot layers are stacked, and it is well-known that the strain field and surface morphology induced by the first layer of dots can have strong effects on the growth of the upper dot layers.

V.2. Effect of growth conditions on absorption spectrum

In this section, the room temperature absorption properties of heterostructure samples listed in Table IV-3 are compared. The samples were processed into oxide isolated stripe multisection devices as described in section II.1.2. The stripe width is 50 µm and the sections length is either 300 or 200 µm. The net modal absorption ($\alpha + \alpha_i$) of the unpumped material was measured using the ASE from the first two sections as described in section II.3 using equation (II.8). Its value at low photon energy is a measure of the internal mode loss α_i, and is subtracted to obtain the modal absorption α, which is plotted on all the graphs in this section. In all samples, stronger absorption is obtained from the TE than from the TM polarisation, so that it is the TE absorption spectra that primarily determine the laser properties, and are thus here described and compared in more detail.

V.2.1 Substrate orientation

Figure V-2 shows the modal absorption of heterostructure samples M1a and M1b for light polarised in the plane of the layers (TE). The two samples were grown in the same run respectively on (100) 10° off and (211)B substrates, with the layer structure and growth conditions listed in Table IV-2 and Table IV-3. The growth temperature is 650°C for the central stack of layers, and the deposition rate of the dot material (InP) is 0.8 ML/sec.

The internal modal loss α_i for sample M1a was measured as 11.5 cm^{-1} ± 2 cm^{-1}.
For sample M1b, the value of α_i was estimated around 20 cm^{-1} but the uncertainty on this measurement is large. Due to difficulties in cleaving samples grown on (211)B substrates, the facets are rough, which damages the quality of the nearfield. Good optical alignment was not easy and repeating the measurements on the same or different devices gave different values of α_i with a lot of scatter in the data. However, the measured absorption spectrum α, plotted on Figure V-2, remained unchanged.

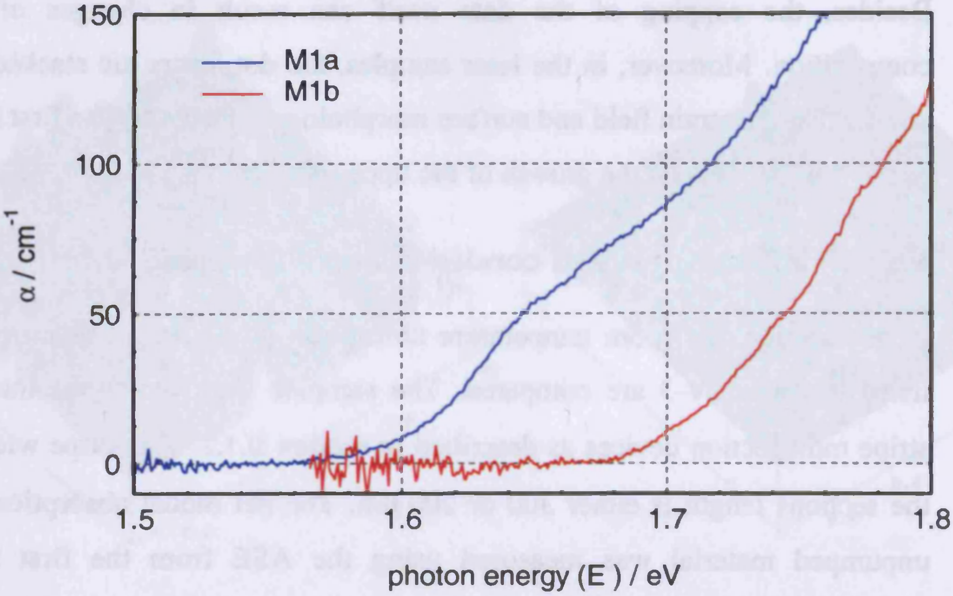

Figure V-2: TE modal absorption of samples M1a and M1b at 300K

The absorption spectra do not exhibit resolved peaks corresponding to different dot transitions, which is probably due to the degree of inhomogeneous broadening, with the absorption spectra from ground states of the quantum dot ensemble overlapping with that from the excited states. Nevertheless the absorption spectrum of sample M1a shows a feature around 1.64 eV, possibly due to absorption by the large dots ground states. Sample M1b exhibits absorption from higher energy than sample M1a, the absorption edges being about 100 meV apart. As the island size decreases, the confinement energy of the carriers increases thus the ground state transition energy increases. Therefore this is consistent with the (211)B sample presenting smaller dots than the larger dots in the 10°off sample, as seen in AFM analysis (section V.1).

V.2.2 Growth rate

Heterostructure samples M1a, M2a and M3a were grown in the same nominal conditions apart from the deposition rate of the InP material, which was 0.8, 1.3 and 2.5ML/sec for the three samples respectively, as shown in Table IV-3. Figure V-3 shows the TE polarised modal absorption spectra of the three samples, measured at 300K. The value of the internal mode loss was measured as 11.5 ± 2 cm^{-1}, 12.5 ± 2 cm^{-1} and 7.5 ± 1 cm^{-1} for samples M1a, M2a and M3a respectively.

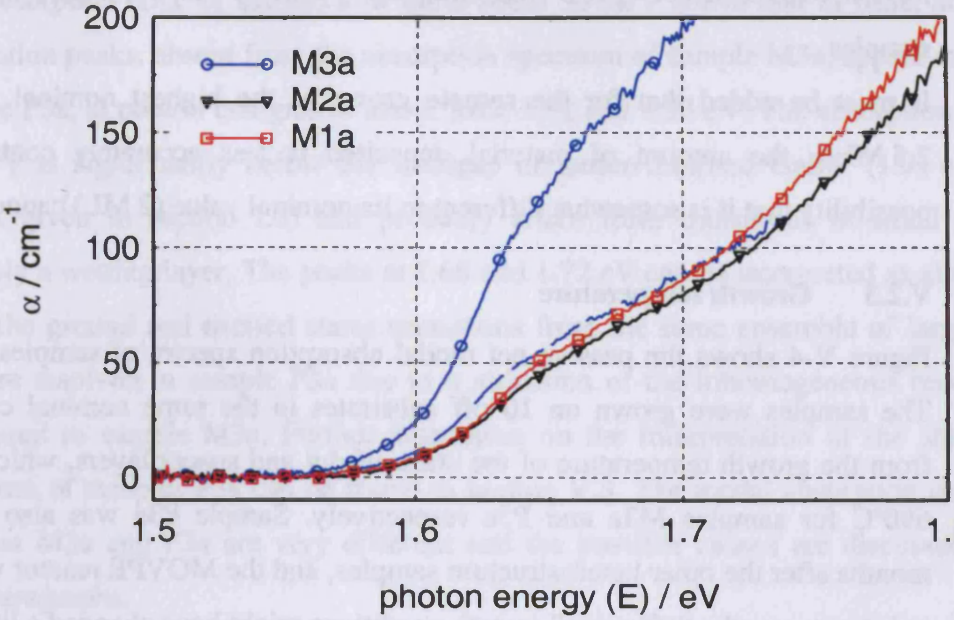

Figure V-3: TE modal absorption spectra of samples M1a, M2a and M3a at 300K

The three absorption spectra show a feature at around 1.64 eV, possibly due to absorption by the large dots ground states.

The absorption spectra of M1a and M2a are similar, showing small influence of the growth rate between these two samples, whereas the absorption from sample M3a is higher over all the measured energy range. The dashed line on Figure V-3 represents the modal absorption spectrum of sample M3a divided by a factor 2.2. It approximately scales to the other spectra, with a small additional red-shift of the order of 10 meV. The scaling of the absorption curves can be due to a difference in dot density, whereas the energy red-shift can be associated with an increase of the dot size or a reduction of the intermixing with the surrounding material. Here it seems that the difference between the absorption of sample M3a and the other two could almost entirely be attributed to an increase of dot density. It is in qualitative agreement with the results obtained from AFM measurements performed on samples with a single layer of uncapped dots, grown at a nominal rate of 2.5 ML/sec (shown in Figure V-1 (*a*)) and 0.4 ML/sec (not shown), that exhibit a bimodal distribution of dot sizes with the large (type B) dots having similar average sizes (measured respectively as 16 and 19 ± 2 nm), with densities of respectively $2.9.10^9$ and $1.9.10^9$ cm^{-2} for the high and low growth rate samples. A quantitative agreement is not expected since the reactants can move for a longer time on the surface for the AFM samples, so that kinetic effects due to the growth rate should have a weaker effect on the final morphology of the AFM samples than of the laser samples.

It must be added that for the sample grown at the highest nominal growth rate of 2.5 ML/s, the amount of material deposited is less accurately controlled and the possibility that it is somewhat different to its nominal value (2 ML) cannot be excluded.

V.2.3 Growth temperature

Figure V-4 shows the passive net modal absorption spectra of samples M3a and P3a. The samples were grown on 10°off substrates in the same nominal conditions apart from the growth temperature of the stack of dot and spacer layers, which is 650ºC and 690ºC for samples M3a and P3a respectively. Sample P3a was also grown several months after the other heterostructure samples, and the MOVPE reactor was refurbished in between, so the "effective" growth conditions might have changed a little.

The internal optical mode α_i was measured at 4 and 7.5 ± 1 cm^{-1} for samples P3a and M3a respectively.

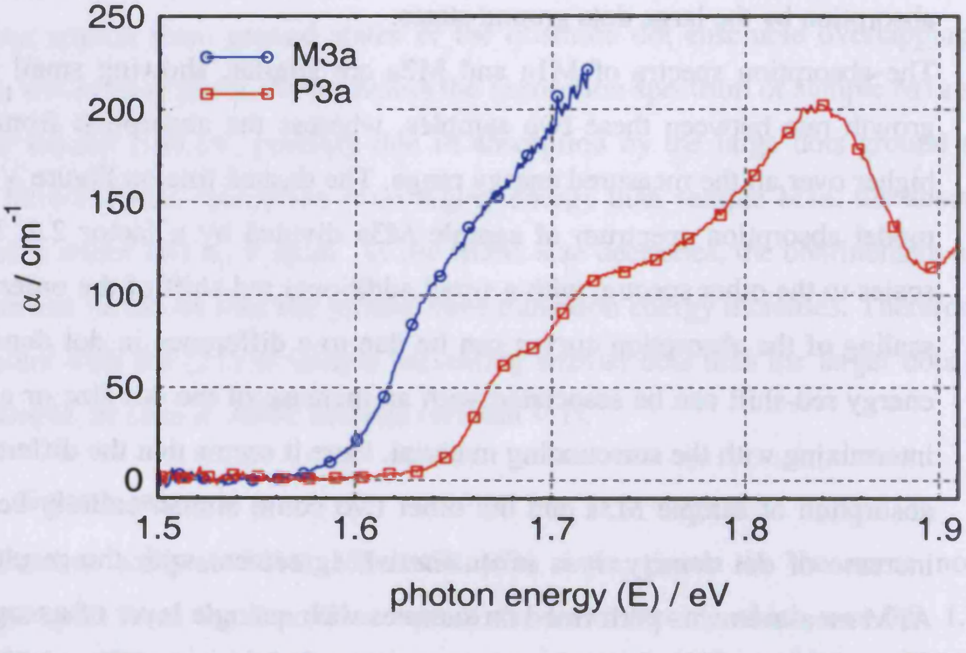

Figure V-4: TE net modal absorption spectra of samples M3a and P3a at 295 K

The absorption edge of sample P3a starts about 50 meV above that of M3a, and clear absorption peaks, absent from the absorption spectrum of sample M3a, appear in that of sample P3a, at photon energies of about 1.68, 1.72 and 1.83 eV. The absorption peak at 1.83 eV is significantly below the bandgap of lattice-matched GaInP (1.91 eV from values given in section I.3) and probably arises from transitions in small dots or possibly a wetting layer. The peaks at 1.68 and 1.72 eV can be interpreted as absorption from the ground and excited states transitions from the same ensemble of larger dots, that are resolved in sample P3a due to a reduction of the inhomogeneous broadening compared to sample M3a. Further discussion on the interpretation of the absorption spectrum of samples P3a can be found in section V.3. The modal absorption spectra of samples M3a and P3a are very different and the possible causes are discussed in the next paragraphs.

The growth temperatures for sample M3a and P3a are respectively 650 and 690°C for the whole stack of dots and spacer layers. It is well documented that a layer of dot can cause strain modulation and undulation on the surface of the overgrown layer, effectively altering the growth conditions for the next layer of dots. It was reported that the growth surface can be flattened by annealing ([V.5]), and this has been used successfully ([V.6]) to improve the interlayer dot uniformity and reduce the formation of dislocations that lead to poor optical quality.

In samples M3a and P3a, a change of growth temperature of the spacer layers from 650 to 690°C may well have changed the surface morphology significantly so that the dots in sample P3a are less affected by the underlying dot layers. This could explain a decrease of inhomogeneous broadening, as well as a blue shift of the absorption due to the absence of very large dots in the upper layers. Additionally, the lower internal optical mode loss of sample P3a compared to sample M3a, respectively measured at 4 and $7.5 \pm 1\ \text{cm}^{-1}$, also hints towards a better surface smoothness. Measurement and comparison of the samples optical efficiency are presented in section VI.2.

The effects of the growth temperature of the self-assembled islands themselves are complex. Increasing the growth temperature accelerates the kinetics of dot formation by increasing the mobility of the reactants on the surface, favours intermixing of the dot material with the surrounding material, which increases the bandgap energy of the dot material causing a blue-shifting the absorption spectrum, and reduces the strain causing a change of dot sizes.

A systematic study of the effects of the temperature and the spacer layer thickness, as well as more structural characterisation on capped structures, would be required to disentangle the possible origins of the large difference observed between the absorption spectra of samples M3a and P3a.

The first transition in the dot being at a higher energy than the bandgap of the dot material, it is possible to put an upper limit to the material intermixing by calculating the effect of intermixing on the bandgap energy. Figure V-5 is a plot of the bandgap energy of $Ga_yIn_{1-y}P$ with varying Gallium composition y calculated as in section (I.3.1.5) and with material parameters given in section (I.3.2). Since partial strain relaxation is expected in the dot material, the two extreme cases of unstrained material and fully strained material (i.e. material under biaxial strain such that its in-plane lattice constant matches that of the GaAs substrate), are represented. It was calculated from the material parameters given in section I. With a ground state transition energies of 1.68 and 1.64eV for samples P3a and M3a respectively, represented on the figure by dashed lines, it is possible to put an upper limit to the fraction of Gallium in the dots at respectively 34% and 30%. Since increasing the aluminium content increases the bandgap, the limit obtained by considering intermixing of the dot material with AlGaInP would be lower. The graph also shows that the energy difference between samples M3a and P3a correspond to a change in gallium content of about 0.04.

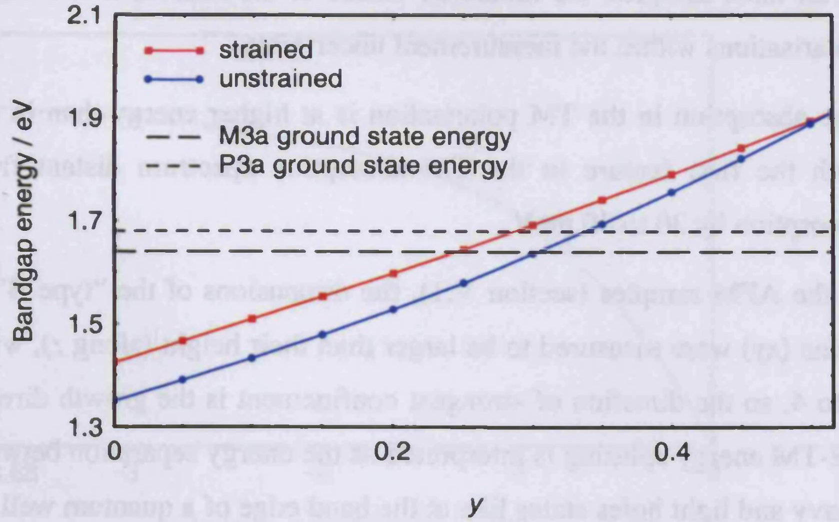

Figure V-5 Variation of the bandgap energy of $Ga_yIn_{1-y}P$ with y, for unstrained material and material under biaxial strain with in-plane lattice parameter matching that of GaAs.

V.2.4 TE and TM absorption spectra

Figure V-6 regroups both TE (plain lines) and TM (dashed lines) net modal absorption spectra of samples M1a, M3a and P3a.

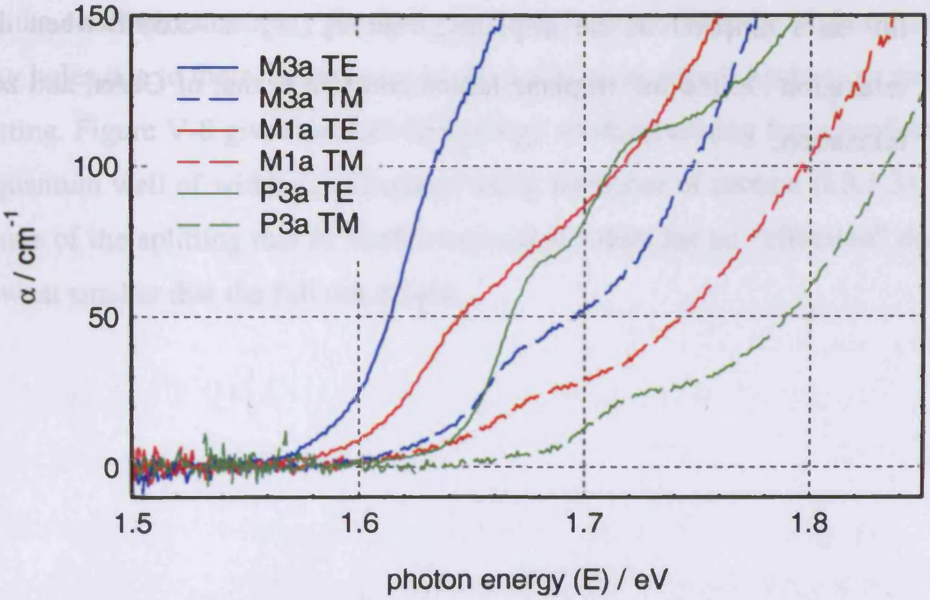

Figure V-6 TE and TM net modal absorption of samples M1a, M3a and P3

In all three samples, the measured values of the internal mode loss are equal for both polarisations within the measurement uncertainty.

The absorption in the TM polarisation is at higher energy than in the TE polarisation, with the first feature in the TM absorption spectrum distant from that in the TE absorption by 30 to 40 meV.

In the AFM samples (section V.1), the dimensions of the "type B" dots in the growth plane (*xy*) were measured to be larger than their height (along *z*), with a ratio of at least 3 to 4, so the direction of strongest confinement is the growth direction. Therefore the TE-TM energy splitting is interpreted as the energy separation between the lowest lying heavy and light holes states like at the band edge of a quantum well. This is because the heavy holes interact only with the TE polarisation at the band edge (see section I.5.4), whereas the light holes interact mostly with the TM polarisation.

To determine if the measured splitting of 30 to 40 meV between TE and TM polarisation is in the expected energy range for the splitting between heavy holes (HH) and light hole (LH) states, the LH-HH energy splitting ($E_{v,hh}$-$E_{v,lh}$) in the InP dot material under in-plane biaxial compressive strain was estimated as in section (I.3.1.5). Figure V-7 represents the difference between the HH and LH energy band positions for InP as a function of the in-plane strain $\varepsilon_{//}$. $\varepsilon_{//}$ is -3.68% when there is no strain relaxation i.e. the InP in-plane lattice constant is that of GaAs, and zero for full strain relaxation.

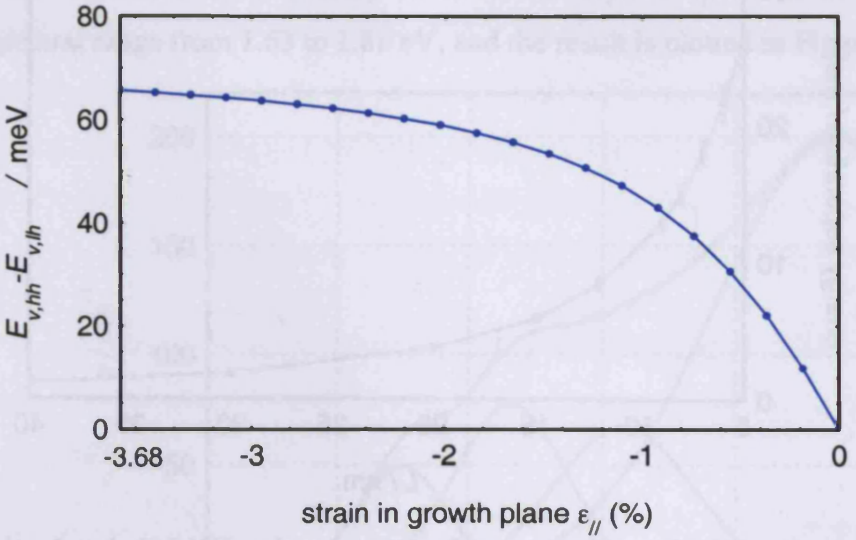

Figure V-7 HH-LH band edge energy splitting of InP as a function of in-plane strain $\varepsilon_{//} = 0$ *correspond to unstrained material and* $\varepsilon_{//} = -3.68\%$ *to in-plane lattice-matching with GaAs.*

The predicted HH-LH energy splitting for InP due to compressive strain varies from 65 meV to 0 when the lattice is relaxed to its native value, hence a measured splitting of 30 to 40 meV lies roughly in the expected energy range. Intermixing with the surrounding GaInP would decrease the calculated energy splitting.

Besides, the confinement energy for the light holes is expected to be higher than that of the heavy holes due to their lighter mass in the z-direction, which leads to an increase of this splitting. Figure V-8 gives the LH-HH energy splitting arising from confinement in an InP quantum well of width L, calculated using formulae of section (I.3.1.3). It gives an estimate of the splitting due to confinement in the dots for an "effective" dot height L, somewhat smaller that the full dot height.

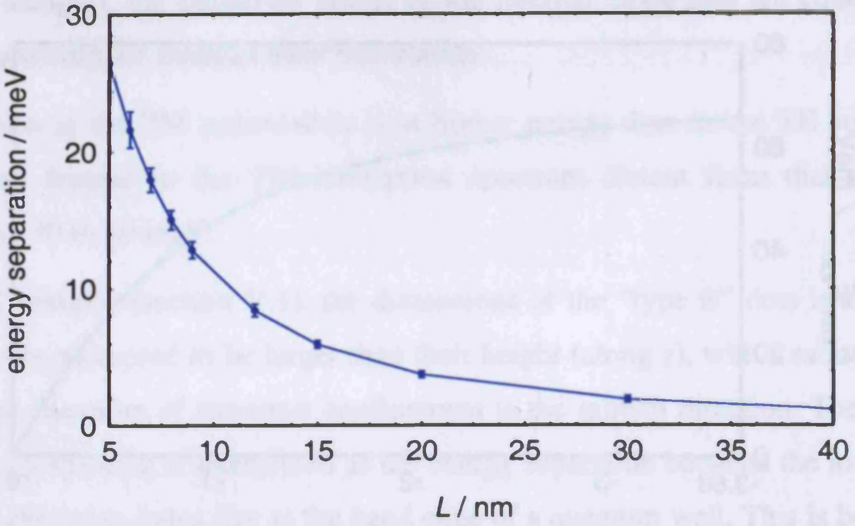

Figure V-8 *Contribution of the confinement to the HH-LH band edge energy separation in an InP well of width L. The error bars take into account the cases where the well is surrounded by GaInP or $Al_{0.3}Ga_{0.7}InP$ lattice-matched to GaAs, and if the strain in the InP well is relaxed or not.*

For example, for an effective width of 10 nm, the expected LH-HH splitting due to confinement alone is about 12 meV, which is less than the measured LH-HH splitting.

V.3. Discussion on the absorption spectrum of P3a

V.3.1 Dot density

In section V.2.3, the two lowest energy peaks in the absorption spectrum of sample P3a, at around 1.68 and 1.72 eV, were rapidly attributed to the ground and first excited states of the larger dots.

In this assumption, a simple representation of the dot transition pairs with unity envelope function overlap, is used to get an estimate of the dot density.

Contribution of the ground and excited states transitions to the total absorption spectrum

To isolate the contribution of each group of transitions to the total absorption spectrum, it is fitted by a sum of Gaussian functions that have the form of (V.1):

$$y = \frac{I}{\sigma\sqrt{2\pi}} \exp\left(\frac{-(x-m)^2}{2\sigma^2} \right) \qquad \text{(V.1)}$$

Four Gaussians are necessary to fit the absorption spectrum of sample P3a on the spectral range from 1.63 to 1.88 eV, and the result is plotted in Figure V-9.

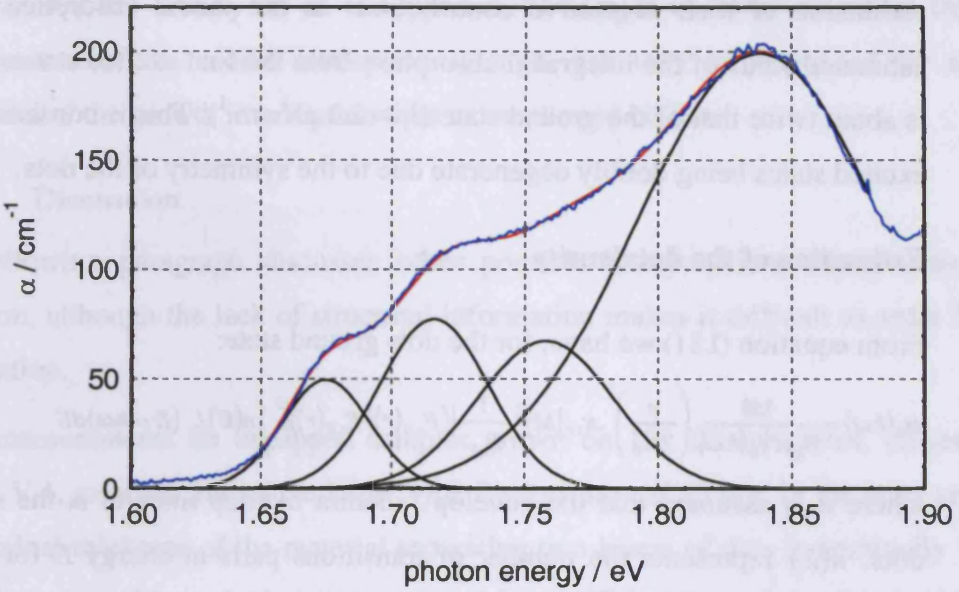

Figure V-9 TE modal absorption spectrum of sample P3a with Gaussian fittings

The best fit is plotted in red, and the four corresponding Gaussians in black.

The four Gaussian spectra are denoted by α_j ($j = 0 .. 3$), numbered from 0 to 3 with increasing average photon energy. The values of the fitting parameters are listed in Table V-1

	m (eV)	I (eV.cm^{-1})	σ (meV)
α_0	1.675	2.08	17
α_1	1.716	4.03	21
α_2	1.758	4.34	26
α_3	1.838	23.2	47

Table V-1 Value of the fitting parameters

In the assumption that the first two peaks in the absorption spectrum are due to ground and first excited states transitions, the spectra $\alpha_1(\hbar\omega)$ and $\alpha_2(\hbar\omega)$ represent an estimation of their respective contributions to the modal absorption spectrum. The estimated value of the integrated absorption from the first excited states ($I_1 \approx 4$ eV.cm^{-1}) is about twice that of the ground state ($I_1 \approx 2.1$ eV.cm^{-1}). This is consistent with the first excited states being doubly degenerate due to the symmetry of the dots.

Estimation of the dot density

From equation (I.81) we have, for the dots ground state:

$$\alpha_0(\hbar\omega)=\frac{4\pi\hbar}{n_{eff}c\varepsilon_0(\hbar\omega)}\left(\frac{e}{2m_0}\right)^2.\kappa_{TE}|M|^2.\frac{1}{L_{eff}}\left|\langle F_{c,0}(r)|F_{v,0}(r)\rangle\right|^2\int_E n(E).L\,(E-\hbar\omega)dE \qquad \text{(V.2)}$$

where it is assumed that the envelop function overlap integral is the same for all the dots. $n(E)$ represents the number of transitions pairs at energy E for the dot ground states per unit area and unit energy.

If one dot contributes to two transitions for the ground state, integrating over transition energy gives:

$$\int\alpha_0(\hbar\omega)d\hbar\omega = I_0 = \frac{4\pi\hbar}{n_{eff}c\varepsilon_0(\hbar\omega)}\left(\frac{e}{2m_0}\right)^2.\kappa_{TE}|M|^2.\frac{1}{L_{eff}}\left|\langle F_{c,0}(r)|F_{v,0}(r)\rangle\right|^2 2.N \qquad \text{(V.3)}$$

where N is the dot density.

Rearranging equation (V.3) gives:

$$N = I_0.\frac{n_{eff}c\varepsilon_0(\hbar\omega).L_{eff}}{8\pi\hbar}\left(\frac{2m_0}{e}\right)^2.\frac{1}{\kappa_{TE}|M|^2}.\frac{1}{\left|\langle F_{c,0}(r)|F_{v,0}(r)\rangle\right|^2} \qquad \text{(V.4)}$$

with $I_0 = 2.08$ eV.cm^{-1} from the previous estimation.

Assuming that the lowest lying transition involves only heavy holes and that the polarisation coefficient is $\kappa_{TE} = 0.5$ as for a quantum well in the (xy) plane, and assuming unity envelope function overlap, an estimate of the dot density can be obtained from (V.4). The waveguide parameters (n_{eff}, L_{eff}) have been calculated in section (IV.1.3). Using the momentum matrix element M of bulk InP given in section I.3.2.8) (intermixing with the surrounding GaInP could increase this value by up to 25%), equation (V.4) gives:

$N = 1.35.10^{11}$ cm^{-2}, i.e. $2.7.10^{10}$ cm^{-2} per layer.

This dot density is almost an order of magnitude higher than what was obtained from the AFM measurements ($3.10^9.cm^{-2}$) on an uncapped sample. The discrepancy between the measured dot density on an uncapped AFM sample and that estimated from the measurement of the modal absorption is high, but may be explained by a large difference of the growth interruption time as mentioned before.

V.3.2 Discussion

The following paragraph discusses other possible interpretations of the absorption spectrum, although the lack of structural information makes it difficult to settle for one explanation.

AFM measurements on uncapped samples grown on 10° off substrates, presented in section V.1, gave heights of the large (type B) dots around 15 nm. In the laser samples, the nominal thickness of the material separating two layers of dots is nominally 16 nm, which is comparable to dot heights measured from AFM. Although the dots in the AFM samples are likely to be larger because the material has more time to gather into the dots than in the laser samples where the dots are capped immediately after deposition, it is possible that the confined electronic states in different layers are coupled. More investigation on samples with different spacer layer thickness or different number of layers would be required to determine if this is the case and what effects this has on the optical properties of the samples.

In that respect, it is interesting to note that in reference ([V.3]), the authors reported measurements on a sample made of a single layer of dots of InP grown in GaInP that exhibits emission peaks at energies very similar to that of sample P3a (1.68, 1.73, 1.77 and 1.83 eV), and where the first peaks were quickly attributed to ground and first excited states emission. Cross-section TEM images presented in the paper give an estimate of the dot height of about 7 nm. Although the sample in this reference was grown in GaInP, on 15°off substrate and with different growth conditions, the similarity of the optical transition spectrum suggests that the dots in sample P3a are similar, and that the AFM measurements on uncapped samples presented here strongly overestimate the dot heights. It also suggests that the apparition of the peaks in the absorption spectrum is not an effect of the stacking and coupling of the dots.

An alternative to the interpretation of the peaks in the absorption spectrum of sample P3a as ground and first excited states is that they arise from non-consecutive excited states, with for example the peaks arising from different states due to *z*-confinement, each involving several states with different wavefunctions in the (*xy*) plane where the dimensions of the dots are larger. Thorough modelling of the dot states position would require more structural information, and is out of the scope of this thesis. However, the energy separation between the first and second e-HH transitions with different wavefunctions in the *z*-direction can be estimated using a calculation for a quantum well of effective width *L*.

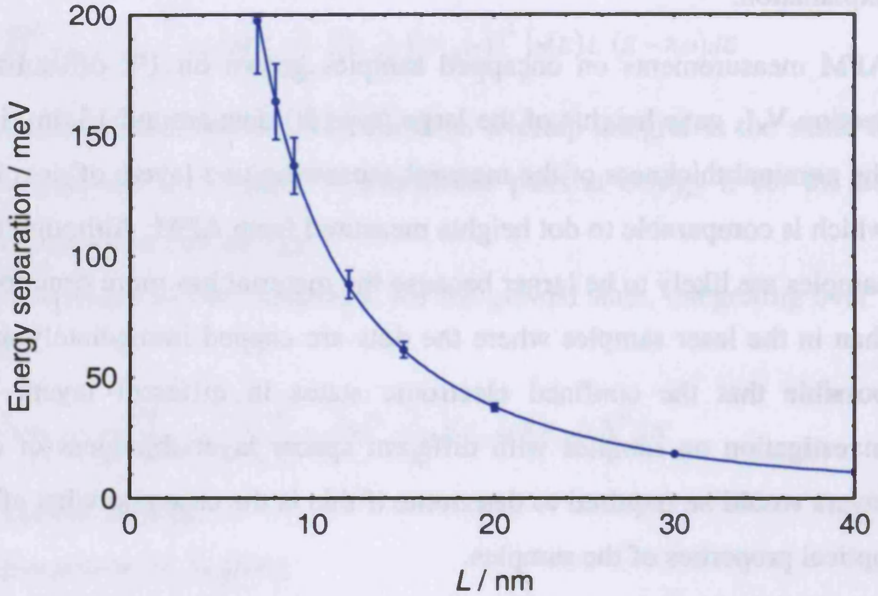

Figure V-10 ***Energy separation between first and second subband transition energies for transitions between conduction and HH bands, in an InP quantum well, as a function of the well width L. The error bars take into account the cases where the InP well is surrounded by GaInP or $Al_{0.3}Ga_{0.7}InP$ lattice-matched to GaAs, and if the strain in the InP well is relaxed or not. The dashed line is the measured TE-TM separation.***

Referring to Figure V-10, the estimated effective height of a dot giving a separation of 40 meV would be about 20 nm, which seems too high, showing that this last interpretation of the peaks in the absorption is rather unlikely. The value of 20 nm is probably nearer to the effective width in the (*xy*) plane, which rather supports the interpretation in terms of ground and first excited states in the dots.

Finally, the energy of the second peak in the absorption spectrum for TE polarisation corresponding to the energy of the first peak in the TM absorption indicates that the two peaks in the TE absorption of P3a could be due to transitions involving heavy and light holes, although the peak in the TE spectrum would be expected to be about 2/3 weaker than in the TM spectrum whereas examining the absorption spectra shows that the peak is rather more pronounced.

V.4. Temperature dependence

Figure V-11 and Figure V-12 show the evolution of the modal absorption spectra of samples P3a and M3a with temperature.

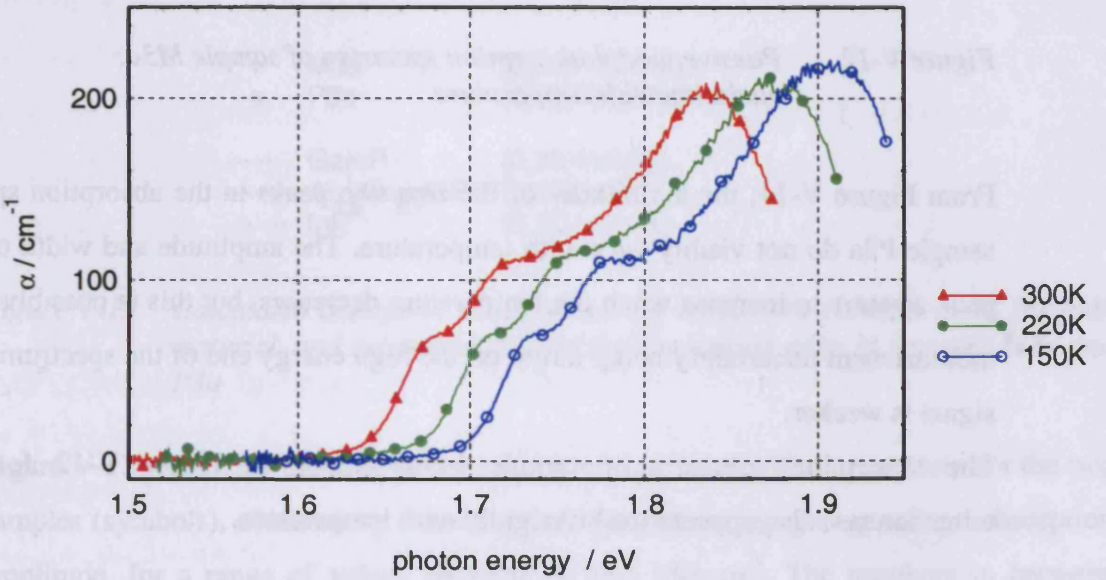

Figure V-11 Passive modal absorption spectrum of sample P3a: variation with temperature

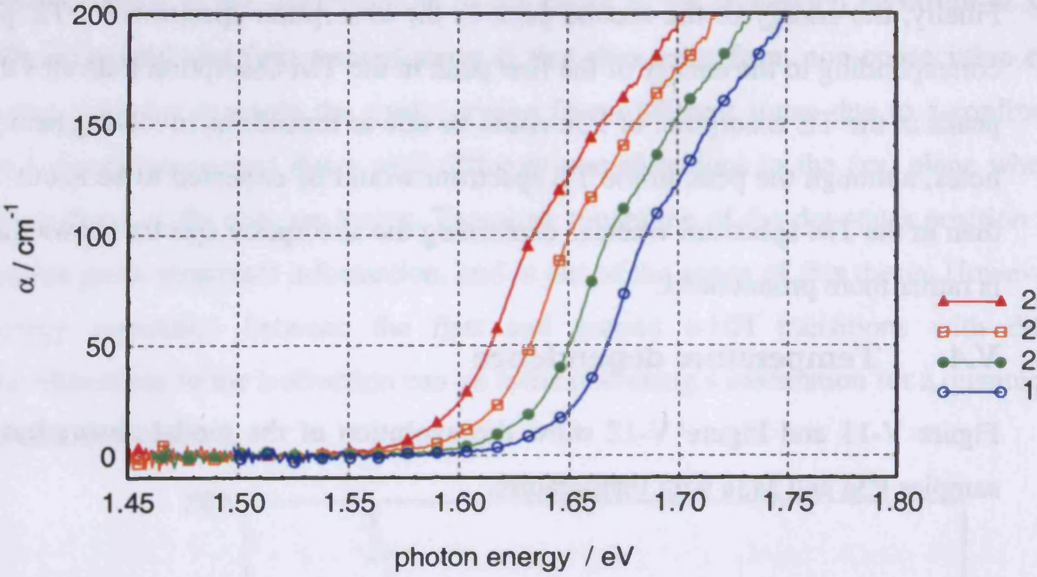

Figure V-12 *Passive modal absorption spectrum of sample M3a: variation with temperature*

From Figure V-11, the amplitudes of the first two peaks in the absorption spectrum of sample P3a do not visibly vary with temperature. The amplitude and width of the third peak appears to increase when the temperature decreases, but this is possibly due to the measurement uncertainty being larger on the high energy end of the spectrum where the signal is weaker.

The absorption spectrum of sample M3a, plotted in Figure V-12 for different temperatures, also appears to shift rigidly with temperature.

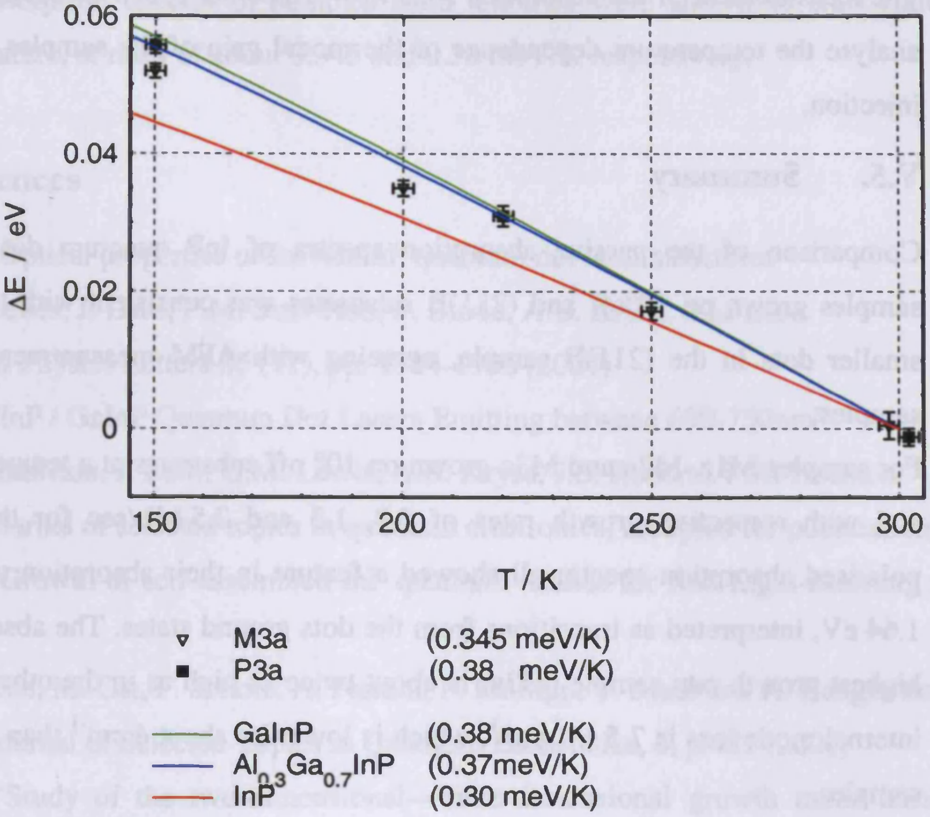

Figure V-13 Calculated change in bandgap energy relative to value at 300K for bulk material, and measured shift of the absorption edge in samples M3a and P3a

Figure V-13 represents the shift of the absorption spectrum with temperature for the two samples (symbols), obtained by measuring the photon energy giving a fixed absorption amplitude, for a range of values between 20 and 150 cm^{-1}. The numbers in between brackets in the legend are the average shifting rates obtained from a linear fit.

The variation of the direct bandgap with temperature of bulk InP, GaInP and AlGaInP, with temperature, obtained from (I.29), (I.32) and (I.35), is also represented on Figure V-13. As might be expected, the shift of the absorption spectrum of the samples lies roughly in between that of the bandgap of InP, which is the nominal composition of the islands, and GaInP and AlGaInP which make up the surrounding material. It would not be appropriate to draw conclusions on the nature of the islands from a quantitative analysis of these results; however larger temperature dependence for sample P3a compared to M3a might indicate a larger degree of intermixing of the InP dots with the surrounding GaInP and AlGaInP material.

The measurement of the absorption shift with temperature will be used in chapter VI to analyse the temperature dependence of the modal gain of the samples under electrical injection.

V.5. Summary

Comparison of the passive absorption spectra of InP quantum dot heterostructure samples grown on 10°off and (211)B substrates was consistent with the formation of smaller dots in the (211)B sample, agreeing with AFM measurements on uncapped samples.

For samples M1a, M2a and M3a grown on 10° off substrates at a temperature of 650°C and with respective growth rates of 0.8, 1.3 and 2.5 ML/sec for the dots, the TE polarised absorption spectra all showed a feature in their absorption spectrum around 1.64 eV, interpreted as transitions from the dots ground states. The absorption from the highest growth rate sample (M3a) is about twice as high as in the other two, while the internal mode loss is 7.5 ± 1 cm^{-1}, which is lower by about 4 cm^{-1} than in the other two samples.

Sample P3a, grown on 10°off substrate at a higher temperature of 690°C and at a nominal growth rate of 2.5 ML/sec for the dots like in sample M3a, presents a very different TE absorption spectrum to M3a, both in terms of transition energy and shape, unforeseen by AFM analysis. The internal mode loss is also lower at 4 ± 1 cm^{-1}. The large difference may be caused by a better surface smoothness in sample P3a due to a higher growth temperature of the spacer layers.

All the samples grown on 10°off substrates exhibit TM absorption from about 30 to 40meV above the TE polarisation, due to added effects of residual strain in the dots and confinement potential, causing a splitting of the heavy and light hole first levels.

The TE absorption spectrum of P3a presents resolved peaks at 1.68, 1.73 eV, interpreted respectively as transitions from ground states and first excited states from the same ensemble of dots, and a peak at 1.84 eV from either small dots, a wetting layer or a mix of both. Within this interpretation, the dot density was estimated at about $2.7.10^{10}$ cm^{-2} per layer of dots, which is about an order of magnitude higher than the value given by AFM measurements on uncapped samples. However it was shown that other interpretations of the absorption spectrum are possible, that can not be discarded due to lack of accurate structural information.

The absorption spectra of samples M3a and P3a were shown to shift rigidly with temperature, at rates of about 0.345 and 0.38 meV/K respectively.

References

[V.1] "Optical properties of InP/GaInP quantum dot laser structures"
G.M. Lewis, J. Lutti, P.M. Smowton, P. Blood, A.B. Krysa, S.L. Liew
Applied Physics Letters **85** (11), pp. 1904-1906 (2004)
[V.2] "InP / GaInP Quantum Dot Lasers Emitting between 690-750nm"
P.M. Smowton, J. Lutti, G.M. Lewis, A.B. Krysa, J.S. Roberts, P.A. Houston
IEEE journal of selected topics in quantum electronics, accepted for publication
[V.3] "Growth of self-assembled InP quantum islands for Red-Light-Emitting injection lasers"
J. Porsche, M. Ost, F. Scholz, A. Fantini, F. Phillipp, T. Riedl and A. Hangleiter
IEEE Journal of Selected Topics in Quantum Electronics, **6**, p.482 (2000)
[V.4] "Study of the two-dimensional—three-dimensional growth mode transition in metalorganic vapor phase epitaxy of GaInP/InP quantum-sized structures"
N. Carlsson, W. Seifert, A. Petersson, P. Castrillo, M.E. Pistol and L. Samuelson
Applied Physics Letters **65** (24) 1994, pp. 3093-3095
[V.5] "Strain and electronic interactions in InAs/GaAs quantum dot multilayers for 1300 nm emission"
E.C. Le Ru, A.J Bennett, C. Roberts and R. Murray
Journal of Applied Physics **91** (2002), pp.1365-1370
[V.6] "Improved performance of 1.3 μm multilayer InAs quantum-dot lasers using high-growth-temperature GaAs spacer layer"
H.Y Liu, I.R. Sellers, T.J. Badcock, D.J. Mowbray, M.S. Skolnick, K.M. Groom, M. Gutierrez, M. Hopkinson, J.S. Ng, J.P.R. David and R. Beanland
Applied Physics Letters **85** (2004) pp.704-706

VI. Optical gain and emission under excitation

In this chapter, gain and emission properties of the heterostructure samples under electrical injection are presented. The first section provides a comparison of the modal gain spectra at room temperature, with a comparison to the laser results that were presented in chapter IV. Measurements of radiative efficiency are presented in the second section. The chapter ends with a study of the gain properties of the samples as a function of temperature, which shows a temperature dependent saturation of the modal gain at a level below the limit of full population inversion.

VI.1. Gain spectra at room temperature

VI.1.1 Gain spectra for 10°off samples, evolution with growth rate

Figure VI-1 shows the TE net modal gain spectra $(G-\alpha_i)$ of samples M1a, M2a and M3a under electrical injection (plain lines with symbols).

At low photon energy, the spectra converge towards $(-\alpha_i)$, α_i being the internal mode loss.

Hardly any positive modal gain G is obtained from samples M1a and M2a, with no positive gain at all obtained from sample M1a at current densities up to 3.3 kA / cm^2. The highest gain is obtained from sample M3a, with broad positive modal gain G achieved between 1.55 and 1.71 eV at a current density of 3.33 kA/cm^2. The useful gain $(G-\alpha_i)$ reaches positive value of 4.5 ± 1 cm^{-1}, which implies that it is possible to obtain lasing action from this device at room temperature. However the required current density is high and the required cavity length is long (2.9 mm for a maximum net modal gain of 4.5 cm^{-1} for a device with uncoated facets).

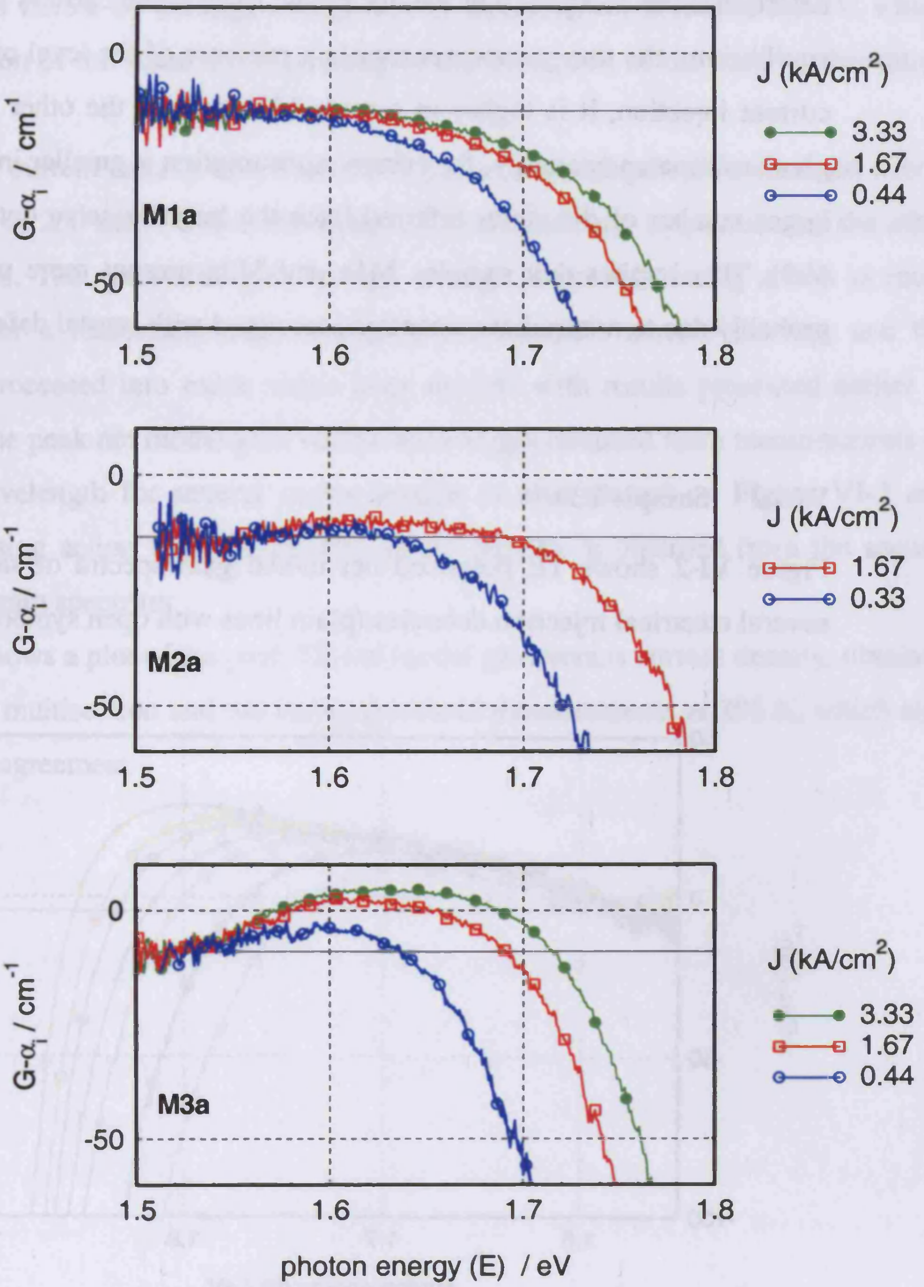

Figure VI-1: TE net modal gain spectra at 300K of devices M1a, M2a and M3a under electrical injection J.
The scattering loss level ($-\alpha_i$) is represented by a plain horizontal line.

Assuming that the carriers in the samples are in quasi-thermal equilibrium, the transparency energy, which is obtained where the gain spectrum crosses the level of the internal losses, gives the quasi-Fermi level separation (see section II.3.1.4)), which determines the occupancy of the dot states. Even if the carriers are not in quasi thermal equilibrium, the transparency energy is a measure of the level of pumping. For a given current injection, it is higher in sample M3a than in the other two samples, i.e. for a given transparency energy, the current consumption is smaller in sample M3a, despite a larger number of dot states inferred from the larger passive optical absorption (Figure V-3). This implies that samples M1a and M2a present more parasitic recombination, probably due to non-radiative centres associated with crystal defects.

VI.1.2 Sample P3a

Figure VI-2 shows TE polarised net modal gain spectra of sample P3a at 295K for several electrical injection densities (plain lines with open symbols).

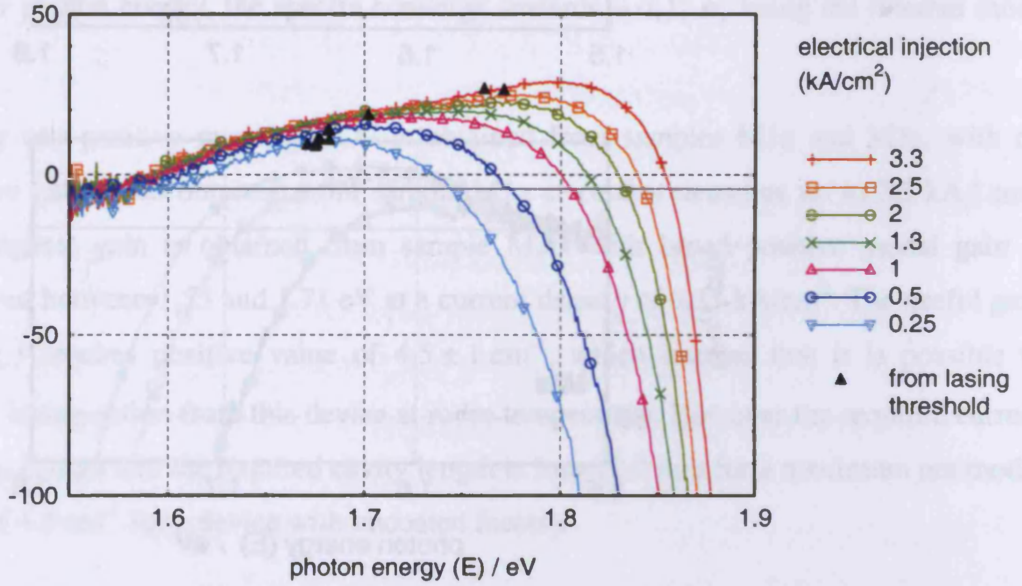

Figure VI-2: TE net modal gain of sample P3a under electrical injection at 295K measured using the multisection technique (plain lines with open symbols) and deduced from laser threshold measurement (full black triangles).

The peaks observed in the passive absorption spectrum of sample P3a (Figure V-4) around 1.68 and 1.72 eV are not visible in the gain spectra under electrical excitation, presumably due to an increase in homogeneous broadening with carrier density. A second peak is visible on the high energy side of the spectrum at around 1.8 eV, which is a contribution of the states corresponding to the third peak of the passive absorption spectrum.

At the highest current density of 3.3 $kA.cm^{-2}$, positive modal gain G is obtained over a spectral width of 250 meV, with a maximum of 33 cm^{-1}, clearly outperforming the other 10°off samples. The net modal gain is high enough to provide lasing action at room temperature for a reasonably short device and reasonable current density, and the sample was processed into oxide stripe laser devices with results presented earlier in chapter IV. The peak net modal gain versus wavelength deduced from measurements of the lasing wavelength for several cavity lengths is also plotted on Figure VI-2 and shows that lasing action from the shorter cavity lengths is obtained from the second feature in the gain spectrum.

Figure VI-3 shows a plot of the peak TE net modal gain versus current density, obtained from both the multisection and the lasing threshold measurements at 295 K, which also shows a good agreement.

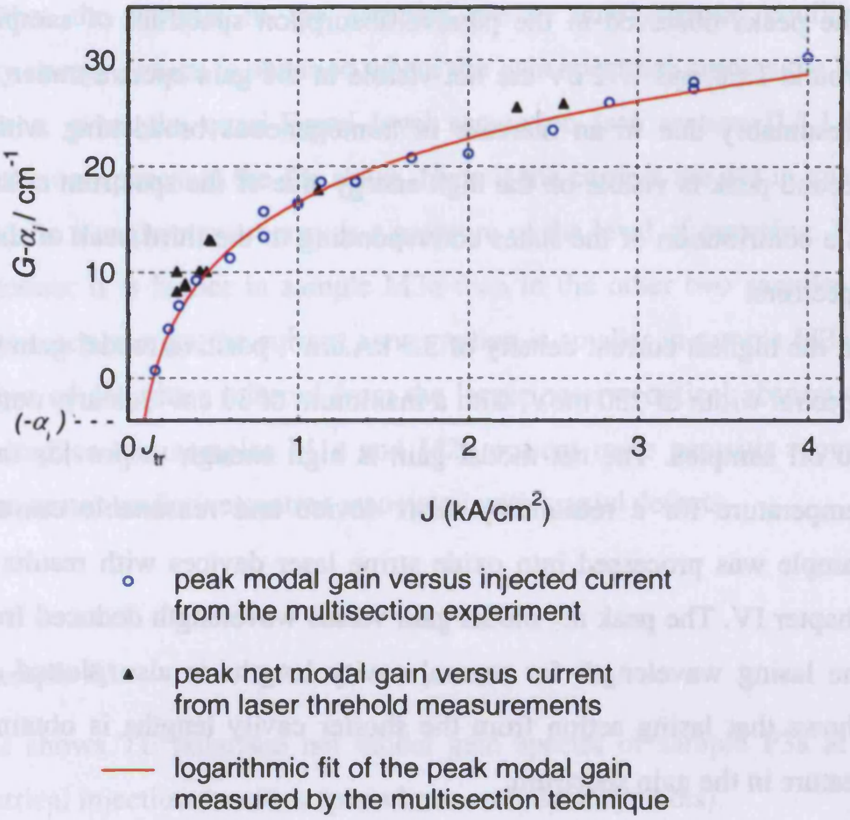

Figure VI-3: Net modal gain versus injected current density for sample P3a at 295K

The usual logarithmic fit of the peak modal gain measured by the multisection technique by $G = G_0.\ln\frac{J}{J_{tr}}$, gives a transparency current density of $J_{tr} = 100 A.cm^{-2}$, and $G_0 = 20\,cm^{-1}$. The fit is also plotted in the figure (plain line)

VI.1.3 Sample M1b

TE polarised net modal gain spectra of sample M1b, grown on (211)B substrate, are plotted in Figure VI-4.

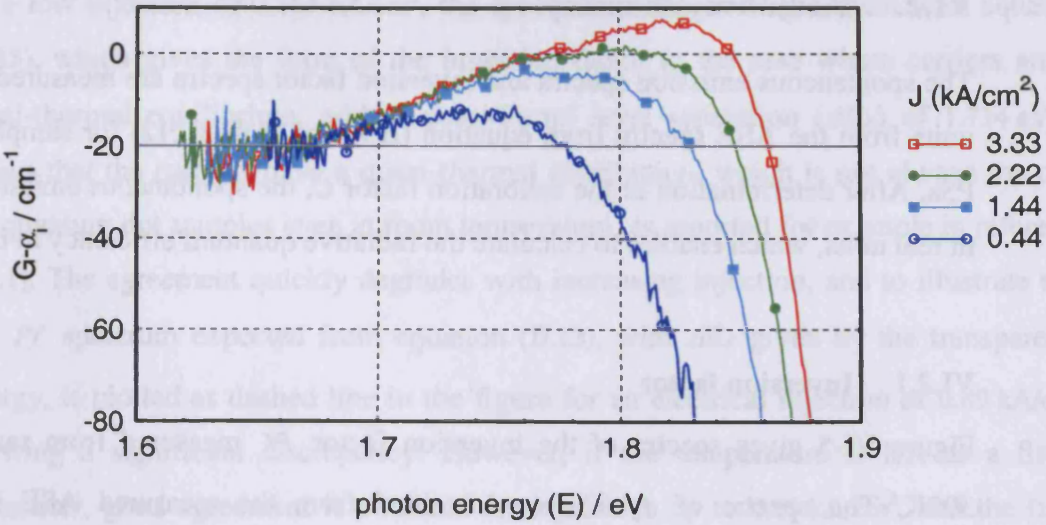

Figure VI-4 *TE net modal gain spectra of sample M1b under electrical injection, measured at 300 K*

The modal gain *G* achieved with this sample is higher than with any of the 10°off samples grown at the same temperature, and reaches a maximum value of 25 cm^{-1} at the maximum current injection of 3.3 kA.cm^{-2}.

It was reported in chapter IV.2, that a 750 µm-long device from this sample produces a lasing wavelength of 688 nm (1.802 eV), with a threshold current density of 2.4 kA.cm^{-2}. From the measured gain spectrum at a similar current density of 2.2 kA.cm^{-2}, the peak net modal gain is also at photon energy of about 1.80 eV, as one may expect. However, its value is only about 2 cm^{-1}, whereas a value of about 17 cm^{-1} is obtained from the round-trip amplification condition. This is because as mentioned in section V.2.1, the measured value of the internal loss is very inaccurate in that sample so that the net modal gain is shifted down compared to its real value. The threshold current measurement suggests an actual internal mode loss of about 5 cm^{-1}.

VI.2. Radiative efficiency

The spontaneous emission spectra and inversion factor spectra are measured in arbitrary units from the ASE spectra from equation (II.9) and from (II.12) for samples M3a and P3a. After determination of the calibration factor C, the spontaneous emission is known in real units, which enables to calculate the radiative quantum efficiency in the samples.

VI.2.1 Inversion factor

Figure VI-5 gives spectra of the inversion factor Pf measured from sample P3a at 302K. The spectra of Pf/C were obtained from the measured ASE by applying equation (II.12) for different current injections and in otherwise the same conditions. The measured spectra of Pf/C converge on the low energy end of the spectrum towards a common value, identified as corresponding to $Pf = 1$, which enables to determine the calibration factor C. The value of C thus determined was used to plot the spectrum of Pf in real units in Figure VI-5.

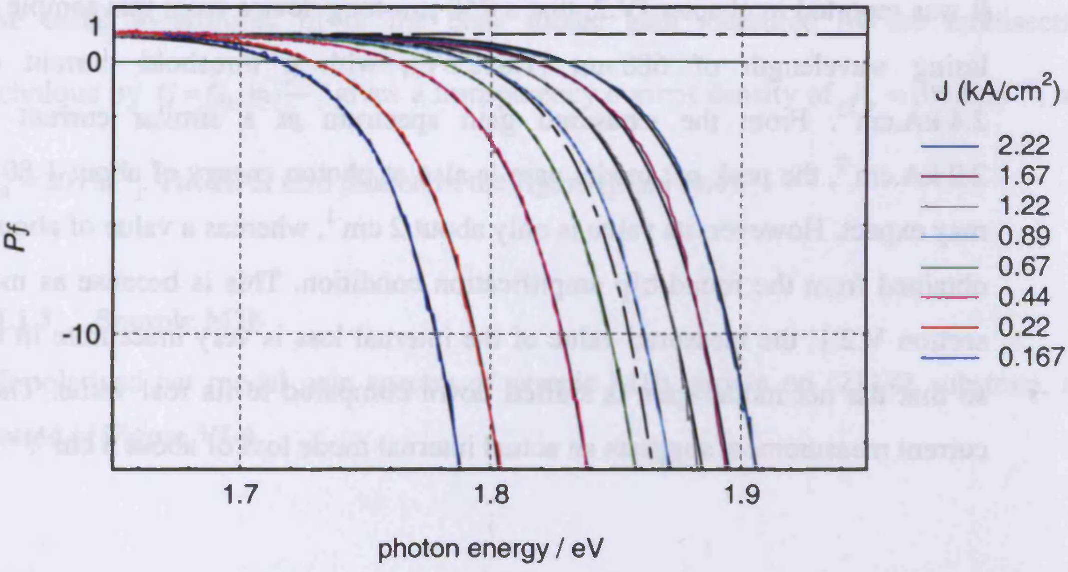

Figure VI-5 Inversion factor Pf for sample P3a, at 302K

At a low injection of 0.167 kA/cm^2, the spectrum is in good agreement with equation (II.13), which gives the form of the inversion factor in the case where carriers are in quasi-thermal equilibrium, with a quasi-Fermi level separation (ΔE_F) of 1.714 eV. It shows that the carriers have a quasi-thermal distribution, which is not always the case for quantum dot samples even at room temperature, as reported for example in reference [VI.1]. The agreement quickly degrades with increasing injection, and to illustrate this, the Pf spectrum expected from equation (II.13), with ΔE_F given by the transparency energy, is plotted as dashed line in the figure for an electrical injection of 0.89 kA/cm^2, showing a significant discrepancy. However, if the temperature is left as a fitting parameter, good agreement is obtained for injections up to 0.89 kA/cm^2, and the fitted temperature increases with injection. Best fits to equation (II.13) are plotted as black plain lines in Figure VI-5, and the fitted values of the quasi-Fermi level separation and temperature are reported in Table VI-1. Above 0.89 kA/cm^2, the quality of the fitting deteriorates even when the temperature is left as a free parameter, with the value of the measured inversion lower than that given by the fitted curves below the transparency energy.

J (kA/cm^2)	0.167	0.22	0.44	0.67	0.89	1.22	1.67	2.22
T (K)	305	312	319	329	330	336	323	321
ΔE_F (eV)	1.715	1.729	1.762	1.779	1.793	1.804	1.818	1.830

Table VI-1 Fitted values of the Fermi-level separation and temperature

The fitted temperature increasing with injection could be a sign of lattice heating; however, it was checked that the fitted temperature does not change if the duty cycle is reduced or increased by a factor five, nor if the measurements are taken while gating the ASE on shorter time windows along the pulse. Therefore the increase of the fitted temperature with current injection is probably not due to an increase of the lattice temperature. It is shown in the appendix of this chapter that an apparent increase of the temperature can arise from homogeneous broadening, which was neglected to obtain expression (II.13). Homogeneous broadening in InAs was for example measured in reference [VI.2], which reports a linewidth of 5 meV at zero bias, increasing to up to 25 meV under electrical injection.

As for sample P3a, Figure VI-6 represents the measured inversion factor spectra at 300 K for sample M3a. They also converge on the low energy end of the spectrum, which was used to determine the calibration constant *C*.

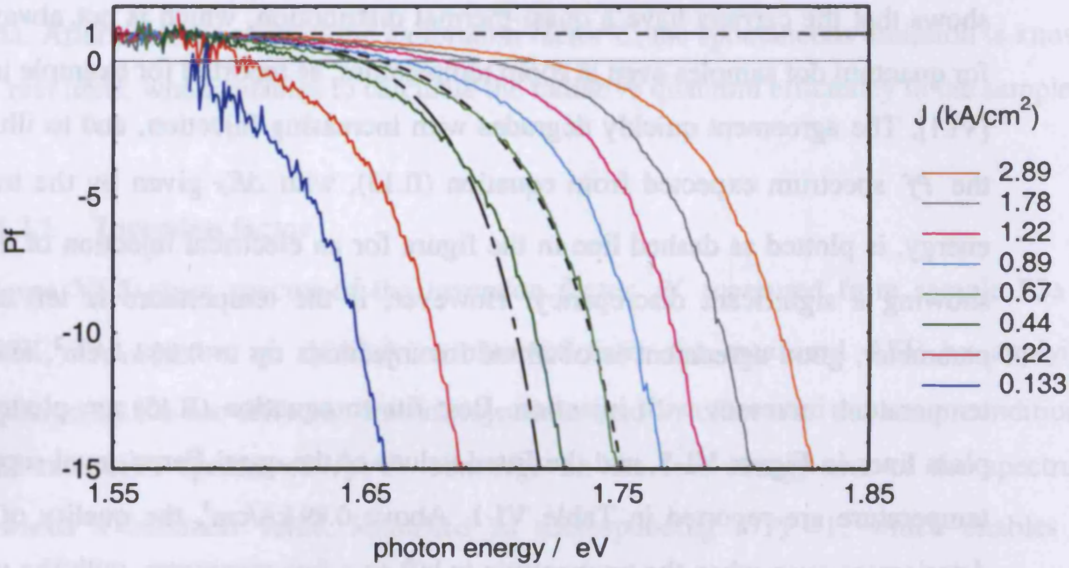

Figure VI-6 Inversion factor Pf for sample M3a, at 300K

The spectra fit poorly to (II.13). To illustrate this, the spectrum expected from equation (II.13) with T = 300 K and ΔE_F given by the transparency energy is plotted as a long-dashed line in Figure VI-6 for a current injection at 0.67 kA/cm^2. The best fit to equation (II.13) leaving both the temperature and Fermi-level separation as free parameters, which gives ΔE_F = 1.656 eV and T = 400 K, is plotted as a short-dashed line in the figure, showing poor agreement.

Within a quantum dot layer, non-thermal carrier distribution can arise from finite capture and escape time to and from the dots. The carriers can also be non-uniformly distributed amongst the dot layers, with each layer separately in thermal equilibrium and described by its own Fermi-level separation, as was for example reported for a multi-quantum well sample in reference [VI.4].

VI.2.2 Spontaneous emission and radiative efficiency

The calibration coefficient C being known from the measurement of the inversion factor, the spontaneous emission spectrum measured in arbitrary units, can be calibrated. Figure VI-7 and Figure VI-8 show the measured the spontaneous emission rate spectra in real units in samples P3a and M3a respectively, in the TE (TE_x+TE_y) polarisations.

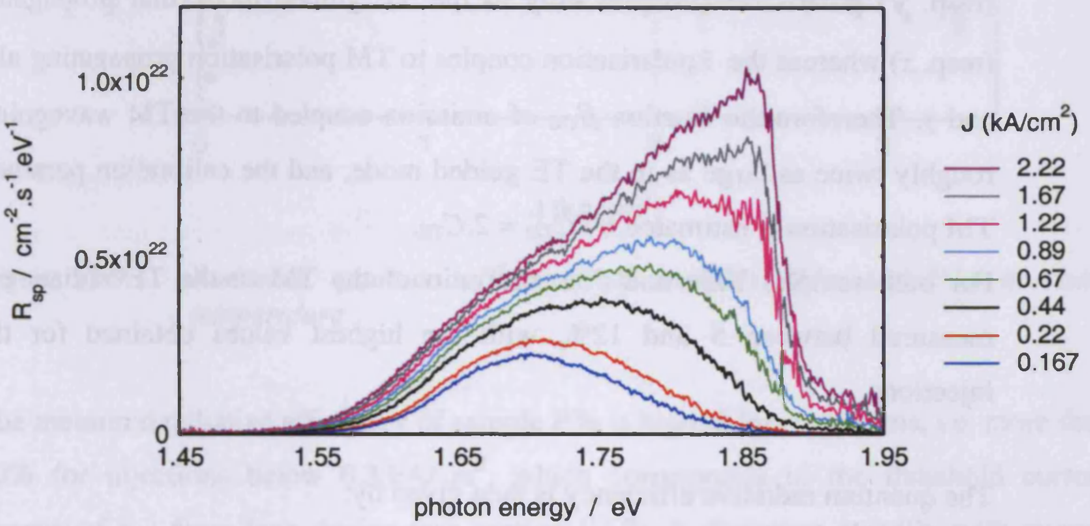

Figure VI-7 Spontaneous emission rate in the TE polarisation (TEx+TEy) from sample P3a at 302K

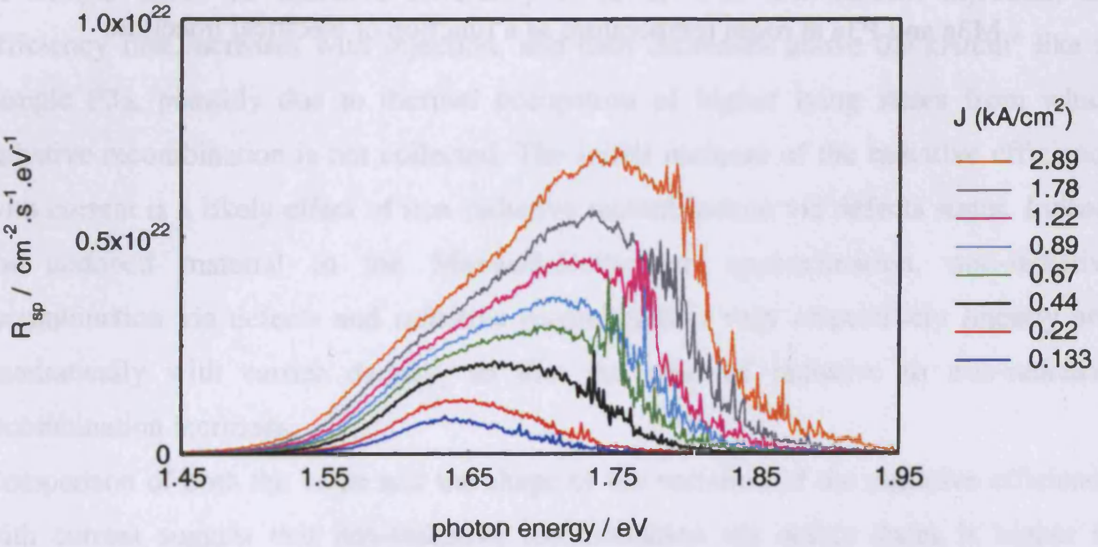

Figure VI-8 Spontaneous emission rate in the TE polarisation (TEx+TEy) from sample M3a at 300K

The radiative recombination current density is obtained by integrating the spontaneous emission spectra for all three polarisations, as described in section II.3.1.3). In the TM polarisation, the measurement error is too large to be able to determine the calibration factor C_{TM} from the measurement of the inversion factor, and C_{TM} is deduced from the value obtained for the TE polarisation C_{TE} for the same measurement conditions.

C is proportional to the fraction of spontaneous emission coupled to the waveguide, denoted by β_{TE} and β_{TM} for TE and TM modes. For small propagation angles, the $\hat{x}$ (resp. $\hat{y}$) polarisation couples only to the TE guided mode that propagates along y (resp. x) whereas the $\hat{z}$ polarisation couples to TM polarisation propagating along both x and y. Therefore the fraction β_{TM} of emission coupled to the TM waveguide mode is roughly twice as large as in the TE guided mode, and the calibration parameter for the TM polarisation is estimated by $C_{TM} = 2.C_{TE}$.

For both samples M3a and P3a, the ratio of the TM to the TE radiative current is measured between 5 and 12%, with the highest values obtained for the highest injections.

The quantum radiative efficiency is then given by:

$$\eta = \frac{\sum\limits_{p=TEx,TEy,TM} \int R_{sp}^{p}(\hbar\omega)d(\hbar\omega)}{J / e} \qquad \text{(VI.1)}$$

The measured radiative quantum efficiency is plotted in Figure VI-9 for both samples M3a and P3a at room temperature as a function of electrical injection.

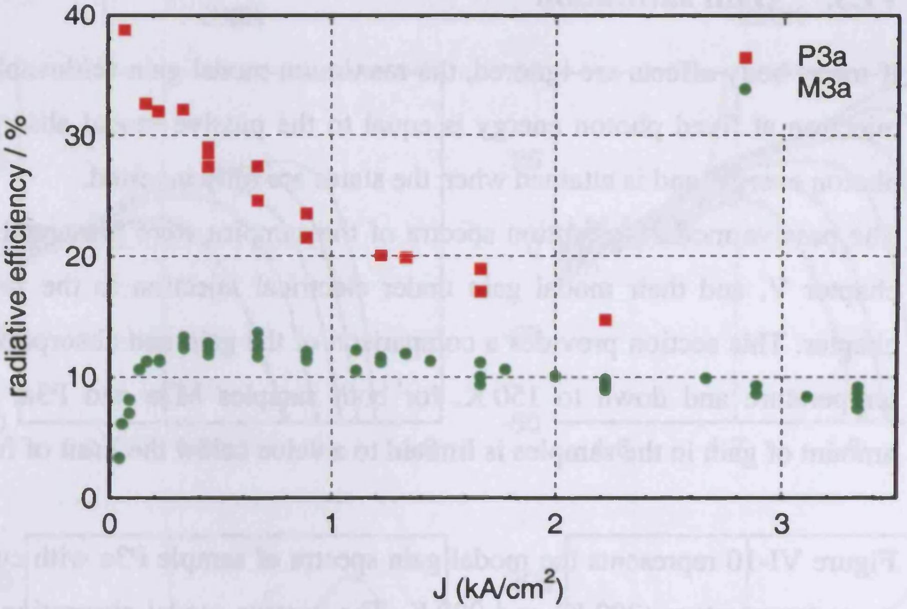

Figure VI-9 *Radiative quantum efficiency of samples M3a and P3a at room temperature*

The measured radiative efficiency of sample P3a is high at low injections, i.e. more than 30% for injections below 0.3 kA/cm^2, which corresponds to the threshold current density of a 1.6mm-long device (see section IV.2). It decreases steadily with current injection, which is consistent with a thermal population of higher lying states, which increases as the pumping level (Fermi-level separation) increases.

In sample M3a, the radiative efficiency is lower. For low current injection, the efficiency first increases with injection, and then decreases above 0.3 kA/cm^2 like in sample P3a, possibly due to thermal occupation of higher lying states from which radiative recombination is not collected. The initial increase of the radiative efficiency with current is a likely effect of non-radiative recombination via defects states. Indeed, for undoped material in the Maxwell-Boltzmann approximation, non-radiative recombination via defects and radiative recombination vary respectively linearly and quadratically with carrier density, so that the ratio of radiative to non-radiative recombination increases.

Comparison of both the value and the shape of the variation of the radiative efficiency with current suggest that non-radiative recombination via defect states is higher in sample M3a compared to P3a.

VI.3. Gain saturation

If many body effects are ignored, the maximum modal gain achievable under electrical injection at fixed photon energy is equal to the passive modal absorption at the same photon energy, and is attained when the states are fully inverted.

The passive modal absorption spectra of the samples were presented and compared in chapter V, and their modal gain under electrical injection in the first section of this chapter. This section provides a comparison of the gain and absorption spectra at room temperature and down to 150 K, for both samples M3a and P3a, showing that the amount of gain in the samples is limited to a value below the limit of full inversion.

Figure VI-10 represents the modal gain spectra of sample P3a with current injection, at room temperature (302 K) and 220 K. The passive modal absorption is represented in red colour.

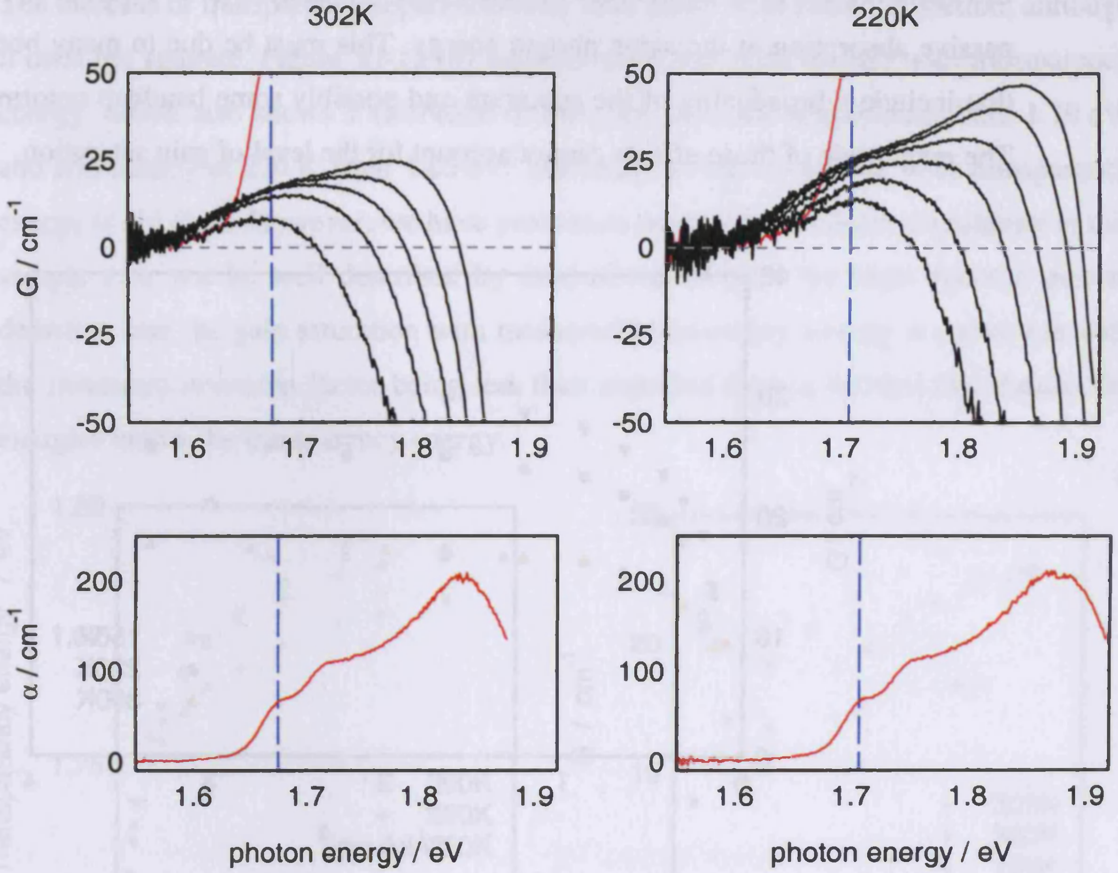

Figure VI-10 Modal gain spectra of sample P3a under electrical injection (upper) with current densities from 0.17 to 3.33kA/cm^2 and of the passive material (lower) at 302K (left) and 220K (right)
(The vertical blue line is at 1.675 eV at 300K, and 1.707 eV at 220K, indicating the same states at the two temperatures).

It was shown in chapter V.4 that the passive absorption spectrum of the sample shifts rigidly with temperature. The first peak of the spectrum, which is at a photon energies of 1.675 eV and 1.707 eV at 302 K and 220 K respectively, as indicated by vertical dashed lines in Figure VI-10, provides a modal absorption of 64 cm^{-1}. Hence if the states participating to transitions at that energy can be fully inverted, the maximum achievable modal gain from those states is also 64 cm^{-1}, (which is enough to achieve lasing of a device as short as 200 μm). However, the modal gain under electrical injection for both temperatures saturates much below this value. The modal gain versus current density at a photon energy corresponding to the first peak of the absorption is plotted on Figure VI-11 for temperatures of 302, 220 and 150 K, showing a saturation of the gain at a level that increases with temperature with respective values of 17, 24 and 30 cm^{-1}, but remains below the full inversion limit.

In Figure VI-10, it is visible that the gain near the band edge can exceed the value of passive absorption at the same photon energy. This must be due to many body effects that include a broadening of the spectrum and possibly some bandgap renormalisation. The magnitude of those effects cannot account for the level of gain saturation.

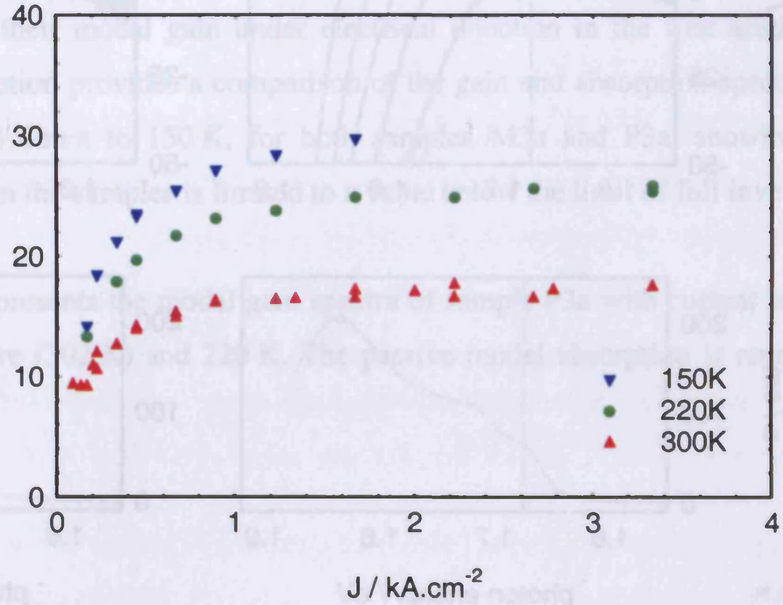

Figure VI-11 Modal gain versus electrical injection at a photon energy corresponding to the first peak of the absorption spectrum

Saturation of the gain with current at a level which is increasing with decreasing temperature was reported in [VI.4] for InAs dots, where it was shown that it could be accounted for by population of the wetting layer states. The large effect of the wetting layer on the dot occupation lies in the fact that it represents a large number of states compared to those of the dots, so that the movement of the Fermi-levels is significantly slowed down when getting nearer to the wetting layer states. Here it is visible from the gain spectra at high injection that higher states are significantly populated, especially at 220 K, and that they must play an important role in determining the occupancy of the dot ground states. Recombination of carriers in the excited dot states, the states in smaller dots and two-dimensional states, but also carrier leakage over the barriers, would all contribute to a saturation of the ground state gain with current. The measured transparency energy, which is a measure of the Fermi-level separation if the carriers are in thermal equilibrium, is plot as a function of injected current on Figure VI-12 *(a)*.

The increase of transparency separation does slow down with current injection, although it does not saturate. Figure VI-12 *(b)* represents the variation of gain with transparency energy, which also shows a saturation of the gain, at room temperature from 1.79 eV, and less clearly at 220 K from 1.85 eV. The cause of this saturation with transparency energy is not clear. However, we have previously seen that the carrier population in this sample may not be well described by thermal equilibrium for high injected current densities, and the gain saturation with measured transparency energy is consistent with the measured inversion factor being less than expected from a thermal distribution for energies below the transparency energy.

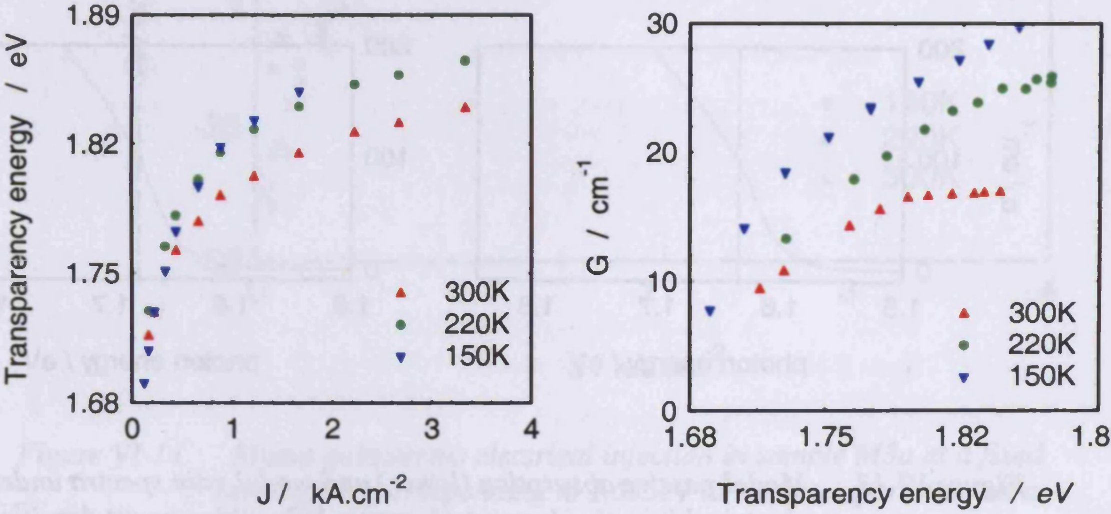

(a) *(b)*

Figure VI-12 Transparency energy versus current density and gain from the first peak of the absorption spectrum versus transparency energy in sample P3a. At temperatures of 220 and 150K, the transparency energy has been shifted to compensate for the shift of the absorption spectrum with temperature.

Figure VI-13 is the equivalent of Figure VI-10 for sample M3a. The modal gain spectra G of sample M3a is plotted at several current injections (not equally spaced in current) at room temperature and 175 K, and the passive modal absorption is represented in red colour.

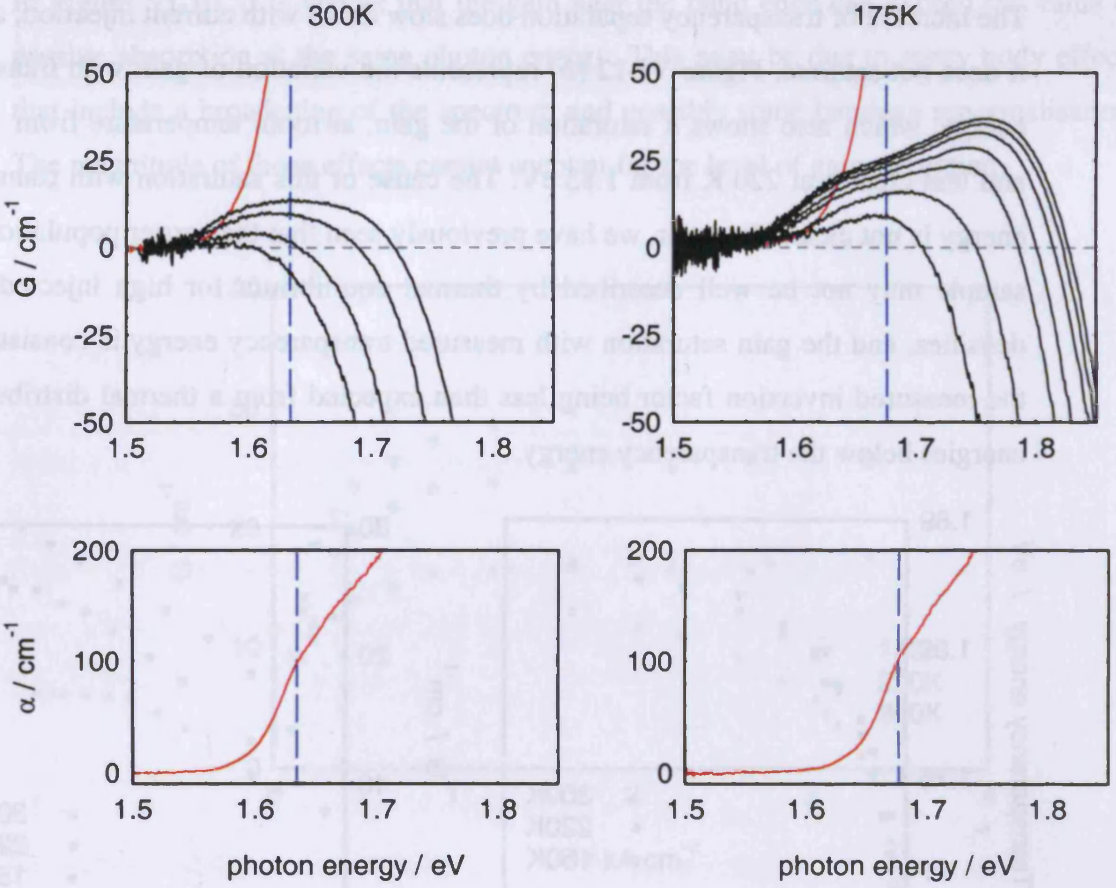

Figure VI-13 Modal passive absorption (lower) and modal gain spectra under electrical injection (upper) of sample M3a with current densities from 0.33 to 3.33kA/cm2 , at 298K (left) and 175K (right) (The vertical blue line is at 1.634 eV at 300K, and 1.6765 eV at 175K, indicating the same states at the two temperatures.)

On Figure VI-13, the vertical dashed line indicates the photon energy of the feature in the absorption spectrum, for which the modal passive absorption is 100 cm^{-1}. It is at 1.634 eV and 1.6165 eV respectively at T = 298 K and T = 175 K. The absorption shifts rigidly with temperature (section V.4) and these energies correspond to the same states at different temperatures.

At 175 K, a second peak appears on the high energy side of the spectrum, showing significant population of the higher lying states that may arise from transitions in small dots. Many body effects are also visible near the band edge, with the first peak of the gain at 175 K appearing to shift with injection, which is an indication of bandgap renormalisation.

Like in sample P3a, the gain under electrical injection at a photon energy corresponding to the feature in the absorption spectrum is far from reaching the limit of full inversion. The modal gain at this photon energy, which is adjusted with temperature to compensate for the shift of the passive modal absorption spectrum, is plotted in Figure VI-14 as a function of current density.

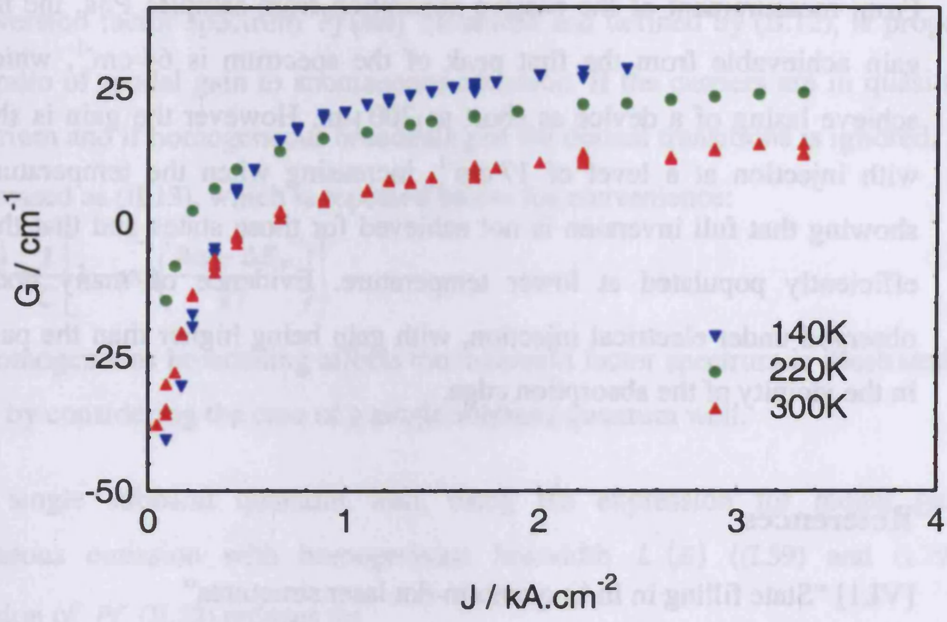

Figure VI-14 Modal gain versus electrical injection in sample M3a at a fixed transition corresponding to 1.635eV at room temperature, as a function of injected current density.

Sample M3a also exhibits a saturation of the gain with current injection below the level of full inversion of 100 cm^{-1}, with a saturation level that increases as the temperature decreases.

VI.4. Summary

Modal gain spectra of the samples under electrical injection were measured and compared. Little gain was obtained at room temperature from samples M1a, M2a and M3a, grown on 10º off substrates at a temperature of 650ºC, with the highest gain achieved from sample M3a grown at a high growth rate of 2.5 ML/s. A higher and narrower gain spectrum is obtained from samples M1b, grown on (211)B substrate. Gain spectra from sample P3a grown at a higher temperature of 690ºC is higher than in the other samples grown on 10º off substrates at a lower temperature, and confirms results of current threshold measurements presented in chapter IV.

Quantum radiative efficiency was measured for samples M3a and P3a at room temperature. The efficiency from samples P3a was measured at about 40% at low injection and decreases with increasing injection. The efficiency measured in sample M3a is less than 15% and first increases with injection, suggesting higher non-radiative recombination via defects.

From measurement of the passive absorption from samples P3a, the maximum modal gain achievable from the first peak of the spectrum is 64 cm^{-1}, which is enough to achieve lasing of a device as short as 200 μm. However the gain is shown to saturate with injection at a level of 17 cm^{-1}, increasing when the temperature is decreased, showing that full inversion is not achieved for those states and that the dots are more efficiently populated at lower temperature. Evidence of many body effects were observed under electrical injection, with gain being higher than the passive absorption in the vicinity of the absorption edge.

References

[VI.1] "State filling in InAs quantum-dot laser structures"
S Osborne, P Blood, PM Smowton, J Lutti, YC Xin, A Stintz, D Huffaker, LF Lester,
IEEE Journal of Quantum Electronics **40** (2004) pp. 1639 - 1645

[VI.2] "Time-resolved four-wave mixing in InAs/InGaAs quantum-dot amplifiers under electrical injection"
P Borri, W Langbein, JM Hvam, F. Heinrichsdorff, MH Mao and D Bimberg
Applied Physics Letters **76**, (2000) pp. 1380-1382

[VI.3] "Non-uniform carrier distribution in multi-quantum-well lasers"
PM Smowton, GM Lewis, A Sobiesierski, P Blood, J Lutti, and S Osbourne
Applied Physics Letters **83**, (2003) pp. 419-421

[VI.4] "Experimental investigation of the effect of wetting-layer states on the gain-current characteristic of quantum-dot lasers"
DR Matthews, HD Summers, PM Smowton, M Hopkinson
Applied Physics Letters **81** (2002) pp 4904-4906

Appendix VI.1

Inversion factor and inhomogeneous broadening

The inversion factor spectrum $Pf(\hbar\omega)$ measured and defined by (II.12), is proportional to the ratio of modal gain to spontaneous emission. If the carriers are in quasi-thermal equilibrium and if homogeneous broadening of the optical transitions is ignored, Pf can be expressed as (II.13), which is repeated below for convenience:

$$\frac{Pf(\hbar\omega)}{C}=\frac{1}{C}\left[1-\exp\left(\frac{\hbar\omega-\Delta E_F}{kT}\right)\right] \tag{VI.2}$$

How homogeneous broadening affects the inversion factor spectrum is illustrated in this section by considering the case of a single subband quantum well.

For a single subband quantum well, using the expression for modal gain and spontaneous emission with homogeneous linewidth $L\,(E)$ ((I.59) and (I.79)), the expression of Pf (II.12) reduces to:

$$Pf(\hbar\omega)=\frac{\int\limits_{E>E_0}\{f_c[E_c(E)]-f_v[E_v(E)]\}L\,(E-\hbar\omega)dE}{\int\limits_{E>E_0}f_c[E_c(E)]\{1-f_v[E_v(E)]\}L\,(E-\hbar\omega)dE} \tag{VI.3}$$

where E_0 is the energy separation between the conduction and the valence subbands. Figure VI-15 shows Pf spectra calculated from (VI.3) with a Gaussian homogeneous linewidth $L\,(E)$ of width (2σ) of 0, 20 and 40 meV. The carriers are assumed in quasi-thermal equilibrium at a temperature T of 300 K. To calculate the occupancy probabilities spectra f_c and f_v in the conduction and valence bands, the position of the conduction and valence band Fermi-levels are determined from the condition of charge neutrality. The quantum well is such that the energy separation between conduction and valence subbands E_0 is 1.5 eV, and the ratio of hole to electron effective masses is taken as 5; the quasi-Fermi level separation ΔE_F is 1.7 eV.

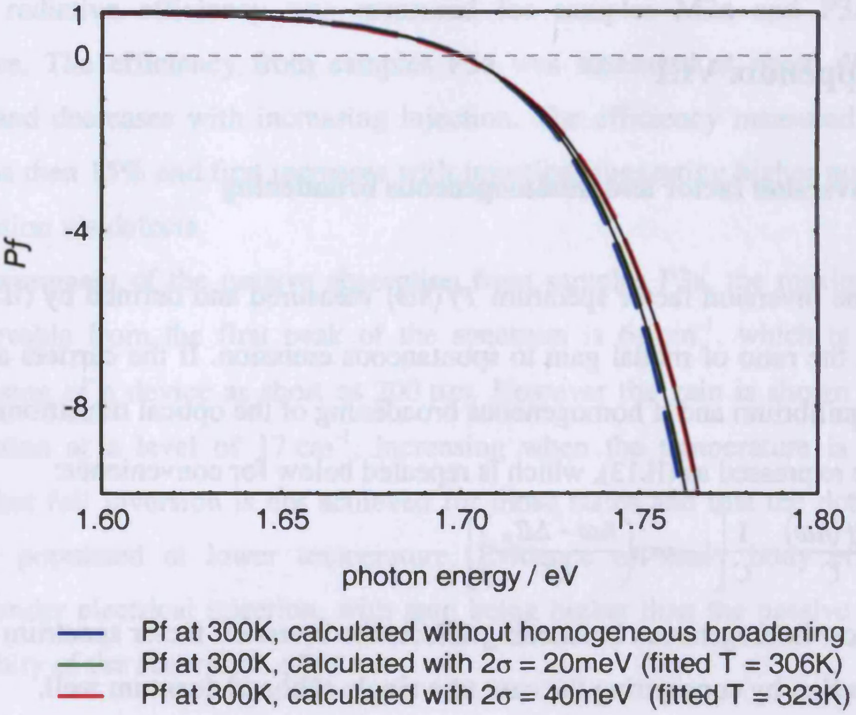

Figure VI-15 *Inversion factor for a single subband quantum well at 300K, with Gaussian homogeneous linewidth of width 2σ.*
It is assumed that the carriers are in quasi-thermal equilibrium with $\Delta E_F = 1.7$ eV. The subband edge of the quantum well is at 1.5 eV and the valence to conduction band mass ratio is 5.

In Figure VI-15, the black continuous lines represent the best fit of the calculated *Pf* spectra to expression (II.13). For homogeneous linewidths of 20 and 40 meV, the fitted temperatures are respectively 306 K and 323 K, while the fitted Fermi level separation is off its true value of 1.7 eV by less than 0.1 meV.

Hence it is shown by examining the simple case of a subband quantum well that homogeneous broadening can lead to an overestimation of the carriers' temperature if the *Pf* spectrum is fitted to equation (II.13). The calculation with homogeneous broadening of 20 meV, which is a realistic amount for a sample under electrical excitation, leads to an overestimation of the temperature by 6K at 300K.

VII. Summary, conclusions and further work

VII.1. Summary and conclusions

The work presented in this thesis focused on analysis of the effect of measurement collection geometry in the multisection technique (*i*), and optical characterisation of InP quantum dot laser samples (*ii*).

(*i*) Analysis of the effect of the measurement geometry in the multisection technique was carried out for broad area laser type of structures, where light is not guided in the plane of the layer. A differential expression for the Amplified Spontaneous Emission at the end of a pumped stripe was derived. Numerical integration was performed to simulate the measured ASE, taking into account the collection geometry, and the impact of the collection geometry on the result of gain measurement was calculated. The analysis was shown to agree quantitavely with experimental data and lead to the following conclusions:

- In order to ensure accurate measurement of the gain, the collection geometry should be limited so that rays that intercept the edges of the pumped stripe are not collected. In consequence the maximum collection angle that shall be used depends on the aspect ratio of the stripe. For an excitation stripe of 50 μm wide by 600 μm long, the maximum collection half-angle for a sample with a refractive index of 3.5, is 8.5° when the ASE is collected from the centre of the nearfield.

- When this condition is not met, the measurement underestimates the value of the gain. If the gain is extracted from the ASE measured from two pumped lengths L and $2L$, the error introduced by the collection geometry has mostly the effect of shifting the measured spectrum down, leading to an overestimation of the internal mode loss. If the ASE is measured from many stripe lengths, the dependence of the measured ASE over pumped length still fits well with an exponential function; hence using more than two pumped lengths does not help in finding out if the collection geometry, and hence the result of the measurement in that respect, is correct.

(ii) Optical characterisation was carried out on InP quantum dot laser heterostructure samples, consisting of five layers of self-assembled InP dots in GaInP quantum wells and separated by $Al_{0.3}Ga_{0.7}InP$ barriers. The samples were grown in Sheffield University by MOVPE on (100) 10°off and (211)B GaAs substrates, and the dots were formed by depositing two monolayers of InP on $Al_{0.3}Ga_{0.7}InP$ with growth rates from 0.8 to 2.5 monolayers per second and at growth temperature of 650 or 690°C. The measurements carried out on these samples included threshold current and lasing wavelength, absorption and gain spectra, and quantum radiative efficiency. The main outcomes are as follows:

- Room temperature threshold current density as low as 290 $A.cm^{-2}$ with a lasing wavelength of 740 nm for a 1.6 mm-long device with uncoated facets was obtained from the sample grown on (100) 10°off substrate at a growth rate of 2.5ML/sec and a temperature of 690°C. This is the lowest reported threshold current density for InP QD structures and demonstrates their potential for use in the 690-750 nm wavelength window. The sample also has the following measured properties:

➢ The passive absorption spectrum exhibits at least two resolved peaks from dot states at photon energies of 1.675 and 1.716 eV, with a full width at half maximum of 34 and 42 meV, that can be understood as ground and first excited states from the same ensemble of dots. Lasing is obtained from the first peak of the absorption spectrum for cavity lengths down to 1000 μm, and from higher energy transitions for 750 μm-long devices or shorter.

➢ The internal optical mode loss was measured at 4 ± 1 cm^{-1}.

➢ The radiative efficiency was measured to above 30 % for injection lower than 300 $A.cm^{-2}$, and decreases with increasing injection, with for example 20 % measured at 1.2 $kA.cm^{-2}$.

➢ The carrier distribution at room temperature was shown to be well described by quasi-thermal equilibrium for low excitation.

➢ Modal gain achieved from the first absorption peak saturates at a value of 17 cm^{-1} at room temperature, i.e. at about ¼ of the value for full population inversion given by the passive modal absorption. The level at which the gain saturates increases with decreasing temperature, showing that the population in the dots is limited by a thermally activated process. This behaviour was also observed on another sample grown at 650°C.

- The growth temperature was shown to have a large effect on the optical properties. Compared to the sample grown at 690°C which gives a low threshold current, a sample grown at 650°C, and otherwise same conditions, exhibits optical transitions at lower energies (by about 40 meV), does not have resolved absorption peaks, and fails to lase at room temperature. The sample grown at 690°C has a lower internal optical mode loss ($4 \pm 1\ \mathrm{cm}^{-1}$ against $7.5 \pm 1\ \mathrm{cm}^{-1}$) and a higher radiative efficiency (about 3 times higher for a low injection of $0.25\ \mathrm{kA/cm}^{-2}$, the difference decreasing with increasing injection), suggesting that the lower threshold current is due to a reduction of non-radiative recombination via defects that is likely to be linked to a better smoothness of the growth surface at a growth temperature of 690°C.

- Comparison of the passive absorption spectra from samples grown on (100) 10°off and (211)B substrates in the same conditions showed that the dot optical transitions in the (211)B sample are at higher photon energy, being consistent with smaller dot sizes observed in AFM measurements on uncapped samples.

- On all (100) 10°off samples, absorption in the TM polarisation was observed to occur at higher photon energies than in the TE polarisation by 30 to 40 meV.

- Evidence of many body effects were found, with positive gain achieved at photon energies below the passive absorption edge.

VII.2. Further work

One could gain more understanding of the samples properties from structural data. TEM plan-view and cross-section measurements could be made to determine the dot size, morphology and density. This would in particular shine more light on the nature of the peaks observed in the absorption spectrum in one of the samples, and validate or invalidate its description in terms of ground and excited states proposed in this thesis.

The optical properties of the samples were shown to be critically dependent upon growth temperature, with strong improvement obtained by increasing the growth temperature from 650 to 690°C. It may be worth carrying out a systematic investigation of the effect of growth temperature, and to try growth at even higher temperature.

A better growth surface smoothness was proposed as a possible explanation for the better quality of the sample grown at a temperature of 690°C compared to 650°C. Measurement of growth surface morphology after deposition of the first layer of dots could be performed in order to determine the validity of this hypothesis.